NTNU – Trondheim
Norwegian University of
Science and Technology

Mechanical and Acoustic Characterization of Perfluorocarbon Microbubbles Containing Nanoparticles

Gard Fostad Moe

Master of Science in Physics and Mathematics
Submission date: June 2015
Supervisor: Catharina de Lange Davies, IFY

Norwegian University of Science and Technology
Department of Physics

Abstract

In order to optimize the production and behaviour of ultrasound contrast agents it is necessary to map their characteristics. The aim of this master's thesis is to investigate different batches of perfluoropropane microbubbles stabilized by polymer nanoparticles and protein through the use of atomic force microscopy and acoustic measurements. This provides insight into how the microbubble responds to acoustic fields and may aid in predicting in-vivo behaviour. By using four different models: Reissner theory, Hertz theory, elastic membrane theory and the de Jong model the Young's Modulus of the nanoparticle microbubbles was investigated. A linear relationship was established between the Young's Modulus and the microbubble diameter for the Hertz theory and the de Jong model in three out of five measurement series. Across all the experiments the range of the Young's Modulus was: 0.82-8.31 MPa with the Reissner theory, 0.29-47.06 MPa with the Hertz theory, 2.9-2395.3 MPa using the elastic membrane theory and 6.43-137.16 kPa for the De Jong model. By comparing the nanoparticle microbubbles to bubbles with a shell of bovine serum albumin and SonoVue® it was determined that the addition of nanoparticles lowers the Young's Modulus of the shell accoring to the Reissner and de Jong theory. Modelling the microbubble as a homogeneous sphere as per the Hertz theory, however, predicts an increase in the Young's Modulus compared to albumin and phospholipid microbubbles. By measuring the attenuation of the microbubbles at evenly spaced intervals over 18 minutes it was found that the primary factor causing attenuation loss for the perfluropropane microbubbles is the gas exchange process where perfluoropropane seeks out of the bubble core and air diffuses in. The shell was also found to have a stabilizing effect in this process, slowing the dissolution by obstructing gas flow. By producing the microbubbles with microfluidic systems it is possible to attain narrower size distributions than with the ultraturrax setup and this causes a narrower attenuation band across the frequency axis. Backscatter experiments performed with three different transducer pairs showed that microbubbles combined with nanoparticles can produce subharmonics and a wide range of harmonics and ultraharmonics at low mechanical indeces.

Sammendrag

For å kunne optimalisere produksjonen av og egeneskapene til ultralydkontrastmiddel i form av mikrobobler er det viktig å kartlegge boblenes egenskaper. Målet med denne oppgaven er å undersøke ulike prøver av perfluoropropan mikrobobler som er stabilisert ved hjelp av polymernanopartikler og protein. Dette blir gjort ved atomkraftmikroskopi og akustiske forsøk. Disse målingene gir innsikt i hvordan mikroboblene vil oppføre seg når de blir utsatt for et akustisk felt og kan også være med og forutse hvordan boblene vil reagere in vivo. Ved å ta i bruk fire ulike modeller: Reissner teorien, Hertz teorien, elastisk membran teori samt de Jong modellen blir Young's modulusen til mikroboblene kartlagt. Et linært forhold mellom Young's modulus og boblediameteren ble avdekket for Hertz teori samt de Jong modellen i tre av fem måleserier. Over alle måleseriene var verdiene av Young's modulus: 0.82-8.31 MPa med Reissner teorien, 0.29-47.06 MPa med Hertz teorien, 2.9-2395.3 MPa ved bruk av elastisk membran teori og 6.43-137.16 kPa med De Jong modellen. Ved å sammenligne nanopartikkelboblene med bobler bestående kun av protein samt SonoVue® viste det seg at nanopartikler senker Young's modulus for mikroboblenes skall ifølge Reissner teori og De Jong modellen. Dersom man istedet valgte å modellere boblen som en homogen sfære ble resultatet at Young's modulus økte i forhold til protein- og lipidboblene. Ved å måle attenuasjonen forårsaket av mikroboblene gjennom faste intervaller i løpet av 18 minutter ble det bestemt at hovedårsaken til attenuasjonstapet er som følge av gassutvekslingen der perfluoropropan vil trenge ut av mikroboblene samtidig som luft vil diffundere inn. Det ble også vist at skallet har en stabiliserende virkning på oppløsningsprosessen ved å være et hinder for gassutvekslingen. Ved å produsere mikroboblene ved hjelp av mikrofluidikk kan man oppnå en smalere størrelsesfordeling og følgelig en smalere fordeling av attenuasjonen over frekvensene. Tilbakespredningen av ultralyd fra mikroboblene ble også undersøkt med tre forskjellige transducerpar og disse undersøkelsene viste at nanopartikkelboblene kan produsere undertoner, overtoner og ultraharmonier ved lav mekanisk indeks.

Preface

The work contained herein is the culmination of a master's degree in Applied Physics and Mathematics conducted at the Norwegian University of Science and Technology. It was produced at the Department of Physics as part of a specialization in Biophysics & Medical Technology. My sincere gratitude goes out to all the supportive people that have surrounded me during my time at NTNU. I would like to thank my main supervisor Catharina de Lange Davies (Professor, Dept. of Physics) for encouragement, setting up fruitful discussions and feedback. I would also like to thank Sigrid Berg (Post.doc/Scientist, SINTEF, Dept. of Medical Technology) for introducing me to the acoustic part of the work and diligently following me up. The same goes for Astrid Bjørkøy (Dept. of Physics) who provided invaluable assistance with the atomic force microscopy and microbubble imaging. Andreas Finnøy is also deserving of thanks for providing assistance with the data analysis. Lastly I would like to thank my family and Reidun Persdatter Ødegaard for all their support and proof reading.

Table of Contents

Chapter 1

Introduction

Following the separate development of ultrasound contrast agents (UCA) and nanoparticles (NP), researchers have explored the possibilities of combining the two, providing a simultaneous increase in ultrasound signal and drug delivery efficiency. The development of ultrasound contrast agents has seen the technology develop from pure gas bubbles to the incorporation of stabilizing shells and the loading of functional molecules [1]. The parameters of gas contents and shell structure have been constantly shifted, producing a wide array of different contrast agents, each with their particular set of traits. Examples of such variations are Albunex® (Molecular Biosystems, San Diego, CA, USA) with its albumin stabilizing shell and SonoVue® (Bracco, Milan, Italy), with a shell of phospholipids. Changing the production methods and bubble components does not only affect bubble stability and circulation time. These factors directly influence the key qualities of the microbubbles (MB) as contrast enhancers, changing the bubbles frequency response and ultrasound backscatter [2].

The typical contrast agent bubble is 1-7 microns, small enough that they can enter the microvasculature, but still not diffuse out of the blood stream [3]. This range in diameter also fits together with clinical ultrasound frequency, 2-10 MHz, in such a way that the resonance frequency of the UCA is located within it.

Parallel with the rapid development of new ultrasound contrast agents there has been an equal frontier in nanotechnology. The ability to accurately engineer structures on a nanometer scale has sparked widespread interest in many industries, medical technology being no exception. Their role as potential drug carriers is heavily focused. In the same manner in which the UCA shell protects its contrast enhancing core so does the nanoparticle shield its therapeutic content from degradation [4]. Nanoparticles are also small enough to pass through many of the barriers normally presented to larger drug molecules, which can see as much as 99% being blocked off as is the case with the blood-brain-barrier [5].

Splicing the progress made in these two fields opens the possibility of UCA's carrying nanoparticles. With the nanoparticles themselves being loaded with drugs this represents a new way of drug delivery, where its possible to use adverse effects of the UCA's in an ultrasound field to promote the passage of drugs into specific sites. These effects are related to the streams and heat generated by an oscillating or collapsing microbubble in an ultrasound field. The nanoparticles may in turn make the UCA's oscillate asymmetrically, giving enhanced contrast [6].

The microbubbles analysed in this thesis are the result of such a combination using protein shelled microbubbles with a core of perfluorocarbon gas. The nanoparticles in the shell are polymeric and stabilized by polyethylene glycol (PEG). Because of the difference these microbubbles represent compared to commercially available UCA's it is of interest to map their acoustic and mechanical properties. Their performance may then be analysed and compared. These in-vitro characteristics may give important clues to in-vivo behaviour and contribute to the optimization of the UCA's. The mechanical properties are mapped by the use of an atomic force microscopy, providing high-resolution force measurements, which in turn are used to give a respective Young's Modulus, describing the stiffness of the microbubble. The acoustic measurements, attenuation and backscatter properties, are done by exposing the microbubbles to acoustic fields at varying frequencies and pressure.

Chapter 2

Theory

2.1 Ultrasound and Contrast Agents

Ultrasound is the concept of using pressure waves, i.e. sound waves, with a frequency higher than the perceptive capabilities of humans. The established higher ranges of human hearing is perceived to be around 20 kHz for adults [7]. Ultrasound has found its applications in a wide variety of fields and industries, from sonar to material testing, and is also present in wildlife through the use of echo localization. This thesis' field of interest is the use of ultrasound in medical applications, treatment and diagnostics. The perhaps most well known example is the use of ultrasound during pregnancy, where it provides a hazard free way of imaging a foetus. When imaging the human body the frequency determines the spatial resolution of the rendered image as well as penetration depth [8]. Different applications therefore have unique set-ups to achieve the desired ultrasound effect. The nature of the human body, consisting largely of tissue containing water makes it an inherently difficult object to image with ultrasound. The concept of ultrasound agents (UCA) was therefore introduced to alleviate these hindrances. In its most basic form UCA's provide an acoustic impedance difference, providing increased amounts of backscatter from regions of interest. Pure gassbubbles quickly dissipate when injected in to the bloodstream where they diffuse. To prolong circulation times modern UCA's are fitted with a shell, partially to slow this process. Resistance to gas transport has been shown to be the most stabilizing effect of the shell [9]. These shells can consist of protein, lipids or combinations of different molecules. To further increase stability some UCA's are fitted with charged molecules to hinder any unwanted reactions, both between bubbles during storage and interactions when injected. Using heavier gases which are less prone to diffuse out of the shell, such as perfluorocarbon (PFC) or decafluorobutane, is also an important step towards increased stability.

2.2 Nanoparticles

Developments within the field of nanotechnology has allowed researchers to inquire into utilizing the new particles in biomedical applications. The particles represent an opportunity to design new treatment methods that exceed the capabilities of traditional drug treatments. Nanoparticles can be designed from a multitude of platforms, such as liposomes, polymers, albumin and in crystalized form [10]. Among these designs, liposomes and polymers are most frequently used. Polymers are favoured due to their ability to self-assemble as well as their hydrophobic core, which allows the transportation of poorly soluble drugs. Heath and Davis[4] single out four characteristics that separate nanoparticles from other therapeutics. These are:

1. Nanoparticles can carry large payloads that, due to their encapsulation, do not act as reactants when introduced into a biological environment. This is contrary to other targeting systems where the payload may alter the pharmacokinetics.

2. Nanoparticles can have multiple targeting modes because of the ability to carry more ligands than preceding options. This allows for either the increased affinity for a specific target or the construction of a multi-target system, comprised of several ligands.

3. Multiple drug types can be incorporated into the nanoparticles.

4. Finally, the nanoparticles enter cells through endocytose and therefore are able to bypass the immune system pumps that traditionally pose a significant barrier by actively excreting foreign substances.

To ensure drug availability, after the nanoparticle has reached the target, the capsules can be fitted with release mechanisms that respond to a variety of biological cues [11]. pH changes is one possible release mechanism, making use of the acidic nature of tumours in cancer therapy. Temperature changes is another viable option, as is ultrasound. For the nanoparticles to be able to reach their destination and improve circulation time, the capsules are often fitted with a PEG-coating, hindering premature degradation. As an added bonus, adding nanoparticles to the shell of a microbubble may promote non-linear oscillations, increasing backscatter when exposed to ultrasound [12]. A nanoparticle similar to those studied here is shown in Figure 2.1.

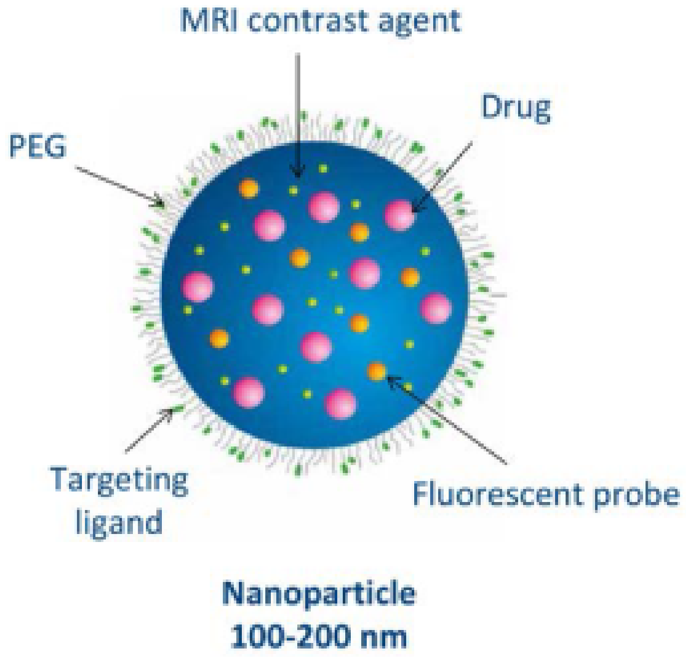

Figure 2.1: The composition of a nanoparticle variant, image taken from SINTEF.

2.2.1 EPR Effect

The enhanced permeability and retention retention effect (EPR) is a molecular weight dependant effect readily observed in tumour tissue. EPR affects nanoparticle drug delivery in two ways, through biodistribution and plasma half life [13]. The first part of the effect relates to the increased accumulation of nanoparticles in tumour tissue when compared to normal tissues. Secondly the nanoparticles are too large to be effectively cleared by the renal system. The EPR elicited a 13 fold increase in drug uptake in an in-vitro study done on human colon cancer, and so the effect has been shown to have a significant contribution [14].

2.3 Targeted Drug Delivery

In order to effectively image the area of interest and to limit the systemic distribution of any potential treatment drugs incorporated in the UCA's, targeting techniques are being developed. By attaching ligands to the microbubble shell it is possible to achieve greater accumulation of microbubbles in the desired area. This also provides prolonged circulation times due to the reduced strain on the microbubbles as they become stationary as opposed to moving in the bloodstream. Klibanov mentions two methods of attaching such ligands [8]. The methods differ in whether the ligand is attached to the shell material before or after bubble formation. Attaching the ligand prior to sonification will be most beneficial for small targeting molecules, as larger target molecules may be damaged during the bubble forming process. Using targeting molecules in combination with UCA's was successfully performed on mice, where the UCA's where set to target inflammatory tissue, targeting P-selectin [15].

2.4 Ultrasound Physics

The speed of sound is defined as

$$c = \nu\lambda = \frac{\omega}{k}, \tag{2.1}$$

where c is the phase speed of sound, ν the frequency and λ is the wavelength. This in turn equates to ω, the angular frequency divided by k, the wave number. The speed of sound in air is typically given as 344 m/s and in water 1480 m/s. In a gas, which is relevant in respect to ultrasound contrast agents, the pressure waves will cause the gas to heat and cool with compression and rarefaction as the wave propagates. The speed of sound can therefore be formulated as

$$c = \sqrt{\frac{\kappa p}{\rho}}, \tag{2.2}$$

where κ is a polytropic index varying whether the process is adiabatic, isothermal or a combination of the two. p denotes the pressure and ρ the density. The contrast generated during ultrasound imaging is provided by the impedance differences between two mediums, the specific acoustic impedance is given by

$$Z = \frac{p_{acoustic}}{v_{particle}}. \tag{2.3}$$

Assuming $p_{acoustic}$ is the change with respect to equilibrium pressure and that the oscillations are harmonical, the impedance can be further defined as

$$Z = \rho c, \tag{2.4}$$

namely the density times the speed of sound in the medium. The pressure variations in the medium can be expressed as

$$P = -i\omega\rho c\epsilon_0 e^{i(\omega t - kx)}. \tag{2.5}$$

The total energy density

$$E_{total} = \frac{1}{2}\rho \mid \dot{\epsilon} \mid_m ax^2, \tag{2.6}$$

can be used to express the intensity of the wave which is defined as

$$I = E_{total} c, \tag{2.7}$$

which in turn yields

$$I = \frac{P_A^2}{2Z}. \tag{2.8}$$

When the ultrasound wave traverses from one medium to another a part of the wave will be reflected while the other will be transmitted. By employing the fact that the pressure from the incident wave and reflected wave will equal the transmitted pressure, 2.3 and the boundary condition that the velocity of the two waves are equal in the interface the following coefficients can be established for the two waves:

$$T = \frac{2Z_2}{(Z_1 + Z_2)}, \tag{2.9}$$

and

$$R = \frac{Z_2 - Z_1}{Z_1 + Z_2}, \tag{2.10}$$

where the subscripts denote the medium. This highlights the importance of the impedance mismatch with regard to ultrasound contrast agents.

During the propagation the waves loses energy, which is transferred into the medium. This process is called attenuation and can be expressed as

$$P = P_0 e^{i(\omega t - qx)} e^{-bx}, \tag{2.11}$$

where b is a material property of the medium. This energy turns into a variety of effects such as heat, increased entropy, relaxation or hysteresis.

2.4.1 Non-Linear Effect

Although the signal generator in a given experiment may provide a stable symmetrical signal with a constant amplitude and frequency, the signal might yet deteriorate in the medium as it leaves the transducer. This is evident in non-linear effects affecting phase velocity. The two main contributions to this is the change in material stiffness, i.e. material non-linearity and convective non-linearity. The phase velocity can be adjusted to include a convective component which gives

$$v_{phase} = v + c, \tag{2.12}$$

where v is the convective term and c the local speed of sound. This local speed is in turn affected by the changes in stiffness and can be expressed as

$$c = c_0 + \frac{\gamma - 1}{2} v, \tag{2.13}$$

where c_0 is the speed of sound for waves with infinitesimal amplitude. γ can be fitted to accommodate for non-linearity in liquids by setting it to

$$\gamma = 1 + \frac{B}{A}, \tag{2.14}$$

$\frac{B}{A}$ being the non-linearity ratio.

2.4.2 Resonance Frequency and Harmonics

Taking the microbubble to be a simple harmonic oscillator on the form

$$\epsilon = e_0 e^{i\omega_0 t}, \tag{2.15}$$

and using Hook's law with Newton's second returns the resonance frequency as

$$\omega_0^2 = \frac{k}{m}. \tag{2.16}$$

Minnaert developed an expression for the resonance frequency of a single bubble in water, which after neglecting surface tension is on the form

$$f_0 = \frac{1}{2\pi} \sqrt{\frac{3\gamma P_0}{\rho R_0^2}}, \tag{2.17}$$

where γ is the polytropic constant,ρ is the water density and P_0 is the ambient pressure [16]. Depending on the characteristics of the microbubble, shell parameters such as the stiffness and uniformity as well as the size, the bubbles may oscillate in a non-linear fashion when subjected to an acoustic field. This causes the microbubbles to not only respond with the incoming transmitted frequency from the transducer, but also overtones, called harmonics, as well as subharmonics and ultraharmonics. The regular harmonics/overtones are recognized by being integer multiples of the transmitted wave frequency thus on the form $2f_0$,$3f_0$, $4f_0$ etc. This original frequency f_0 is called the fundamental. Subharmonics are defined as the fundamental divided by a integer on the form $\frac{f_0}{2}$, $\frac{f_0}{3}$. Lastly the response may be that of an ultraharmonic which takes the form $\frac{3f_0}{2}$, $\frac{5f_0}{2}$, $\frac{7f_0}{2}$ and so on.

2.5 Microbubble Models

As the microbubbles are subjected to ultrasound the changes in pressure will induce oscillations, causing the microbubbles to contract and expand in cycles. These motions can be described by mathematical approximations.

2.5.1 The Rayleigh-Plesset Equation

The Rayleigh Plesset equation maps the response of the microbubble under the assumption that it is situated in an incompressible fluid. Other assumptions are that there is only a single bubble, it's constantly spherical and uniform, no other forces act upon the bubble, vapour pressure is constant and that the radius is small. The first step is to assume that the pressure at a point distant to the bubble can be expressed as a constant pressure superimposed with a time varying pressure. Using these assumptions gives

$$p_\infty = p_0 + P(t), \tag{2.18}$$

which can be used to attribute a kinetic energy to the surrounding fluid

$$E_K = \frac{1}{2}\rho \int_R^\infty r^2 4\pi r^2 dr. \tag{2.19}$$

This gives a radius varying with time, and stating that this is equal to the difference in work by the fluid at a distance and at the bubble wall yields

$$\int R_0 R(p_L - p_\infty) 4\pi R^2 dR = 2\pi R^3 \dot{R}^2 \rho. \tag{2.20}$$

Differentiation then gives

$$\frac{p_L - p_\infty}{\rho} = \frac{3\dot{R}^2}{2} + R\dot{R}. \tag{2.21}$$

Inserting the expression for p_L and expanding the pressure returns the Rayleigh-Plesset equation

$$R\dot{R} + \frac{3\dot{R}^2}{2} = \frac{1}{\rho}\{(p_0 + \frac{2\sigma}{R_0} - p_v)(\frac{R_0}{R})^{3\kappa} + p_v - \frac{2\sigma}{R} - p_0 - P(t)\}, \tag{2.22}$$

where p_v is the vapour pressure and σ the surface tension.

2.5.2 The Church Model

The Church model is an attempt to describe the surface motion of microbubbles under the assumptions that the microbubbles are surrounded by a shell as seenin Figure 2.2 [17]. This shell is solid and visco-elastic. In addition the fluid surrounding the bubble is incompressible and Newtonian. The last assumption is that the surface tension is reduced by the shell in such a way that this effect can be neglected. Church proposed that these assumptions give rise to the follow equation

$$\begin{aligned} &\rho_L[\ddot{a}_2 a_2 + \frac{3}{2}\dot{a}_2^2] + \rho_S[\ddot{a}_2 a_2(\frac{a_2}{a_1} - 1) + \dot{a}_2^2(2\frac{a_2}{a_1} - \frac{1}{2}(\frac{a_2}{a_1}^4 - \frac{3}{2}] \\ &= p_{ge}(\frac{a_{1e}}{a_1})^{3\kappa} - p_\infty(t) - 4\eta_L\frac{\dot{a}_2}{a_2} - 4\eta_S\frac{V_S}{a_2^3}\frac{\dot{a}_1}{a_1} - 4G_S\frac{V_S}{a_2^3}(1 - \frac{a_{1e}}{a_1}), \end{aligned} \tag{2.23}$$

where a_1 and a_2 denotes the inner and outer shell radii, ρ_L is the density of the liquid, ρ_S the density of the solid, $p_g e$ the gas equilibrium pressure, $a_1 e$ and $a_2 e$ the equilibrium radii, κ is the polytropic exponent and $V_S = a_2^3 - a_1^3$.

Assuming that the shell is thin compared to the bubble radius allows for further simplification of the equation. This allows the neglect of the shells contribution to inertia. Further setting the equilibrium pressure of the bubble gas to be equal to the surrounding hydrostatic pressure and the pressure far away to be a superposition of the atmospheric pressure and the varying acoustic field yields

$$\rho_L(\ddot{a}a + \frac{3}{2}\dot{a}^2) = p_0((\frac{a_e}{a})^{3\kappa} - 1)) - p_i(t) - 4\eta_L\frac{\dot{a}}{a} - 12\eta_S\frac{d_S e a_e^2}{a^3}\frac{\dot{a}}{a} - 12G_S\frac{d_S a_e^2}{a^3}(1 - \frac{a_e}{a}). \tag{2.24}$$

where the radii a_1 and a_2 have been related through

$$\frac{a_{1e}}{a_1} \approx \frac{a_{2e}}{a_2}(1 + (\frac{d_{Se}}{a_{2e}} - \frac{d_S}{a_2})) \approx \frac{a_{2e}}{a_2} = \frac{a_e}{a}. \tag{2.25}$$

By performing a linearisation it is possible to solve 2.25 analytically as described by Hoff [17]. This is done by setting $a(t) = a_e(1 + x(t)), \mid x(t) \mid \ll 1$ and only keeping terms of x in the first order. This produces the following force equation

$$ma_e\ddot{x} + ra_e\dot{x} = -4\pi a_e^2 p_i(t). \tag{2.26}$$

Performing a Fourier transform of this equation gives the frequency based equation

$$(\omega_0^2 - \omega^2 + i\omega\omega_0\delta)\hat{x}(\omega) = -\frac{1}{\rho_L a_e^2}\hat{p_i}(\omega), \tag{2.27}$$

where the coefficients are given by

$$\omega_0^2 = \frac{s}{m} = \frac{1}{\rho_L a_e^2}(3\kappa p_0 + 12G_S)\frac{d_{Se}}{a_e} \tag{2.28}$$

$$\delta = \frac{R}{\omega_0 m} = \delta_L + \delta_S \tag{2.29}$$

$$\delta_L = \frac{4\eta_L}{\omega_0\rho_L a_e^2} \tag{2.30}$$

$$\delta_S = \frac{12\eta_S\frac{d_{Se}}{a_e}}{\omega_0\rho_L a_e^2} \tag{2.31}$$

This leads to an expression for the radial oscillation

$$\hat{x}(\omega) = \frac{1}{\Omega^2 - 1 - i\Omega\delta}\frac{\hat{p_i}(\omega)}{\rho_L\omega_0^2 a_e^2}, \Omega = \frac{\omega}{\omega_0}. \tag{2.32}$$

2.5.3 Scattering and Attenuation

The added attenuation of the solution after the addition of microbubbles can be computed by treating the solution as a sum of individual bubbles as described by Hoff [17]. This is defined through the extinction cross section σ_e, given by

$$\sigma_e = 4\pi a_e^2\frac{\Omega^4}{(1-\Omega^2)^2 + (\Omega\delta)^2}\frac{\delta}{\delta_c}, \tag{2.33}$$

where δ is the sum of all dampening constants and δ_c is the radiation dampening constant. Combining this result with 2.32 gives

$$\sigma_e(a,\omega) = 4\pi a_e^2\frac{c\delta}{a_e\omega_0}\frac{\Omega^2}{(1-\Omega^2)^2 + \Omega^2\delta^2}. \tag{2.34}$$

Assuming the suspension is of low enough for the bubbles not to interact one can express the attenuation in decibels as

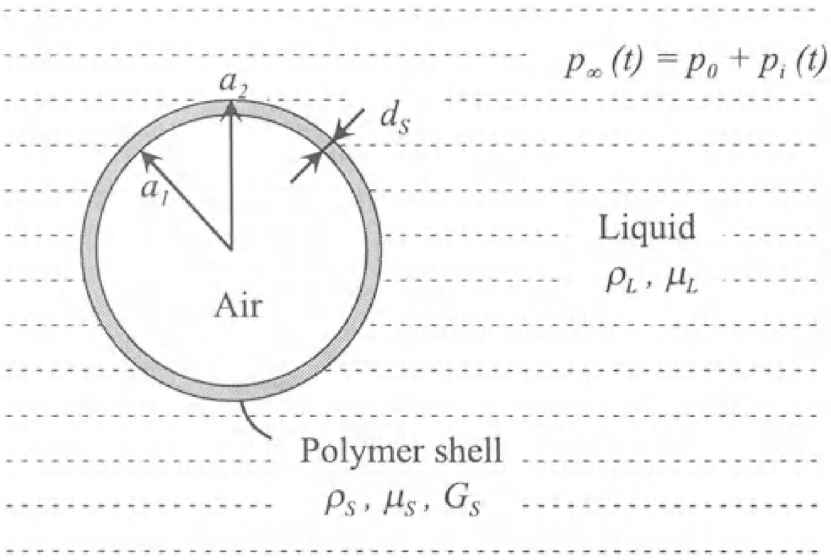

Figure 2.2: The theoretical concept forming the basis of the Church equation, adapted from Hoff [17].

$$\alpha(\omega) = 10(\log e)\int_0^\infty \sigma_e(a,\omega)n(a)da[dB], \tag{2.35}$$

with $n(a)$ being the number of bubbles.

The scattering cross section is given by

$$\sigma_S(a_e,\omega) = 4\pi a_e^2 \cdot \frac{\Omega^4}{(\Omega^2-1)^2+\Omega^2\delta^2}. \tag{2.36}$$

2.6 Effects on Microbubbles in Acoustic Fields

2.6.1 Coalescence

When many microbubbles are present in a solution they may start to merge. When coalescence occurs the film between two colliding bubbles drain before the bubbles rupture, producing an enlarged version. Whether two colliding microbubbles undergo coalescence depends upon the surface tension and radius of the microbubbles. Small bubbles are more prone to coalescing. To counteract this effect UCA's may be fitted with charged particles in order to repulse each other. The process is illustrated in Figure 2.3.

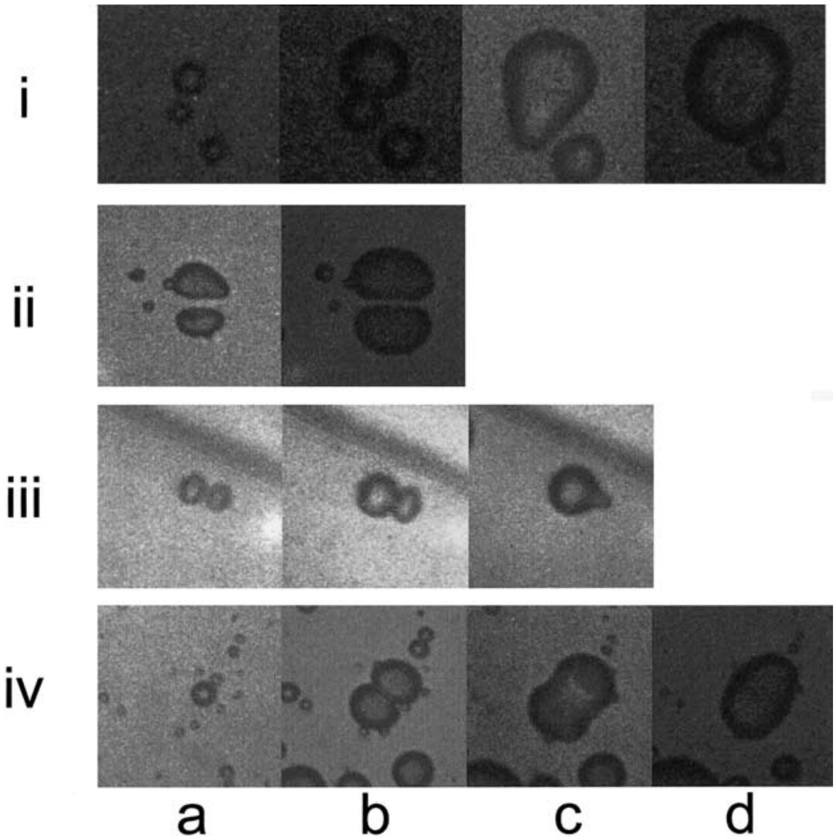

Figure 2.3: Coalescence of microbubbles in time frames as captured by Postema [18]

2.6.2 Non-Inertial Cavitation

When the microbubble is affected by the incoming ultrasound the microbubble may start to oscillate around its resonance frequency. In non-inertial cavitation these oscillations persist, contrary to inertial cavitation where the microbubble is rapidly destroyed. Non-inertial can, however, also have cause effects relevant to drug delivery. By applying an ultrasound field lower than the threshold for inertial cavitation and thus avoiding destruction, the stable oscillations of the microbubbles can cause ”micro-streaming” that occurs around the bubble surface. The streams, though less violent than the implosions in inertial cavitation can induce shear stresses in the tissue around the bubble [19] [20].

2.6.3 Inertial Cavitation

If a microbubble is subjected to a high intensity acoustic field it may undergo the process of inertial cavitation. This refers to the rapid increase in bubble diameter due to increasing pressure, followed by a rapid implosion releasing energy. This has great implications for drug delivery as the energy released can be used to increase the permeability of therapeutic barriers. Shohet et. al successfully employed this strategy to introduce a transgene expression into rat hearts [21]. If the microbubble undergoes inertial cavitation next to a solid surface, the uneven distribution of pressure in the microbubble may lead to the generation of a jet. The jet strikes out from an involution at the microbubble surface, passes through the bubble and hits the wall that is in the bubble proximity [22]. If the constraining wall next to the bubble consists of live cells this may cause damage. Another potential consequence of inertial cavitation and the heat generation is the forming of free radicals, an undesirable side effect [19].

2.6.4 Nucleation

Nucleation is a process in which the acoustic field generates new macrobubbles from weaknesses in the medium [23]. This can occur either homogeneously or heterogeneously, the first being the generation of micro nuclei due to thermal variations. If the nucleation occurs heterogeneously it is dependant on either impurities or interfaces. The impurities can consist of gas or other particles, promoting the formation of nuclei. This has consequences when investigating UCA's as the nucleation produces added signals as showed by Chen et al. [24]. When using ultrasound therapeutically these impurities will be constantly present in the form of particles in the bloodstream, and so this effect has to be accounted for. Homogeneous nucleation is governed by three equations. First the pressure difference is defined as

$$p_B - p = \frac{2S}{R}, \tag{2.37}$$

where p_B is the internal pressure, p the external, S the surface tension of the liquid and R the radius which leads to the first governing equation relating the maximal radius of the vacancy to the tensile strength of the liquid in the form of,

$$\Delta p_C = \frac{2S}{R_C}. \tag{2.38}$$

The second equation gives the energy required to form a new microbubble,

$$W_C R = \frac{4}{3}\pi R_C^2 S. \tag{2.39}$$

The final equation gives the nucleation rate

$$J = J_0 e^{-G_b}, \tag{2.40}$$

where $G_B = \frac{W_{CR}}{kT}$.

2.7 Microbubbles in Fluids

As microbubbles are introduced into a fluid the gas will start to diffuse out through the shell. In addition the microbubble will start to rise to the surface. Both of these effects will lead to temporal changes in the measurements.

2.7.1 The La Place Pressure

To better understand the driving mechanisms behind microbubble dissolution it is necessary to present the La Place pressure, the difference between the pressure inside and outside of the bubble. A stable microbubble is balanced through its surface tension, which is related to the excess pressure through

$$p_\sigma = \frac{2\sigma}{R}, \tag{2.41}$$

where σ is the surface tension and R is the radius.

2.7.2 Buoyancy

The buoyancy of an air bubble is given by

$$F = \frac{4\pi}{3} g(\rho' - \rho) R^3, \tag{2.42}$$

where ρ' is the water density and ρ is the bubble density, g is gravity and R the bubble radius. The buoyancy is not only relevant due to the microbubbles drifting out of the acoustic field, but also because of it's tendency to increase the gas diffusion through the shell [25].

2.7.3 The Epstein-Plesset Equation

The Epstein-Plesset equation forms the basis of gas diffusion related to a microbubble suspended in a liquid-gas solution [25]. The equation gives the change in radius with respect to time as

$$\frac{dR}{dt} = -\kappa d \frac{1 - f + \frac{\tau}{(R\rho(\infty))}}{1 + \frac{2\tau}{(3R\rho(\infty))}} \left\{ \frac{1}{R} + \frac{1}{(\pi\kappa t)^{\frac{1}{2}}} \right\}, \tag{2.43}$$

where κ is the coefficient of diffusivity of the gas in the liquid, $d = \frac{c_s}{\rho}$ is the saturated dissolved gas concentration divided by the gas density and $f = \frac{c_i}{\rho}$ is the initial dissolved gas concentration over the concentration at saturation. τ is defined as

$$\frac{2M\sigma}{BT}, \tag{2.44}$$

where M is the molecular weight of the gas, T is temperature, B is the universal gas constant and σ is the surface tension between the gas and liquid. Finally $\rho(\infty)$ is the density of the gas when there is no curvature present in the gas-liquid boundary.

Borden and Longo went further with the model, including a a term for the mass transfer resistance of the shell present in modern UCA's [9]. Expressed by the use of the Ostwald coefficient H this equated to

$$-\frac{dR}{dt} = \frac{H}{R_{water} + R_{shell}} \frac{(1 + \frac{2\sigma}{P_a R} - f)}{1 + \frac{4\sigma}{3P_a R}}, \tag{2.45}$$

where R_{water} and R_{shell} is the mass transfer resistance of the water and shell respectively. R_{water} is further defined through the diffusivity of water D_w as

$$R_{water} = \frac{1}{(\frac{D_w}{R} + \sqrt{\frac{D_w}{\pi t}})}. \tag{2.46}$$

2.8 Atomic Force Microscopy

One of the main focuses of the thesis is to make use of atomic force microscopy (AFM) to investigate the mechanical properties of the microbubbles. The results from these investigations are given in the form of the Young's Modulus, which gives a number to describe the rigidity of the microbubbles. The AFM utilizes piezo-electronics to position a cantilever with high precision. A voltage difference applied over the scanners, that move in the x-,y- and z-directions, expands or contracts the material. This movement is transferred into the sample stage, which in turn moves the cantilever with a tip attached to it, relative to the sample. This tip interacts with the sample. The tips and cantilevers are supplied in many shapes and forms specified by the requirement of the sample in question. Examples are flat cantilevers, coated tips and carbon nano-tips. The choice of set-up depends on the requirements of resolution, noise and the properties of the sample. As the tip is engaged with the sample any interactions are detected by a laser, positioned so that it is deflected off the back of the cantilever and into a photo-detector. This produces a voltage measurement. The detector then translates the voltage, i.e. the movements of the laser, into x-,y- and z-coordinates. A typical set-up is illustrtated in figure 2.4.

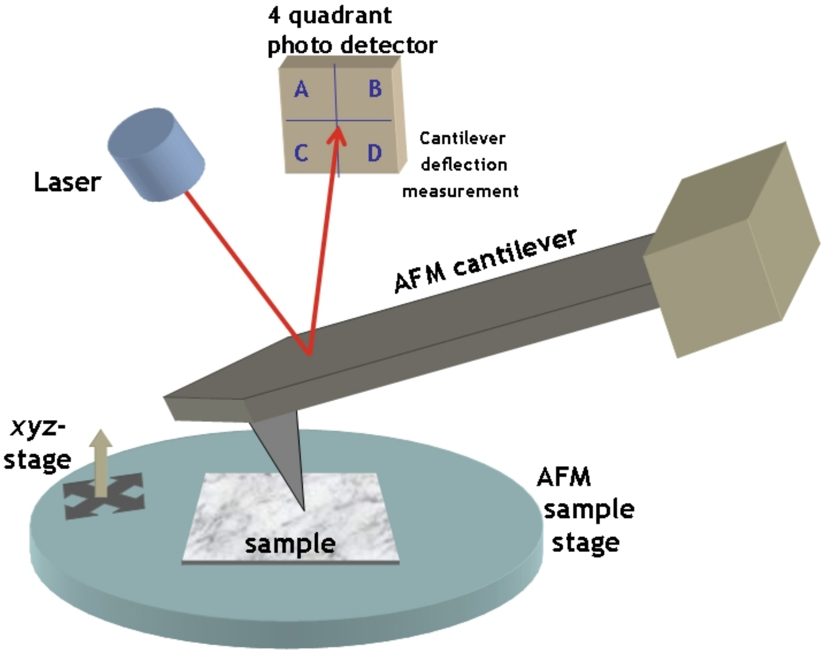

Figure 2.4: The AFM set-up showing the cantilever, laser and photo-detector interactions, adpated from the Opensource Handbook of Nanoscience and Nanotechnology.

The deflection following the tip-sample interaction can further be exploited into giving a force measurement through Hook's Law given by:

$$F = kd \tag{2.47}$$

where F is the force, d is the deflection and k is the spring constant, a material property of the cantilever-tip system.

The AFM has three main modes of operation, which, in line with the cantilever-tip system can be deployed in accordance with the sample at hand.

2.8.1 Contact Mode

In this mode the sample is in a continuous interaction with the tip. A consequence of this being that the forces acting on the cantilever-tip system are largely repulsive. This measurement method necessitates a sample that is robust enough to handle the constant interactions.

2.8.2 Tapping Mode

In response to the aforementioned requirement set by contact mode regarding sample toughness, tapping-mode was developed. Using the piezoelectric elements the tip is set to resonate, causing it to only directly contact the sample in intervals. This lessens the strain on the sample.

2.8.3 Non-Contact Mode

In particularly fragile samples where neither contact mode or tapping mode is a valid option, non-contact mode may be considered. Here the tip resonates above the sample, allowing the interaction of forces such as van der Waals while at the same time limiting strain and contamination.

2.9 Calculating the Young's Modulus

The Young's modulus provides a tangible numerical value for material stiffness that can easily be compared. Several theories have been developed in an attempt to accurately describe this characteristic.

2.9.1 de Jong Model

Under the assumption that the shell of the microbubble was homogeneous as well as of constant thickness and perfectly elastic, Reismann developed the following equation for the relationship between the internal and external pressure of the bubble with respect to radius displacement as presented by de Jong et al. [26]

$$u = (p_a - p_b)r^2\frac{1-\nu}{2Et}, \tag{2.48}$$

where u is the displacement of the radius, p_a the internal pressure, p_b the external pressure, ν the Poisson Ratio, E the Young's Modulus and t the thickness of the shell.

This equation is then used to calculate the contribution of the shell which is given as

$$S_{shell} = \frac{8\pi Et}{1-\nu}, \tag{2.49}$$

where S_{shell} is the shell stiffness. This equation uses a serial expansion on thickness, an assumption thus being made that the shell thickness is significantly smaller than the bubble radius.

2.9.2 The Reissner Theory

Glynos et al. used the Reissner theory to predict the stiffness of thin-shelled microbbubles, the shell consisting of the polymer polyactide with an extra layer of albumin [27]. The motivation was based on work done by Elsner et al. who determined the Reissner theory to be a good approximation by use of the finite element method [28]. By using Hook's law the force applied can be described as

$$F = k_s d, \tag{2.50}$$

where k_s is the shell spring constant and d is the deformation.

Reissner stated the following equation

$$d = \frac{\sqrt{3(1-\nu^2)}}{4}\frac{R}{h^2}\frac{F}{E}, \tag{2.51}$$

with h being the shell thickness and R the shell radius.

Inserting Hook's law gives

$$k = \frac{4}{\sqrt{3(1-\nu^2)}}\frac{h^2}{R}E, \tag{2.52}$$

where ν is the Poission ratio, R the shell radius, h shell thickness and E the Young's Modulus.

The Reissner theory is, however, not an adequate model when $h/r > 1/10$. Additional assumptions for the model is that the shell is homogeneous and spherical.

2.9.3 Hertz Theory

The Hertz theory was utilized by Santos et al. in an article comparing different models for the AFM measurements [29]. The theory provides a model for the contact of two spheres, but has been adapted for sphere-plate interactions, by assuming one sphere with infinite radius [30] [31]. In addition the model assumes two homogeneous spheres, meaning that it is not the shell itself being evaluated, but rather the sphere as a whole. The equation is stated as

$$E = \frac{3(1-\nu^2}{\sqrt{2}R_0^2}\frac{F}{\epsilon^{(}3/2)}, \tag{2.53}$$

where ϵ is the relative deformation.

2.9.4 Elastic Membrane Theory

This model was presented by Lulevich et al. and describes the forces acting upon spherical membranes, under the assumption that these are impermeable and that the pressure acts evenly on the shell [32]. Two equations are presented to represent all the forces on the sphere in the form of bending and stretching. Another assumption being that the deformation is restricted to the contact area. The stretching force is given as

$$F_s = 2\pi\frac{E}{1-\nu}hR_o\frac{[1+R_0/2R_s]^2}{(1+R_0/R_s)^4}\epsilon^3, \tag{2.54}$$

with the typical criteria of the shell being much thinner than the radius this simplifies to being dependant on R_0. The bending force is in turn given by

$$F_b = -\frac{\pi}{2\sqrt{2}}Eh^2\epsilon^{(}1/2). \tag{2.55}$$

The conclusion being that for relative deformations $\epsilon \gg 0.15$ the bending force is negligible.

Chapter 3

Materials and Methods

The following chapter contains the materials and methods used in the thesis with respect to the atomic force microscopy experiments as well as the acoustic measurements.

3.1 Microbubbles

The microbubbles that were of prime interest in this work were those with a mixed shell consisting of nanoparticles and casein. The gas core of these MB's is made up of perfluoropropane. These microbubbles, recognized by their GB-prefix, were produced by SINTEF. A notable exception is the GB-168 batch, which was made with air, in order to compare two different production methods, namely an ultraturrax method and that tested using the Tide® microfluidic system. The method used by SINTEF is comprised of a solution of casein, nanoparticles and gas which, as stated, is then stirred with an ultraturrax. Different turrax speeds produces microbubbles with different size distributions with higher speeds meaning a smaller radius. The concentrations of the reagents used to produce the microbubbles tested here was 1% casein and 1% nanoparticles, the latter being the Targ 121 particle. The nanoparticles self assemble on the microbubble surface and contain Nile Red® to make them fluorescent. Because of an unfortunate leak in the perfluoropropane tank the Tide® microbubbles had to be synthesized using air and 5% CO_2. This is also the case for the GB-168 batch, which was made using the GB procedure in all aspects except the gas core, which was switched to air. In the AFM part a commercially available microbubble was analysed for comparison in the form of SonoVue® (Bracco, Milan, Italy). This MB is clinically approved and consists of a phospholipid shell and a sulphur hexafluoride gas core. The last unique bubble design to be analysed is the J6 batch, a SINTEF produced microbubble with a pure BSA shell.

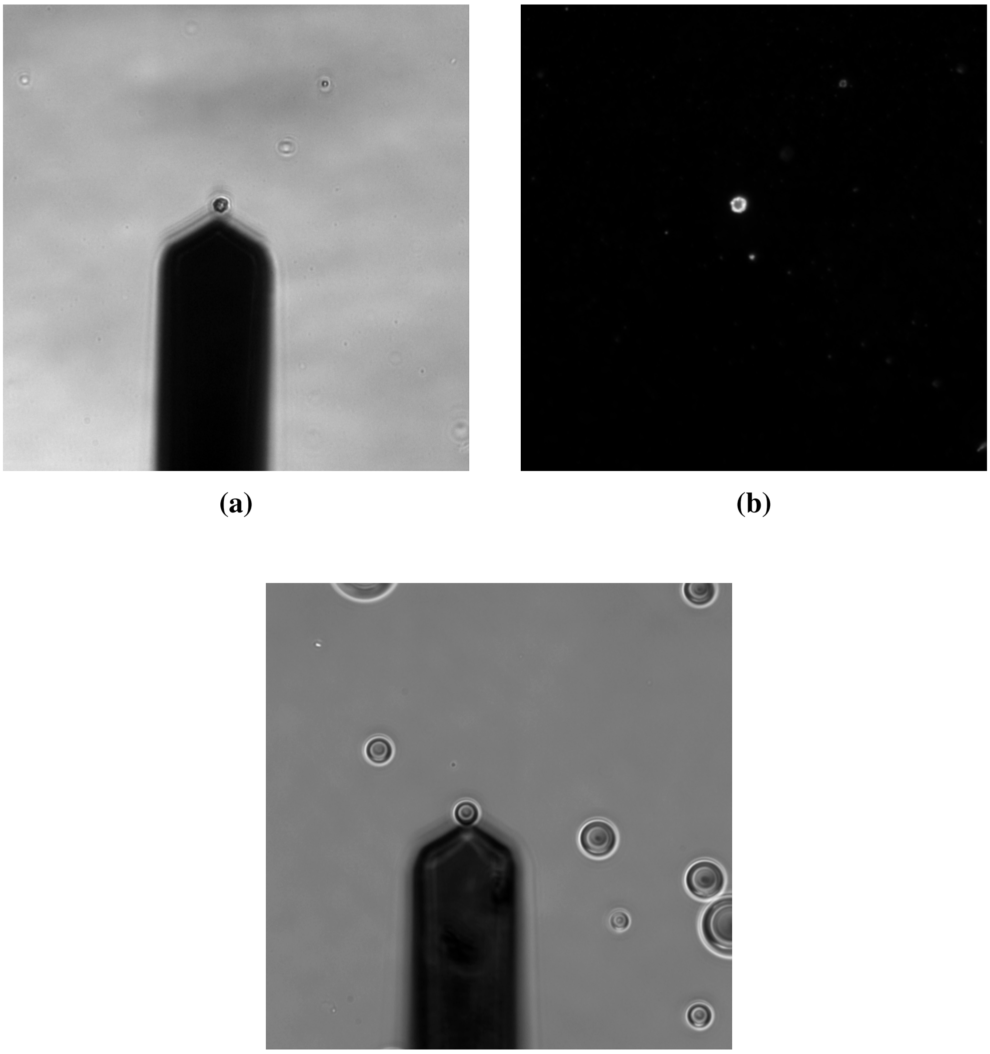

(a) (b)

(c)

Figure 3.1: Three different images of the microbubbles; a) an example of microbubbles containing nanoparticles images in brightfield, b) the same bubble in fluorescence microscopy and c) the commercial SonoVue®.

Figure 3.1 shows the difference between the GB nanoparticles batches and the phospholipid monolayer of SonoVue®. The appearance of the nanoparticle microbubbles is much more ragged and when viewed with fluorescence show illuminating beads at the rim of the microbubble.

3.2 Shell Thickness

Three different shell thicknesses are used the results to follow where two are gathered from litterature. The SonoVue® shell thickness is taken to be 4 nm [33]. Secondly the pure protein microbubbles of the J6 batch were approximated to the shell thickness of Albunex® another protein bubble, which provides a value of 15 nm [34]. Lastly the GB batches containing nanoparticles were investigated using a microscope with high resolution.

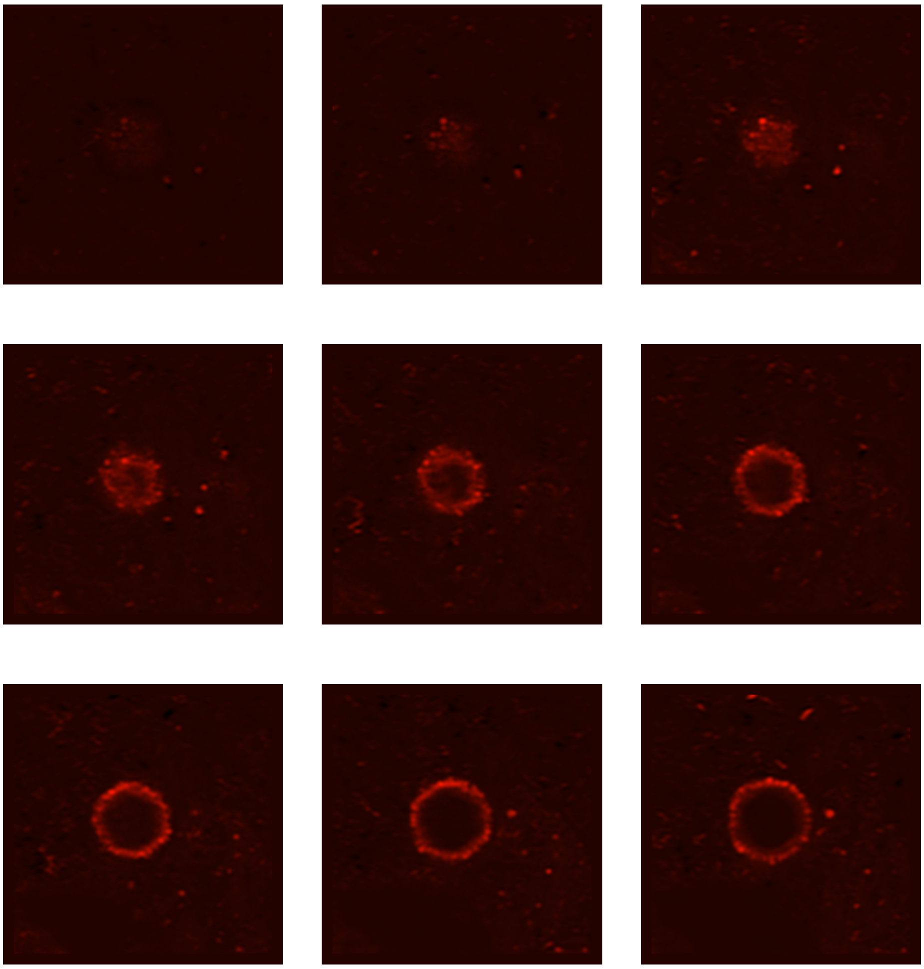

Figure 3.2: Consecutive Z-stack images of a microbubble produced by the ultra-turrax procedure of the GB batches.

Taking the full-width at half maximum of the shell by intensity measures done on the z-stack in Figure 3.2 gave a value of approximately 300 nm. These images were taken with the use of a Zeiss LSM 800 (Zeiss, Oberkochen, Germany) fitted with an airy scan detector.

3.3 Atomic Force Microscopy

3.3.1 Sample Preparation

The sample preparation was done in line with the project work which was in turn inherited from Finnøy [35] [36]. Initially a WillCo-dish® (WillCo Wells BV, Amsterdam, The Netherlands) is rinsed by the use of isopropanol. After adding the isopropanol the dish is left for two to three minutes before being rinsed with Milli-Q® (Merck KGaA, Darmstadt, Germany). In order to adhere to the microbubbles the surface of the dish must be covered in polythylenimine, this is left for a longer stretch of time to be sufficiently applied, approximately 10-15 minutes. While the polethylenimine is resting, the microbubbles are extracted from the container and placed in a 10 ml container of Milli-Q® water. The amount extracted is typically in the range of 10 to 100 microliters. Making sure that the surface of the water arcs on top of its container the WillCo-dish® can be up-ended upon this bath, after being rinsed with Milli-Q® water. Buoyancy will then ensure that the microbubbles rise to the surface of the dish and attaches to the polyethylenimine. Depending on the initial concentration of the bubbles that are to be investigated and the desired density of microbubbles during the AFM measurements the dish can be left on top of the bath for three to ten minutes.

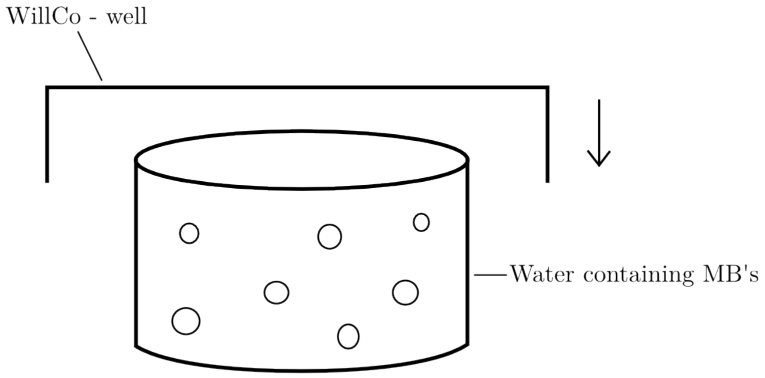

Figure 3.3: Illustration of the sample preparation pertaining to the AFM experiments. The figure depicts the attachment of the microbubbles to the WillCo-dish®.

3.3.2 Measurements

During the AFM experiments the microbubbles were observed through an optical microscope, Zeiss Axio Observer D1 (Zeiss, Oberkochen, Germany), and single microbubbles that showed no inherent deformation were chosen as ramp subjects. The ramping was done with flat cantilevers, as the theoretical models are well approximated to the force between two spheres where one can be considered infinite. A flat cantilever may also lessen the strain on localized parts of the shell, causing unwanted deformation and destruction. The cantilevers used in the measurements were of the type NSC12 (MicroMash, Madrid, Spain), fitted to a Bioscope Catalyst® (Bruker, Billerica, MA, USA). The cantilever spring constant was determined by thermal tuning in fluid. Over the course over the measurements the spring constant was varied between a stiff 5.622 N/m to the softer 0.4048 N/m to investigate possible effects. Another variable was the maximal force that was applied with each compression. This was varied between 40 nN and 400 nN, with the frequency being set to a constant 0.5 Hz, which yielded ramp velocities of approximately 6 µm/s. Each microbubble suffered 20 compressions and was imaged both before and after. Before initializing the ramps the MB's were confirmed to contain nanoparticles by fluorescence microscopy, a simple switch controlling the change between this mode and bright field on the microscope. To standardize the visual appearance of the microbubbles the magnification was kept at 40x in addition to a 1.6x factor added optovar.

3.3.3 Data Analysis

The four different models of Reissner, Hertz, Elastic membrane and de Jong theory was programmed into MatLab®. For the two models that gather the microbubble stiffness directly from the force curves of the AFM, a linear regression was performed up to a set value of the relative deformation, indentation divided by diameter. This value was set to 0.1 for all the calculations performed and so the values obtained are all within the low-deformation regime. The simple regression option was chosen i order to account for the multiple linear regions that occur during compression of the nanoparticle microbubbles in particular . In the two following models of elastic membrane theory and Hertz theory, however, this simple linear regression was found to be inadequate. In these models the relative deformation of a set power was plotted against the force, giving a nonlinear x-axis. This elegant way of defining the linear region for these models was adapted from Morris [37]. When a non-linear axis is employed it becomes clear that the first section of the contact curve can safely be excluded as it does not appear linear. The linearity was found to increase towards the set cut-off point at a relative deformation of 0.1. Taking this into account a forward-winding regression was made from the first point of contact with the microbubble and towards the 0.1 limit. A strict coefficient of determination, R^2, of 0.996 was found to produce linear regions for all but a few microbubbles. In the case where this could not be obtained the microbubble curves were flagged for inspection. The cause of some microbubbles not fitting was found to be due to a separate linear region occuring around the 0.1 limit and so for these microbubbles only the last four points are used to perform the linear regression. It was opted to still include these microbubbles in the datasets so as not to hide behavioural characteristics. Figure 3.4 shows how the slope was determined.

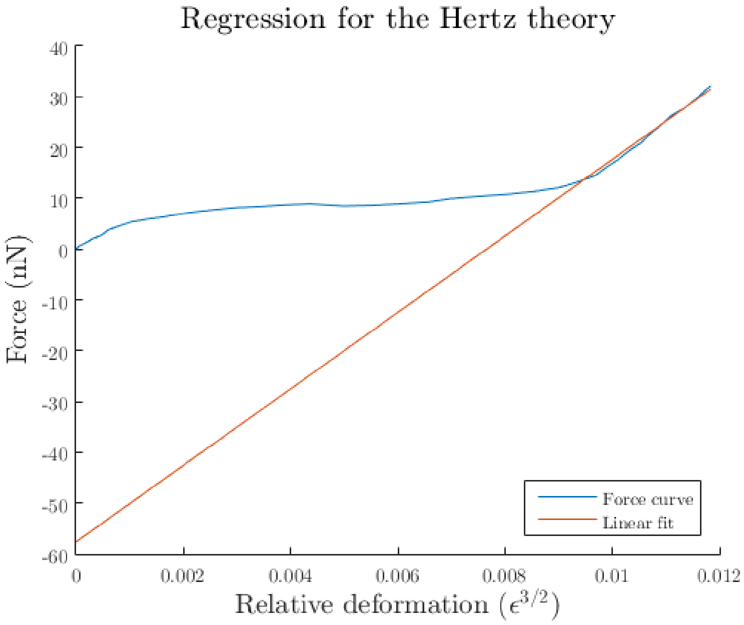

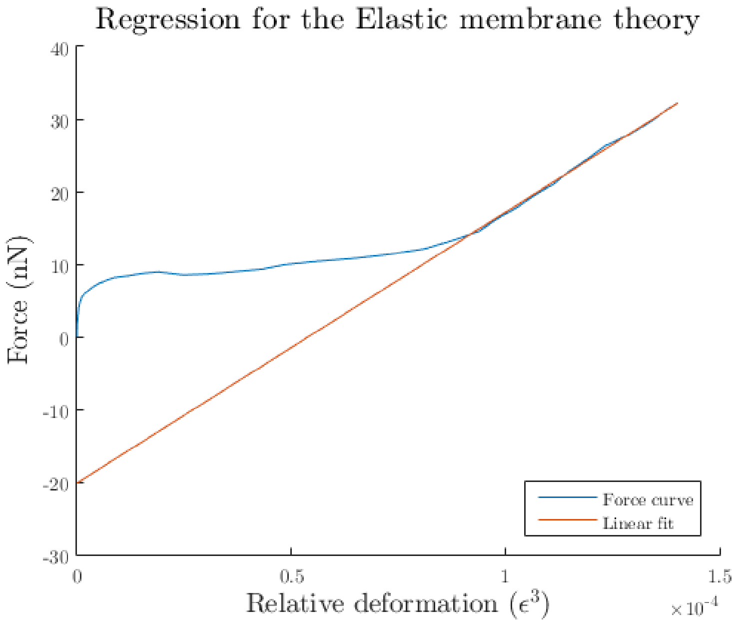

Figure 3.4: Two examples of the fits done for the Hertz theory and elastic membrane theory, plotted with a non-linear axis.

3.4 Backscatter Measurements

The backscatter measurements are done in a custom built water tank that houses a sample chamber and two slots for a transmitting and receiving transducer. The transmitting transducer is placed orthogonally to the chamber wall emitting ultrasound into the microbubbles after travelling the distance between the transducer and chamber in degassed water. The microbubble respone is captured by a second transducer, located approximately 45° above the transmitting transducer in the tank roof. To avoid ultrasound reflecting back from the far wall this side of the tank has an angle, so that the pressure waves may disperse away from the receiving transducer, minimizing noise. The sample chamber is a 3 x 3 x 80 cubic centimeter container, which during the backscatter measurements was filled with 60 ml PBS. The microbubble concentration was 1.15 million bubbles per 60 ml.

A sine wave of two or twenty cycles and with a nominal voltage from 25 mV to 700 mV was passed unto the transmitting transducer from an Agilent® 33500B Series (Agilent Technologies, Penang, Malaysia). Depending on the transducer characteristics this voltage corresponds to a pressure being applied to the microbubbles. This signal was amplified with a RF Power Amplifier, Model 2100L(ENI, Rochester, USA). After a measurement was performed on the amplifier it was found to produce a 160x amplification with a nominal 50 dB. From here the signal excites the transducer and the pressure waves reaches the microbubbles, causing them to oscillate. The pressure waves generated from these dynamics are captured by the receiving transducer and from there transported to a pulse receiver of the model 5900PR (Panametrics, Waltham, USA). The amplification in this link is a nominal 54 dB. Finally the waveform is captured by the LeCroy® oscilloscope, a Waverunner LT262 (LeCroy, Long Branch, USA). In total, three different transducer pairs were utilized for the backscatter measurements. The pairs were, on the form of transmitting/receiving, 1MHz/5MHz, 3.5MHz/5MHz and 5MHz/10MHz.

A total of 15 pulses were captured for each pressure level and subsequently analysed in MatLab® (Mathworks, Natick, USA). The pulses were first averaged and then subjected to a Hanning-window. Lastly a Savitzky–Golay filter was applied to smooth the energy density spectra.
Figure 3.5 shows how the measurements are performed and the instrument chain.

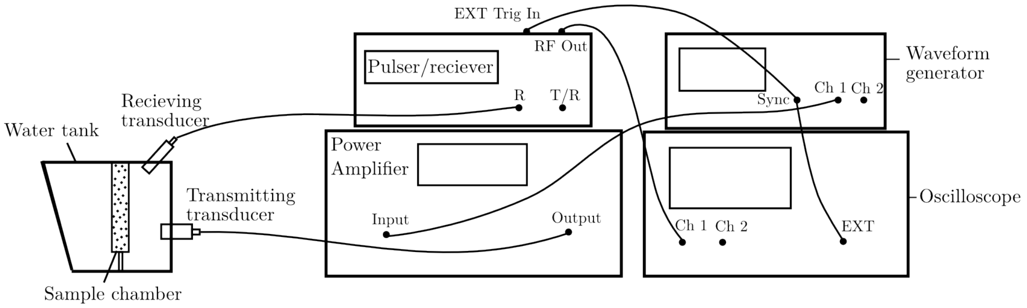

Figure 3.5: The backscatter measurement setup.

3.5 Attenuation Measurements

The experimental setup for the attenuation measurements is not dissimilar to that of the backscatter setup, as they both use the same water tank. However the instrument chain is different and an important difference is the single transducer, used for both transmitting and receiving. In addition, a solid backplate is lowered into the tank to reflect the pressure waves back into the transducer. Again a sine wave is generated with the signal generator described in the backscatter measurements. The amplitude is, however, now set to 10 volts, as there is no amplifier before the signal reaches the transducer. As for the pulse frequency this was set to 0.1 ms. The frequency outputed from the signal generator corresponds to the center frequency of the transducer, in these measurements 5 MHz. After the pressure waves have traversed the sample chamber twice, to the backplate and back, they are picked up by the same transducer and captured by the oscilloscope. The signals were averaged 128 times by the oscilloscope before being transferred to the computer. Measurements were done in evenly spaced intervals ranging from seconds after microbubbles being added to 18 minutes. The microbubble concentrations was either 1 million microbubbles or 10 million microbubbles per 50 ml. The datanalysis was again done by a program written in MatLab® and the spectral difference method was used to compute the attenuation across different frequencies. The crux of this method is the basis of a reference signal, obtained of the chamber without microbubbles present, which is divided by the signal with microbubbles. The difference in magnitude is then divided by the chamber length and so the attenuation per centimeter is obtained. In Figure 3.6 the setup is depicted with its single transducer and backplate key features.

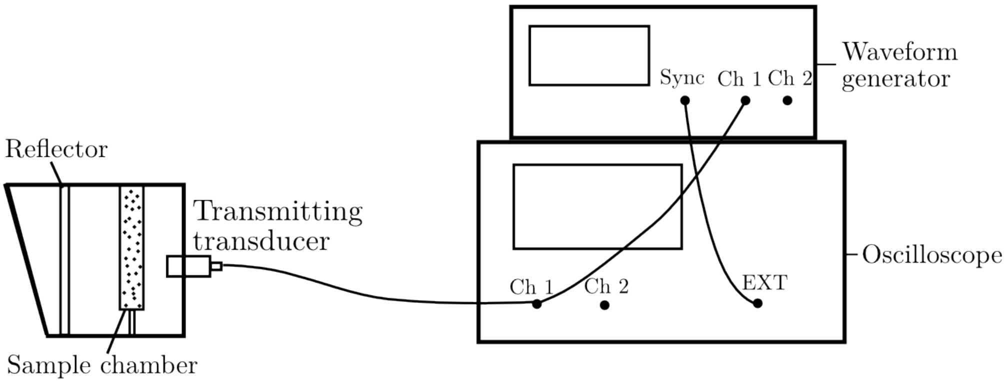

Figure 3.6: The attenuation measurement setup.

3.6 Automation

The initial part of the thesis work consisted of automating the acoustic setup. After unsuccessful attempts using industry software the file formats were deemed incompatible with modern solutions and a workaround had to be implemented. A satisfactory system setup was acquired through the use of desktop automation and using this to control the oscilloscope default software. The program used for this was the open source AutoHotKey, providing a significantly more friendly user environment with its intuitive script-syntax. The result of this endeavour is the ability to send commands to the oscilloscope on timed intervals, providing a boost to the temporal resolution when doing experiments as well as eliminating the human error when timing sequences.

Chapter 4

Results

4.1 Atomic Force Microscopy

The results presented in this section were obtained by the use of atomic force microscopy. The GB-batches were all produced with the same production method from SINTEF, the J6 batch was also produced with the standard procedure, but only contains BSA as surface stabilizer. In-house produced UCA's are compared to the commercially available SonoVue.

4.1.1 Force Curves

Figure 4.1 shows the difference between the force curve of the monolayered SonoVue® bubbles and the nanoparticle containing GB 167. While the GB 167 is prone to display several plateau regions the SonoVue® response is marked by a steadily increasing curve. This tendency is one of the major obstacles when modelling the nanoparticle microbubbles as defining the representative linear region is no trivial task.

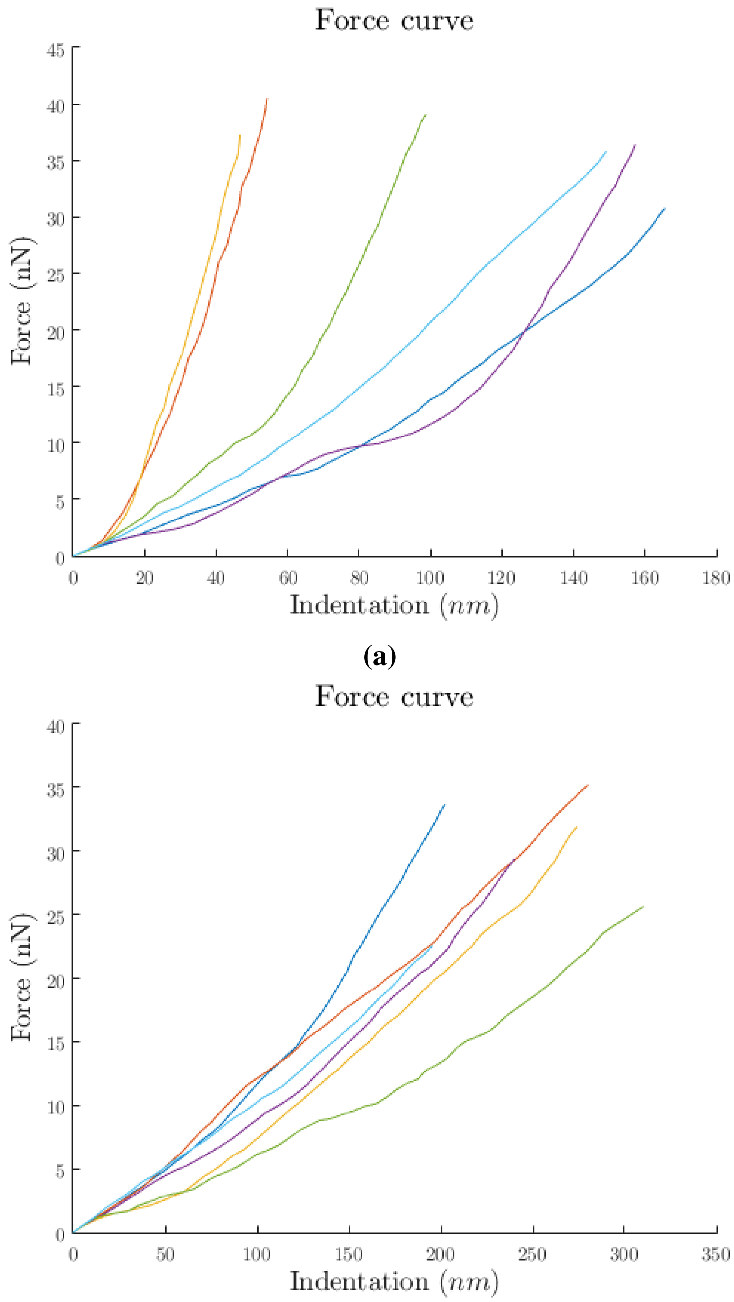

(a)

(b)

Figure 4.1: Six representative force curves for the a) perfluoropropane microbubbles with nanoparticles and b) the phospholipid monolayered SonoVue®. The force curves were gathered from the GB 167 batch and the 40 nN SonoVue® experiments.

4.1.2 GB 160, PFC With NP

The GB 160 batch was analysed using the Reissner theory in the previous project work, but is re-analysed here to include the other three models.

As shown if Figure 4.2 the Reissner model and Hertz model compute similar values of the Young's Modulus in the range of approximately 0.3 to 10 MPa. However it's important to remember that the Hertz theory evaluates the stiffness as being a homogeneous sphere and the Reissner theory that of the shell. The elastic membrane theory shows a very large spread with a possible outlier at 1415 MPa. The model of de Jong gives values in the range of 6 to 55 kPa. Of all the models the Hertz theory and de Jong model give the clearest linear relationships with the microbubble diameter, both showing a significant correlation. The Hertz theory has the lowest p-value, with the Young's Modulus sinking with increasing diameter. The ranges and p-values of the Pearson correlation are given in Table 4.1.

Table 4.1: The theoretical models and their respective Young's Modulus and Pearson correlation p-values computed for batch GB 160

Model	**Young's Modulus**	**p-value**
Reissner	0.98-7.5 (MPa)	0.17
Hertz	0.29-10.0 (MPa)	0.00375
Elastic membrane	2.9-1415.8 (MPa)	0.20
de Jong	6.43-55.49 (kPa)	0.00644

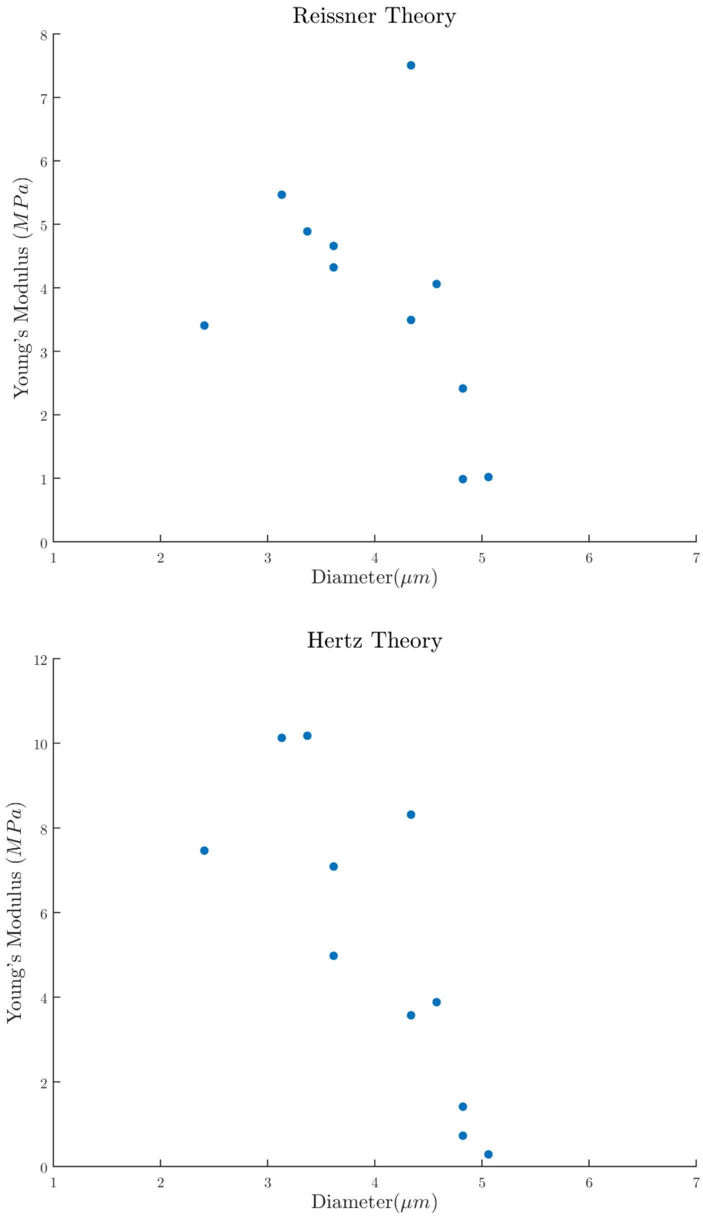
Reissner Theory
Young's Modulus (MPa)
0
1
2
3
4
5
6
7
8
1
2
3
4
5
6
7
Diameter(μm)
Hertz Theory
Young's Modulus (MPa)
0
2
4
6
8
10
12
1
2
3
4
5
6
7
Diameter(μm)

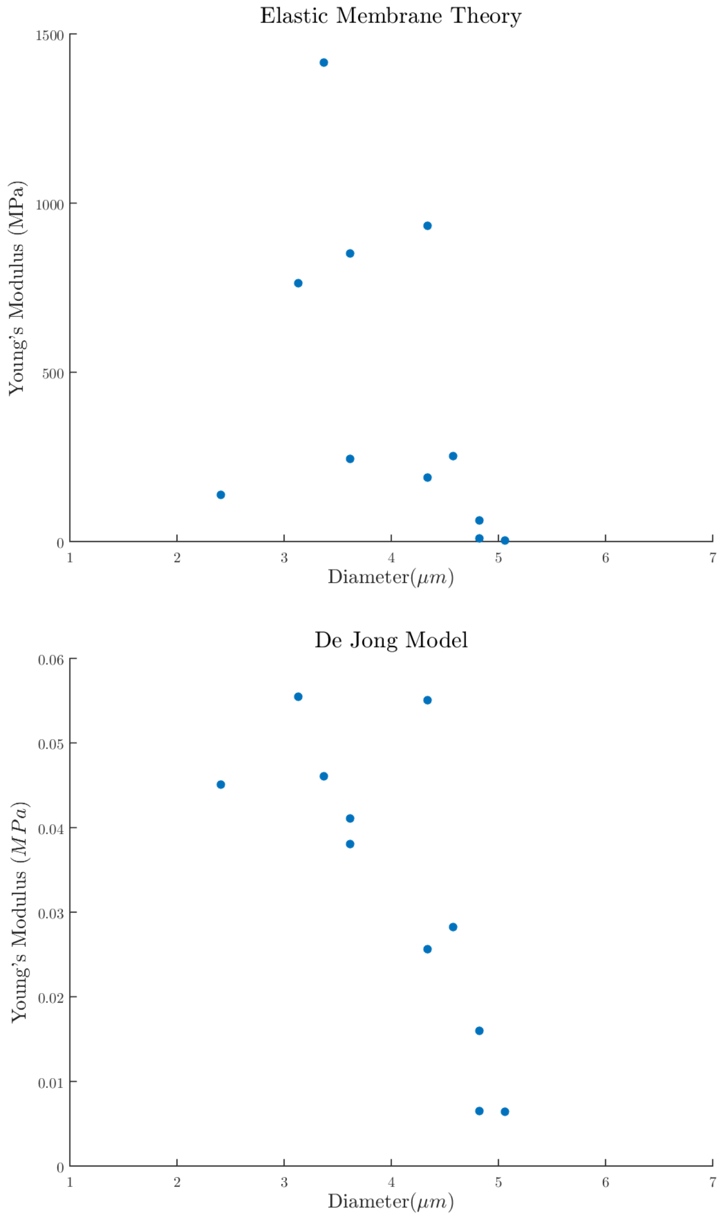

Figure 4.2: The Young's Modulus of GB 160 for each microbubble plotted against its diameter using the four different models with spring constant K_c = 0.2656 N/m

4.1.3 GB 161, PFC With NP

The GB-161 batch represents the standard production technique of 1% NP's and 1% casein with perfluorocarbon. The data obtained for this batch was limited. This may be caused by both the sample preparation and the size distribution of the batch. For the following experiments the spring constant of the cantilever was $K_c = 5.622$ N/m and the maximum applied force was 40 nN.

Figure 4.3 shows no clear relationship between the radius and Young's Modulus and this is backed up by the poor p-values in Table 4.2. The poor fits are to be expected, however, with the limited amount of available data. The different Young's Modulus ranges show that the Reissner and Hertz model both predict moduli within 1-10 MPa. The elastic membrane theory produces a wide range from single digit to hundreds of MPa and the de Jong method values in the range of tens of kPa.

Table 4.2: The theoretical models and their respective Young's Modulus and Pearson correlation p-values computed for batch GB 161.

Model	**Young's Modulus**	**p-value**
Reissner	1.24-4.05 (MPa)	0.88
Hertz	2.13-9.45 (MPa)	0.11
Elastic membrane	62.54-355.47 (MPa)	0.63
de Jong	12.63-55.49 (kPa)	0.35

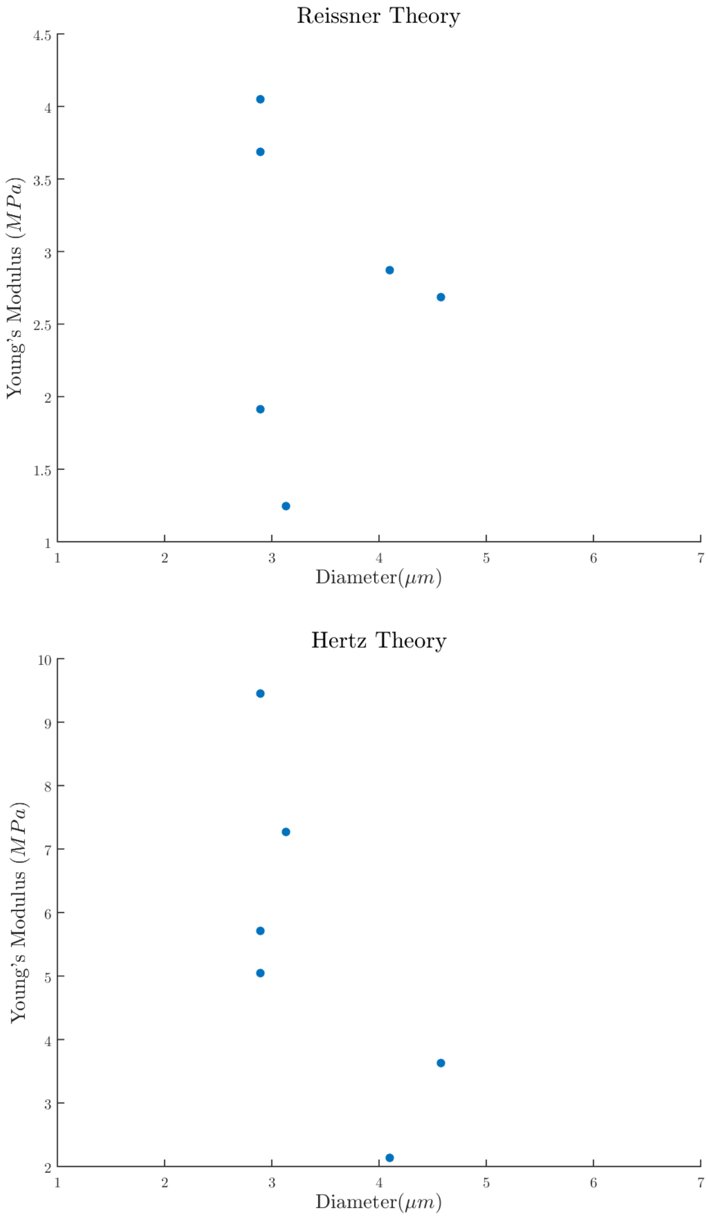
Reissner Theory
Young's Modulus (MPa)
4.5
4
3.5
3
2.5
2
1.5
1
1
2
3
4
5
6
7
Diameter(μm)
Hertz Theory
Young's Modulus (MPa)
10
9
8
7
6
5
4
3
2
1
2
3
4
5
6
7
Diameter(μm)

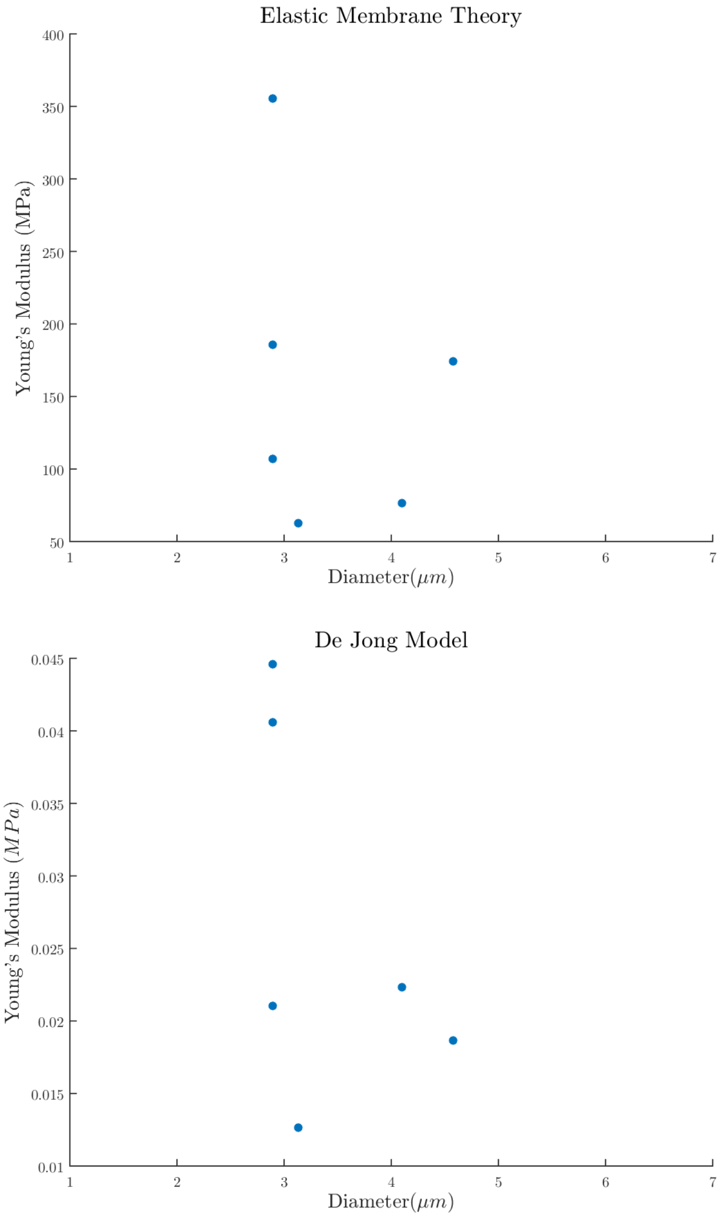

Figure 4.3: The Young's Modulus of GB 161 for each microbubble plotted against its diameter using the four different models with spring constant $K_c = 5.622$ N/m

4.1.4 GB 162, PFC With NP, Day One

GB-162 is the third batch of PFC microbubbles to be analyzed in the same manner as the aforementioned two. The spring constant was kept at $K_c = 5.622$ N/m with a maximal force of 400 nN. This batch was analysed over two days to investigate if prolonged storage has any impact on the Young's Modulus or general stability of the microbubbles.

The first day sees yet another agreement between the Reissner theory and Hertz as shown in Table 4.3, with values of approximately 1-15 MPa. The elastic membrane theory shows a decreased span compared to the previous batches of 3-73 MPa. A range of 10-133 kPa shows an increase in the span of the predicted Young's Modulus according to the de Jong method. As observed in Figure 4.4 there is no obvious linear relationship as is confirmed by the p-values in table 4.3.

Table 4.3: The theoretical models and their respective Young's Modulus and Pearson correlation p-values computed for batch GB 162, day one.

Model	Young's Modulus	p-value
Reissner	0.9-10.08 (MPa)	0.32
Hertz	0.62-14.57 (MPa)	0.13
Elastic membrane	3.01-73.64 (MPa)	0.43
de Jong	10.8-133.11 (kPa)	0.29

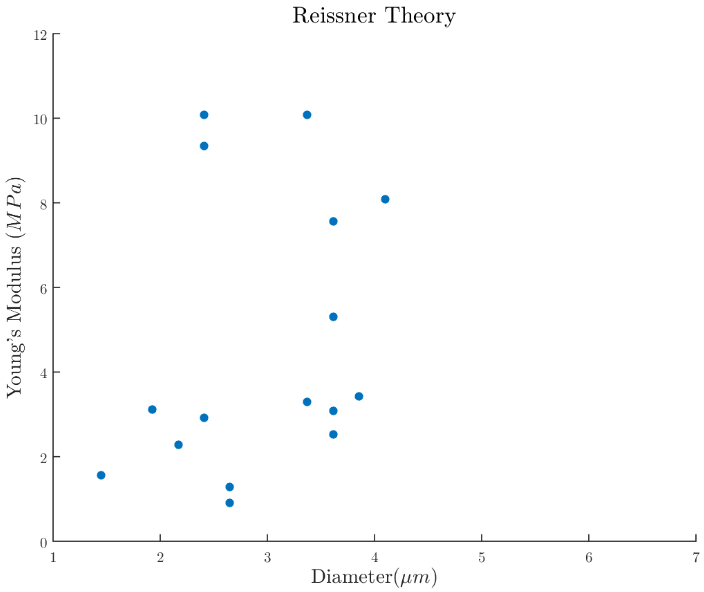
Reissner Theory
Young's Modulus (MPa)
0
2
4
6
8
10
12
1
2
3
4
5
6
7
Diameter(μm)

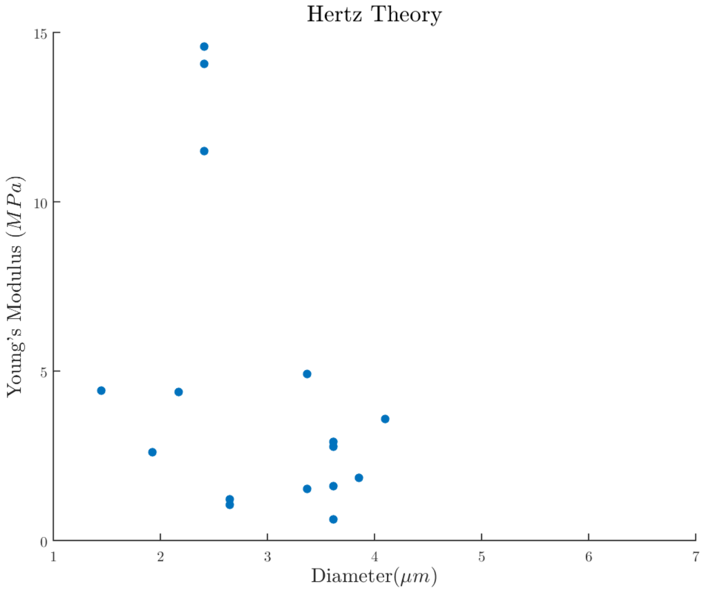
Hertz Theory
Young's Modulus (MPa)
0
5
10
15
1
2
3
4
5
6
7
Diameter(μm)

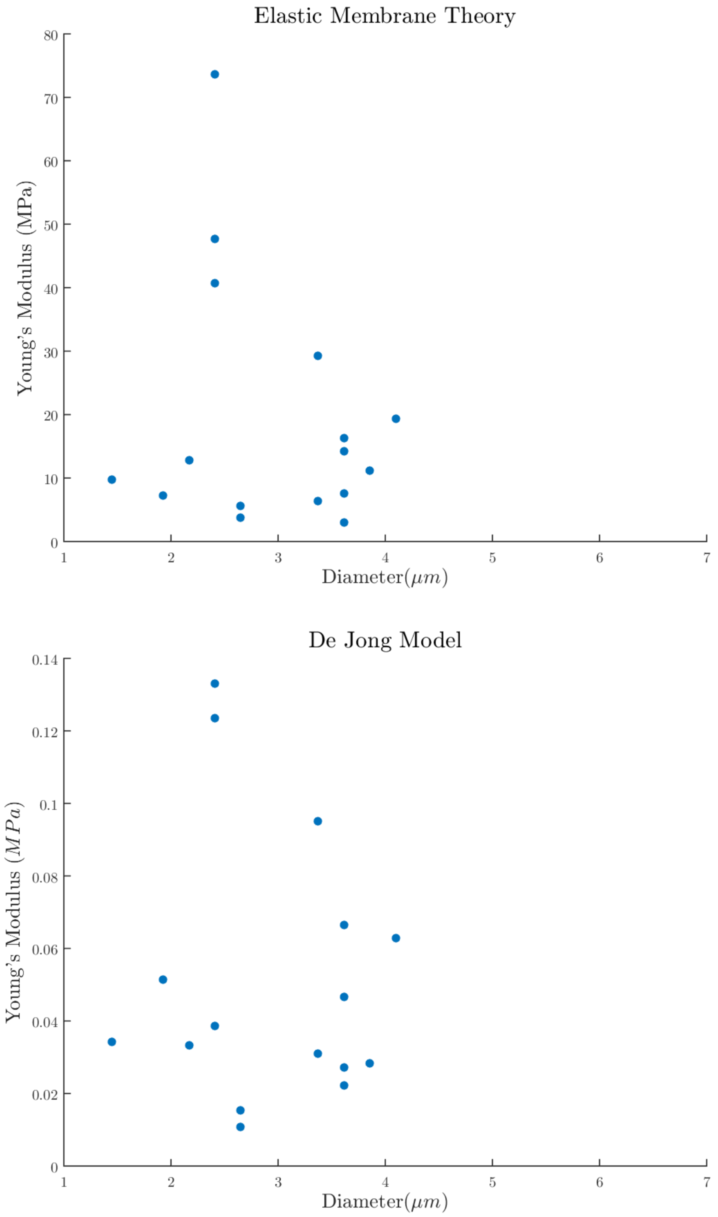

Figure 4.4: The Young's Modulus of GB 162, day one, for each microbubble plotted against its diameter using the four different models with spring constant $K_c = 5.622N/m$

4.1.5 GB 162, PFC With NP, Day Two

Two days later the GB 162 batch was revisited and the procedure of this series is identical to that of the first day with a cantilever spring constant of $K_c = 5.622$ N/m and maximal force 400 nN.

The Young's moduli calculated for day two shows that the Hertz theory produces a significant linear relationship as illustrated in Figure 4.5 and the p-values of Table 4.4. The de Jong model also produces a significant p-value. The range of the Young's Moduli are highly consistent with the findings of day one and mirror the values closely. Again the two significant p-values show the Young's Modulus declining with increasing diameter.

Table 4.4: The theoretical models and their respective Young's Modulus and Pearson correlation p-values computed for batch GB 162, day two.

Model	Young's Modulus	p-value
Reissner	0.82-8.31 (MPa)	0.21
Hertz	0.3-20.65 (MPa)	0.01
Elastic membrane	1.58-67.68 (MPa)	0.15
de Jong	7.26-137.16 (kPa)	0.014

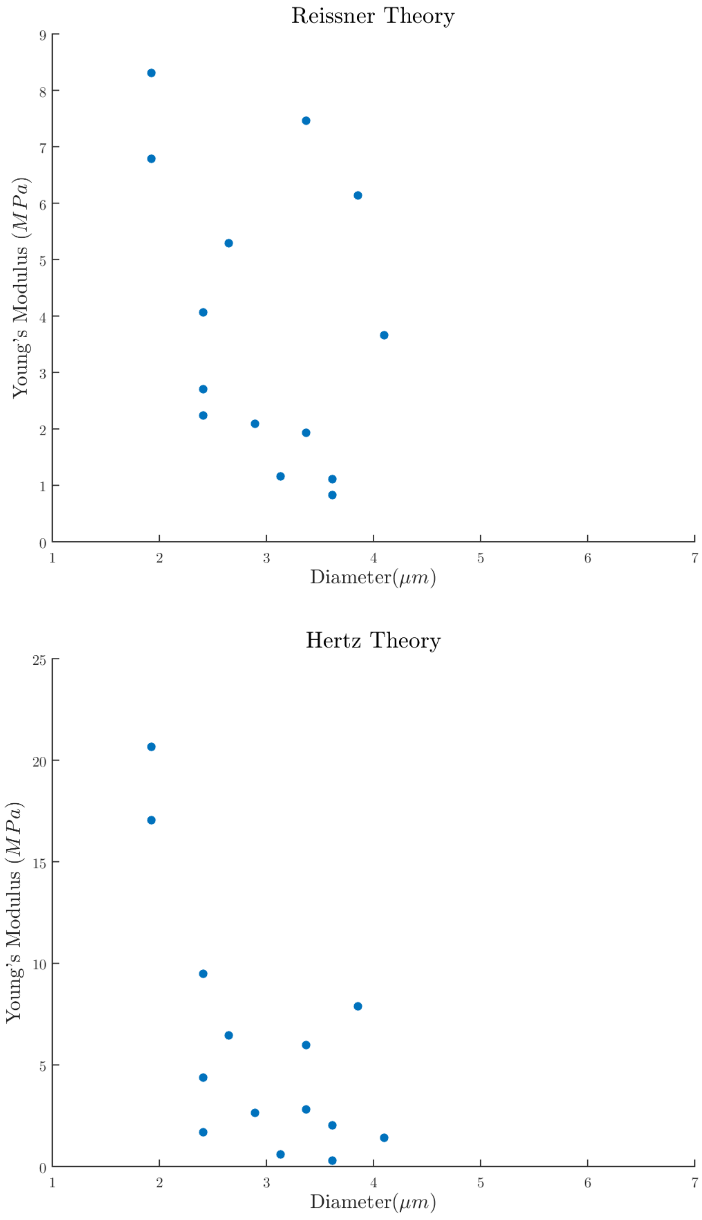
Reissner Theory
Young's Modulus (MPa)
0
1
2
3
4
5
6
7
8
9
1
2
3
4
5
6
7
Diameter(μm)
Hertz Theory
Young's Modulus (MPa)
0
5
10
15
20
25
1
2
3
4
5
6
7
Diameter(μm)

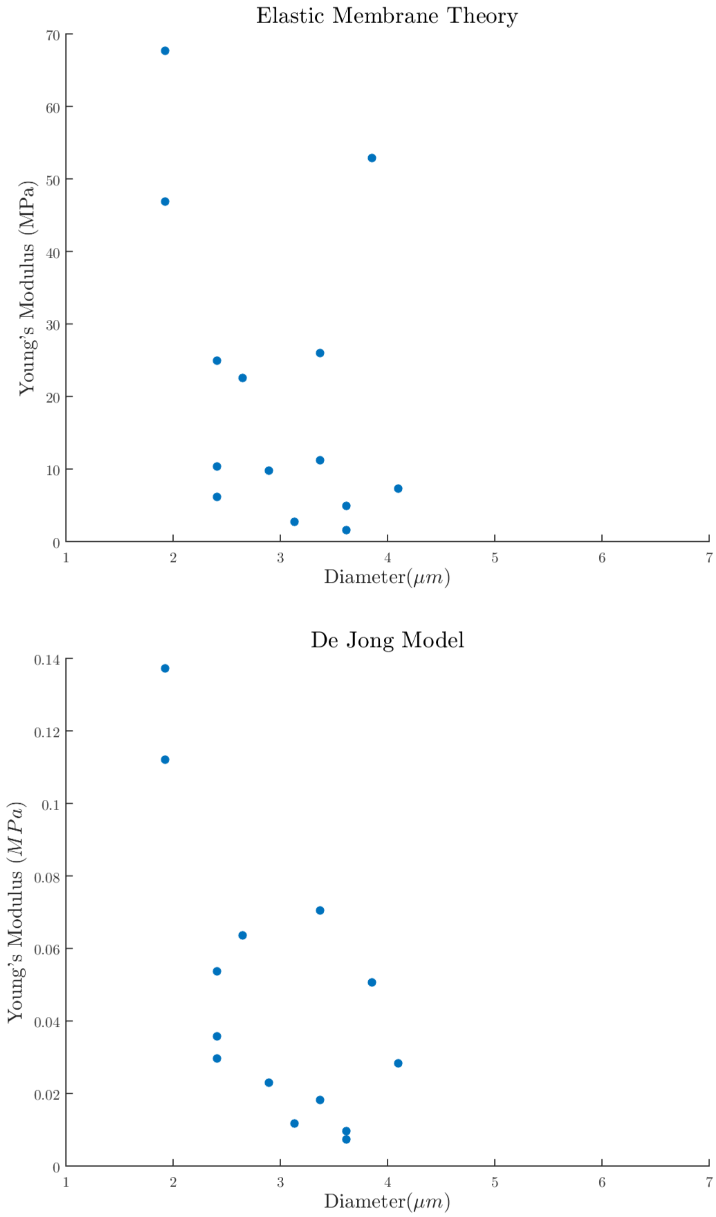

Figure 4.5: The Young's Modulus of GB 162, day two, for each microbubble plotted against its diameter using the four different models with spring constant $K_c = 5.622$ N/m

4.1.6 GB 167, PFC With NP

The last batch to be analysed from the PFC and NP production method was the GB 167 batch. Returning to a lower maximum force of 40 nN the cantilever spring constant for this experiment was 0.4048 N/m. This allows for comparisons both of peak load, cantilever stiffness and loading rate.

The Hertz theory provides a very good linear fit for this batch of microbubbles as can be seen from Figure 4.6, as does the de Jong model. This is backed up by the p-value from the correlation function as seen in Table 4.5. The ranges are in line with what has previously been described, the range of the Hertzian Young's modulus is extended, but this is due to the possible outlier at approximately 50 MPa. It is interesting to note the tendency of the elastic membrane theory to provide very wide ranges for low peak forces and hence loading rate yet produce a better linear correlation. As is the case here, with a lower spring constant and the relatively low peak force of 40 nN.

Table 4.5: The theoretical models and their respective Young's Modulus and Pearson correlation p-values computed for batch GB 167.

Model	Young's Modulus	p-value
Reissner	0.94-7.11 (MPa)	0.23
Hertz	1.55-47.06 (MPa)	0.00674
Elastic membrane	22.9-2395.34 (MPa)	0.091
de Jong	11.24-115.43 (kPa)	0.025

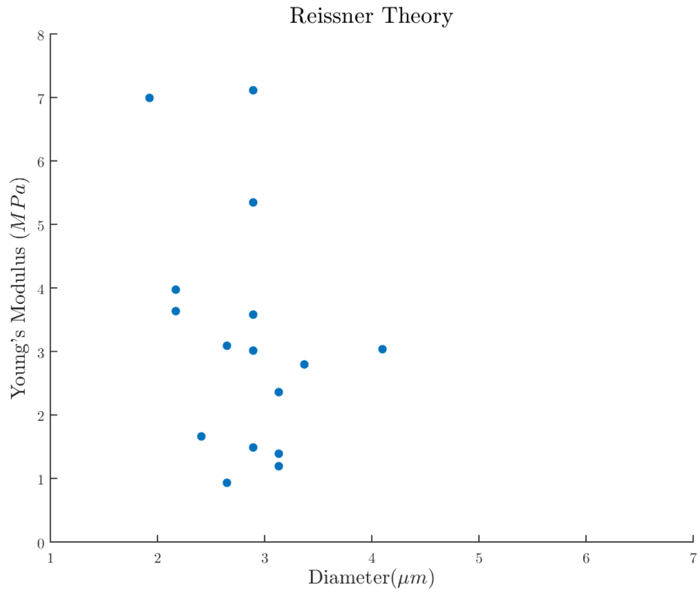
Reissner Theory
Young's Modulus (MPa)
0
1
2
3
4
5
6
7
8
1
2
3
4
5
6
7
Diameter(μm)

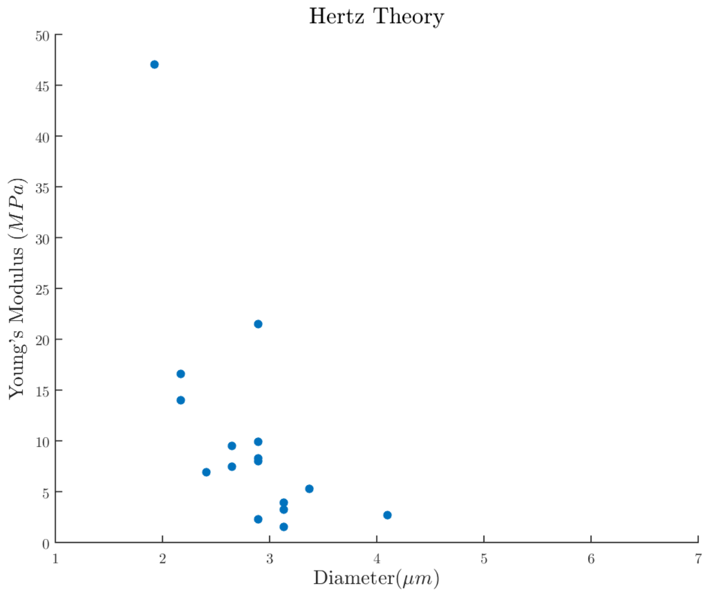
Hertz Theory
Young's Modulus (MPa)
0
5
10
15
20
25
30
35
40
45
50
1
2
3
4
5
6
7
Diameter(μm)

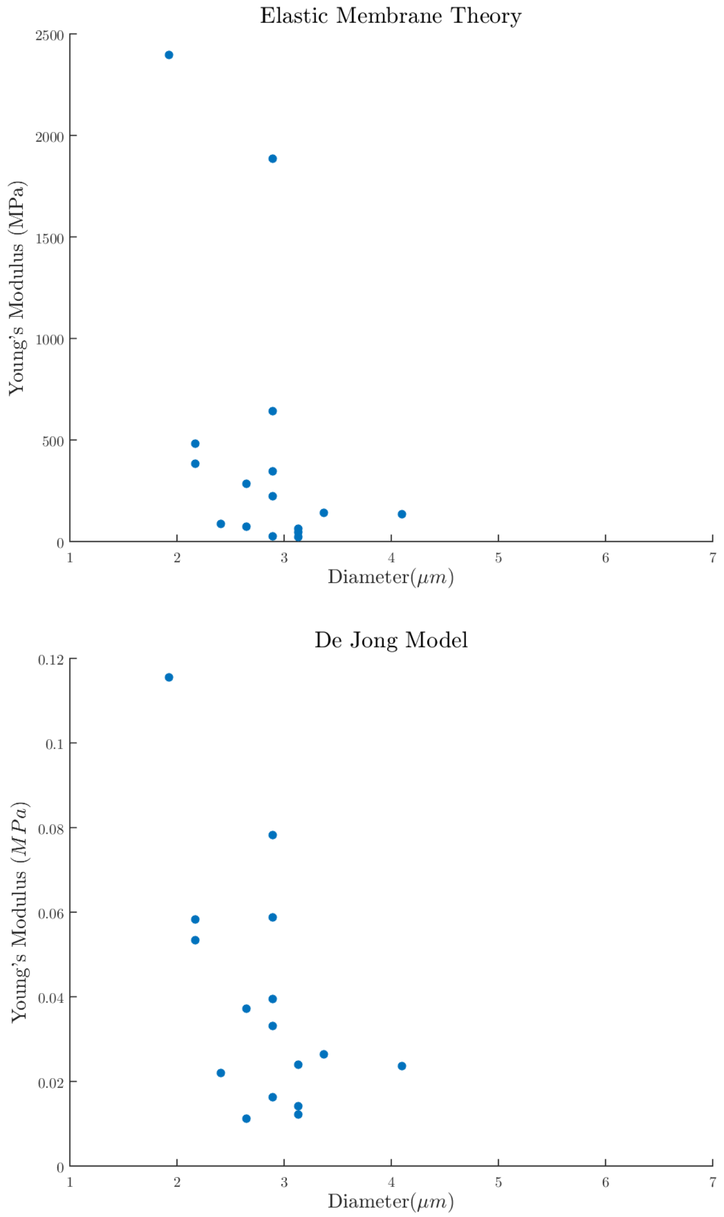

Figure 4.6: The Young's Modulus of GB 167 for each microbubble plotted against its diameter using the four different models with spring constant $K_c = 0.4048$ N/m

4.1.7 J6, BSA

The J6 batch was, in addition to the GB 160 PFC microbubbles, analysed in the project work, but provide an opportunity to examine the differences between microbubbles containing nanoparticles and those that do not. The J6 batch consists of PFC microbubbles with a shell made up of only BSA protein. The shell thickness is therefore taken from literature to be 15 nm, approximately a monolayer of proteins seen in similar UCA's. The spring constant used in these experiments was 0.2656 N/m and the peak force 40 nN.

The Reissner theory predicts a higher value for the shell Young's Modulus that those seen for the GB bubbles containing NP's, indicated in Table 4.6. Total microbubble stiffness, as calculated by the Hertz model, however, seems to have decreased. The elastic membrane theory seems to be in line with the Reissner approach. No apparent relationship can be said to be obtained from the scatter plots in Figure 4.7 between the Young's Modulus and diameter.

Table 4.6: The theoretical models and their respective Young's Modulus and Pearson correlation p-values computed for batch J6 BSA.

Model	Young's Modulus	p-value
Reissner	155.27-418.64 (MPa)	0.11
Hertz	0.47-2.6 (MPa)	0.73
Elastic membrane	33.82-219.93 (MPa)	0.5
de Jong	107.02-230.29 (kPa)	0.94

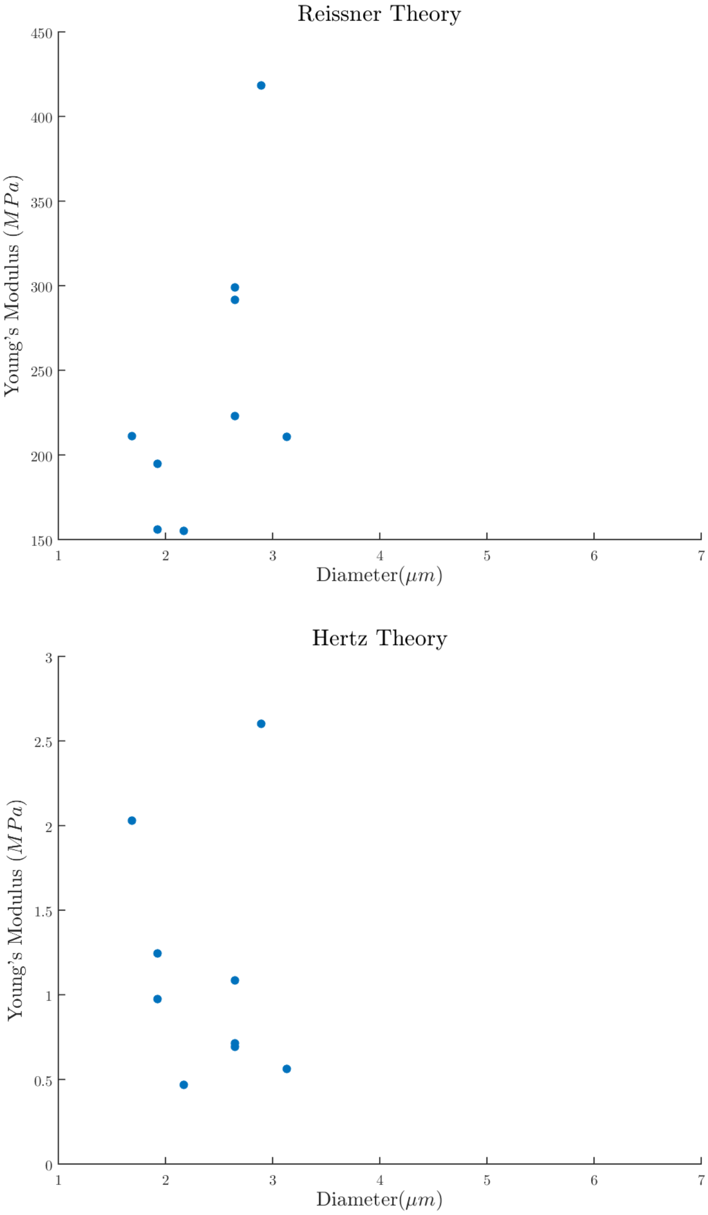
Reissner Theory
Young's Modulus (MPa)
450
400
350
300
250
200
150
1
2
3
4
5
6
7
Diameter(μm)
Hertz Theory
Young's Modulus (MPa)
3
2.5
2
1.5
1
0.5
0
1
2
3
4
5
6
7
Diameter(μm)

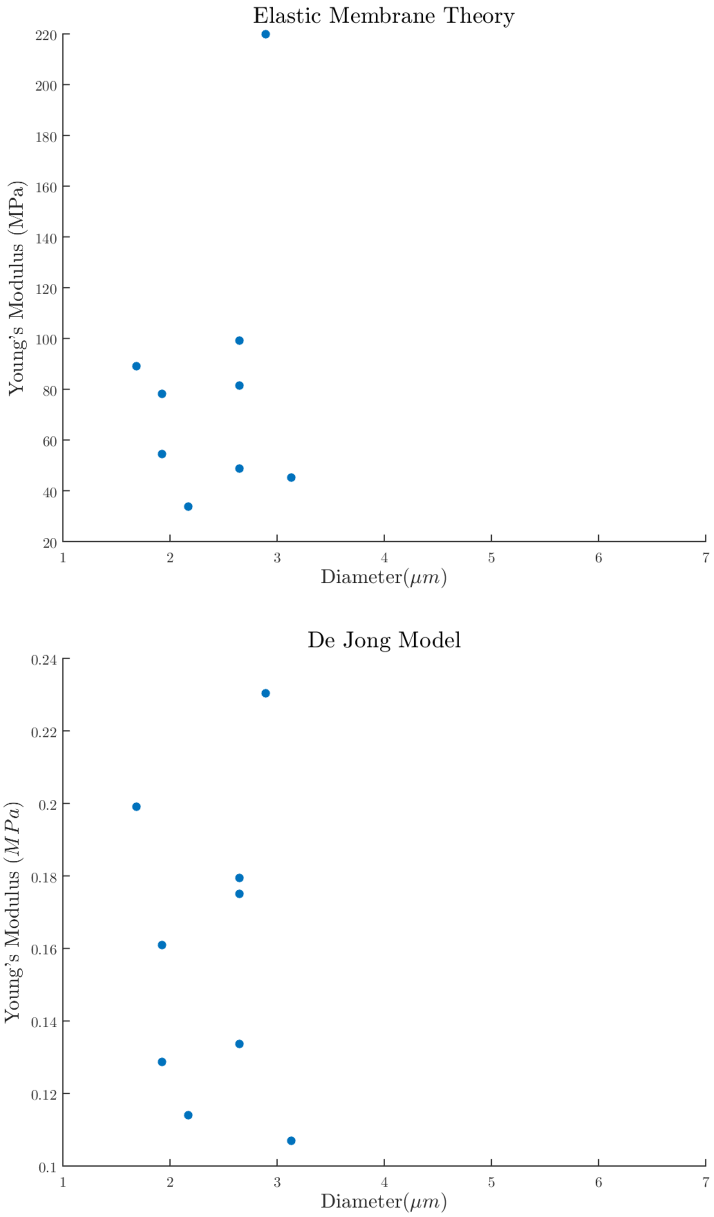

Figure 4.7: The Young's Modulus of J6 BSA for each microbubble plotted against its diameter using the four different models with spring constant $K_c = 0.2656$ N/m

4.1.8 SonoVue

SonoVue® was chosen as a commercially available comparison for the GB batches as well as the pure protein J6. SonoVue® has a well documented set of characteristics and has been widely used in other studies. In addition to this, SonoVue® is thought to be a good fit for the models used, with the criteria being met to a larger degree. The assumed shell thickness for SonoVue® is taken to be a monolayer of phospholipids, 4 nm. The spring constant was varied with different experiments as previously, so was the peak force. Measurements were also done on SonoVue® using a cantilever spring constant of $K_c = 0.4238$ N/m, with a peak load of 150 nN. This caused microbubble destruction in three out of four microbubbles and so the peak load was lowered to 40 nN.

The following plots represent the first day of a two-day measurement series, again to investigate any possible changes in microbubble features during storage. Figure 4.8 shows that all models calculate the SonoVue® microbubbles to have a higher Young's Modulus than for the previous microbubble batches, except for the Hertz model, which shows a decrease for the total MB stiffness. P-values charted in Table 4.7 gives a significant linear relationship only for the Reissner theory. The range of the elastic membrane model is drastically affected by what may be an outlier.

Table 4.7: The theoretical models and their respective Young's Modulus and Pearson correlation p-values computed for SonoVue® day one.

Model	**Young's Modulus**	**p-value**
Reissner	3.98-7.13 (GPa)	0.036
Hertz	0.32-0.81 (MPa)	0.54
Elastic membrane	226.29-8751.72 (MPa)	0.42
de Jong	394.97-620.73 (kPa)	0.28

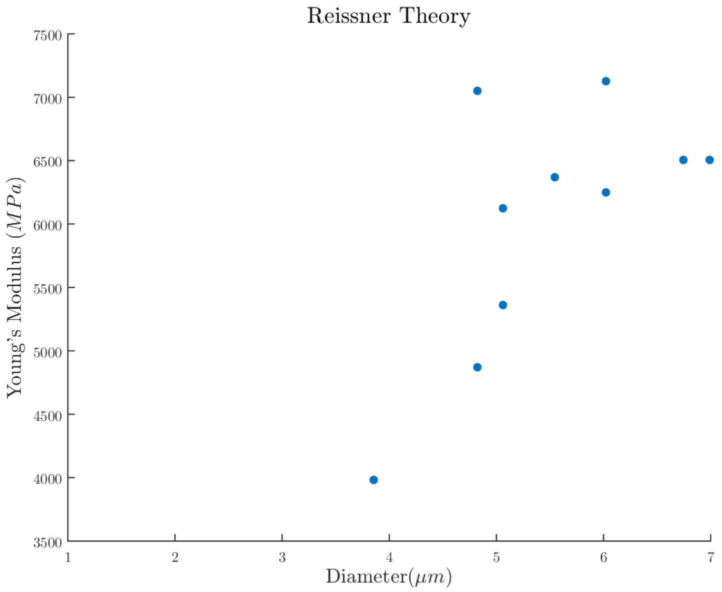
Reissner Theory
Young's Modulus (MPa)
7500
7000
6500
6000
5500
5000
4500
4000
3500
1
2
3
4
5
6
7
Diameter(μm)

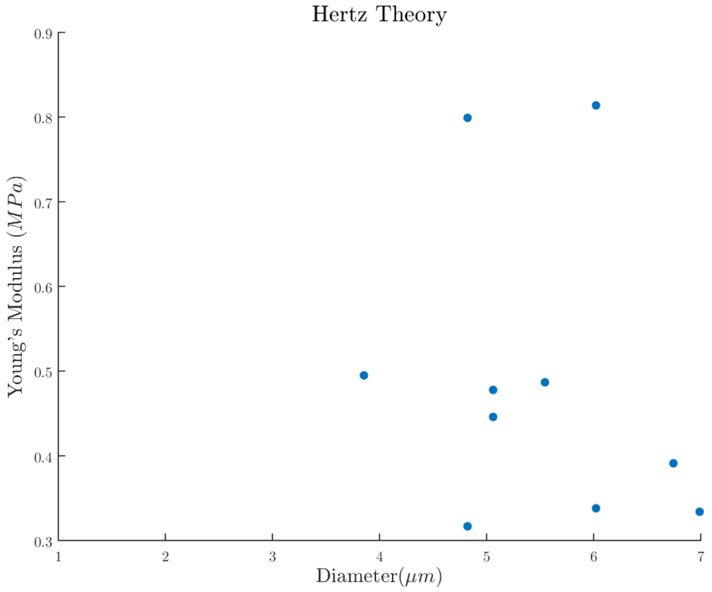
Hertz Theory
Young's Modulus (MPa)
0.9
0.8
0.7
0.6
0.5
0.4
0.3
1
2
3
4
5
6
7
Diameter(μm)

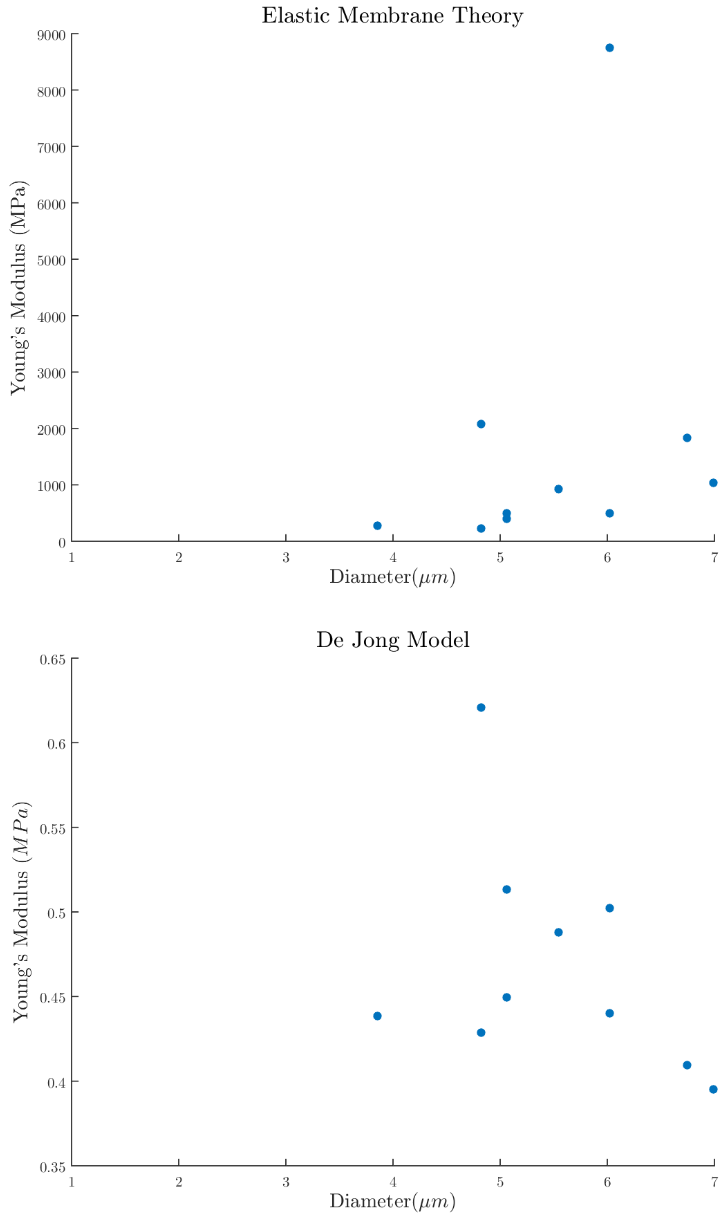

Figure 4.8: The Young's Modulus of SonoVue® day one, with peak force 40 nN for each microbubble plotted against its diameter using the four different models with spring constant $K_c = 0.4238$ N/m

Day two of investigating this batch provided more data samples and as illustrated in Figure 4.9 a linear relationship is now apparent for all models. Barring the elastic membrane theory, with the possible outlier, all models seem to provide consistent values with the first day of experiments as shown in Table 4.8.

Table 4.8: The theoretical models and their respective Young's Modulus and Pearson correlation p-values computed for SonoVue® day two.

] **Model**	**Young's Modulus**	**p-value**
Reissner	2.98-7.09 (GPa)	<0.001
Hertz	0.49-1.63 (MPa)	<0.001
Elastic membrane	135.53-2259.27 (MPa)	<0.001
de Jong	403.82-902.02 (kPa)	0.001584

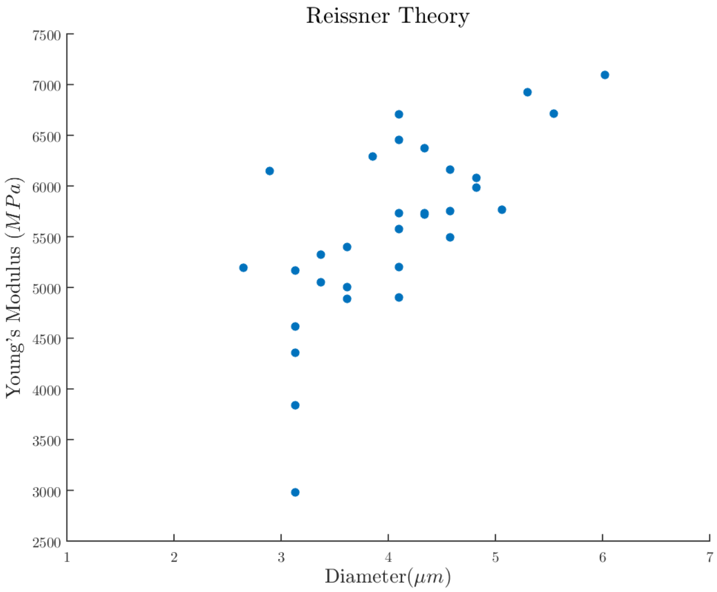
Reissner Theory
Young's Modulus (MPa)
7500
7000
6500
6000
5500
5000
4500
4000
3500
3000
2500
1
2
3
4
5
6
7
Diameter(μm)

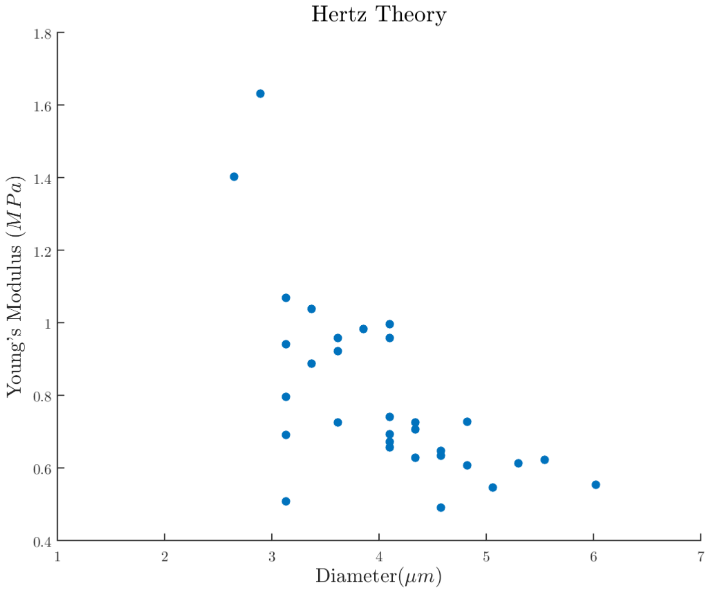
Hertz Theory
Young's Modulus (MPa)
1.8
1.6
1.4
1.2
1
0.8
0.6
0.4
1
2
3
4
5
6
7
Diameter(μm)

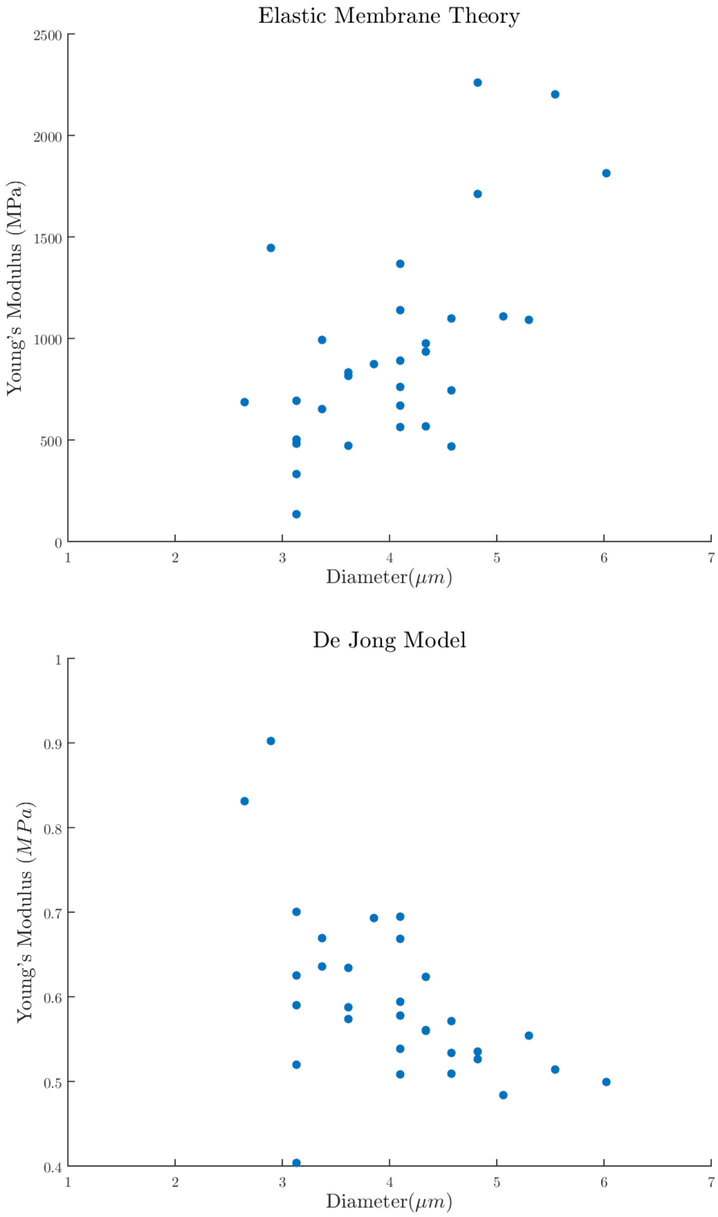

Figure 4.9: The Young's Modulus of SonoVue® day two, with peak force 40 nN for each microbubble plotted against its diameter using the four different models with spring constant $K_c = 0.4238$ N/m

The last experiment performed on SonoVue was performed with a stiffer cantilever as well as a significant increase in the maximal force applied to the microbubbles. The cantilever stiffness was chosen to be $K_c = 5.622 N/m$ and the peak force 400 nN. Contrary to the GB batches these changes drastically altered the Young's Modulus values for SonoVue with none of the models showing the previously attained linear relationship. This can be observed in figure 4.10 and table 4.9.

Table 4.9: The theoretical models and their respective Young's Modulus and Pearson correlation p-values computed for SonoVue with 400 nN peakforce.

Model	Young's Modulus	p-value
Reissner	4.53-21.58 (GPa)	0.35
Hertz	0.78-6.03 (MPa)	0.09
Elastic membrane	395.5-2496.5 (MPa)	0.35
de Jong	469.08-2923.74 (kPa)	0.28

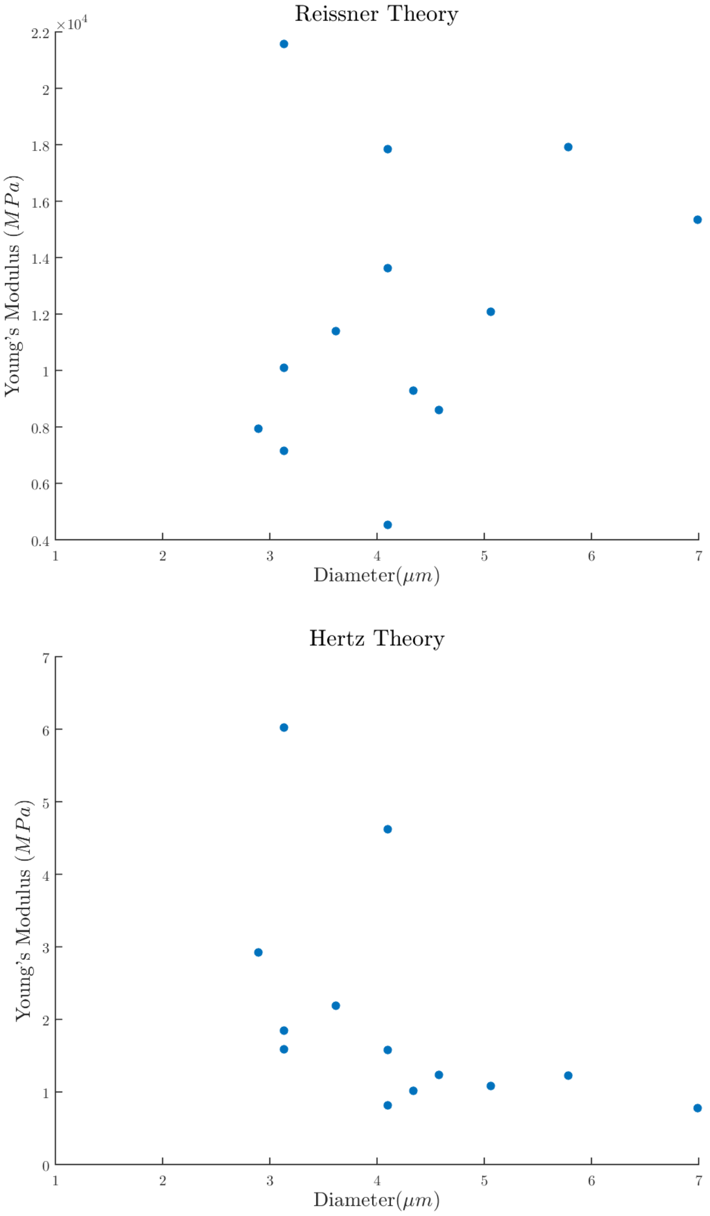
Reissner Theory
$\times 10^4$
2.2
2
1.8
1.6
1.4
1.2
1
0.8
0.6
0.4
Young's Modulus (MPa)
1
2
3
4
5
6
7
Diameter(μm)
Hertz Theory
7
6
5
4
3
2
1
0
Young's Modulus (MPa)
1
2
3
4
5
6
7
Diameter(μm)

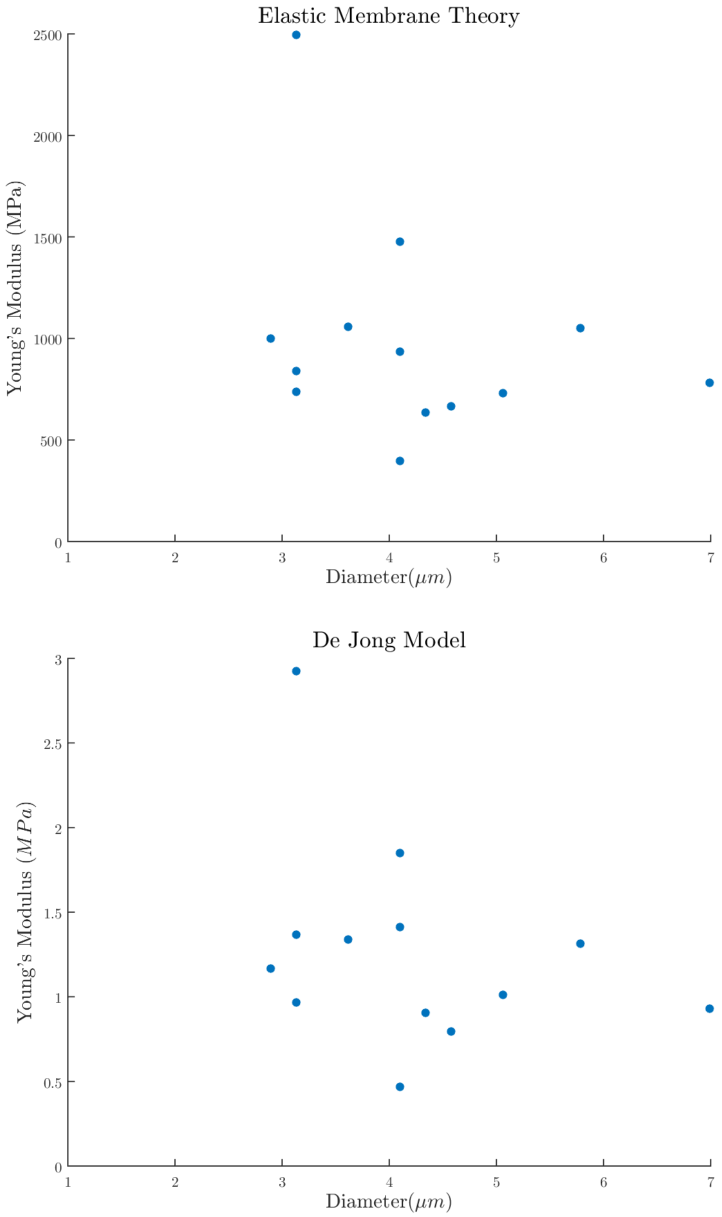

Figure 4.10: The Young's Modulus of SonoVue$^{®}$ with peak force 400 nN for each microbubble plotted against its diameter using the four different models with spring constant $K_c = 5.622$ N/m

4.2 Size Distributions

The following section is the size distributions obtained with the microbubbles. Unfortunately, the size distribution for the perfluoropropane batch analysed by attenuation could not be retrieved. The other four batches are given here, where GB 168 is air microbubbles produced with 1% nanoparticles and 1% casein, while GB 169 are identical, but with a perfluoropropane core. The microfluidic microbubbles come in two batches that differ in average size, but was produced by the same Tide® microfluidic system with a casein concentration of 0.5%.

Figure 4.11 shows the GB 168 air microbubbles that were produced by the ultra-turrax method and the reported mean size for this batch was $4.08\,\mu\mathrm{m}$.

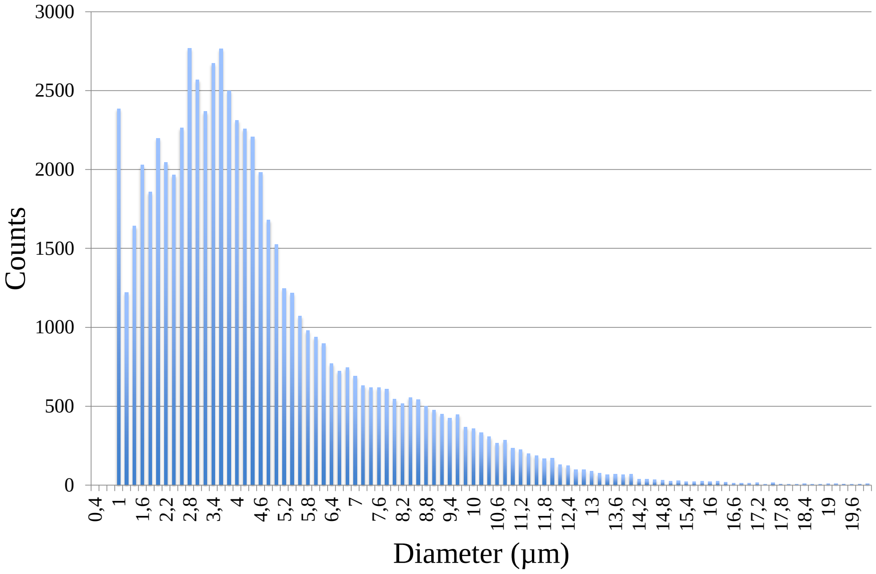

Figure 4.11: The size distribution of the GB 168 air microbubbles produced by SINTEF.

Produced in a similar fashion as the GB 168, Figure 4.12 shows the size distribution of GB 169. These perfluoropropane bubbles had a mean size of $3.92\,\mu\mathrm{m}$.

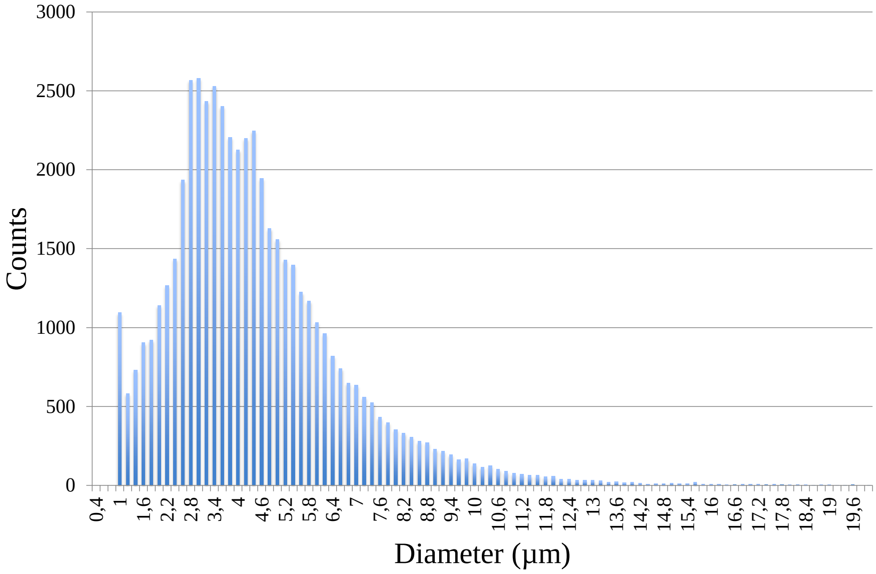

Figure 4.12: The size distribution of the GB 169 PFC microbubbles.

As Figure 4.13 shows, the size distribution of the microfluidic experiments are substantially narrower. The mean size of this batch was found to be $3.9\,\mu\mathrm{m}$.

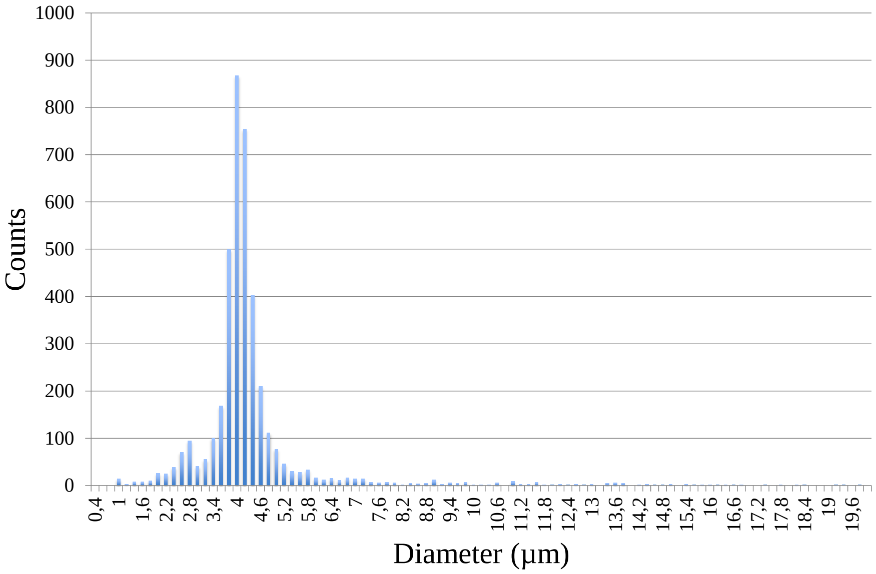

Figure 4.13: The size distribution of one of two batches of microfluidic air microbubbles.

The second microfluidic batch was produced with the aim of increasing the mean size, which Figure 4.14 shows was a success. Here the mean size is $5.43\,\mu\mathrm{m}$.

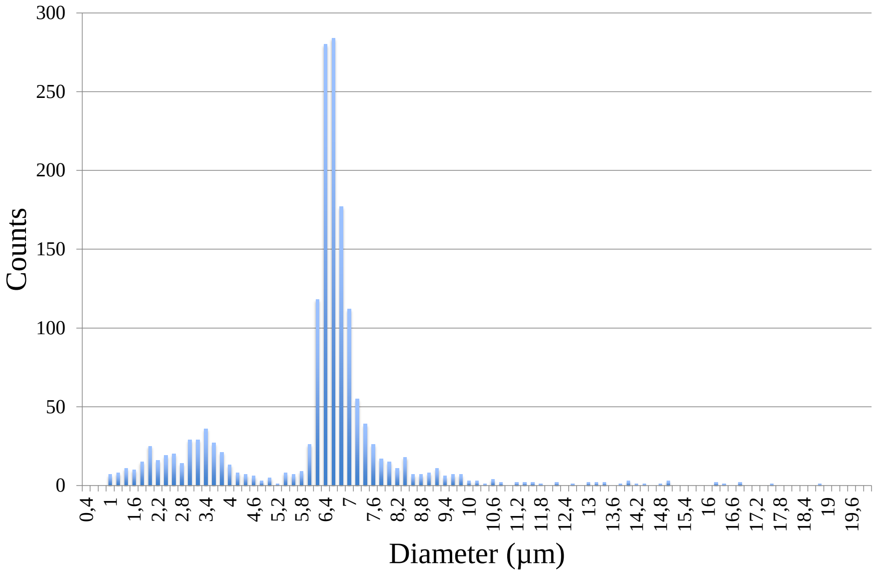

Figure 4.14: The size distribution of the second of two batches of microfluidic air microbubbles.

4.3 Backscatter Measurements

One part of the two pronged acoustic measurement procedure consisted of investigating the acoustic backscatter of the GB batches containing nanoparticles. The particular batch analysed was GB 169 and these microbbubles were produced in the same manner as the others, with 1% casein and 1% nanoparticles with a perfluoropropane core. Three transducer pairs at different transmit and receiving center frequencies were employed. In addition, the number of cycles was varied between two and twenty. Fresh microbubbles were added from the main container when the transducers were swapped. Note that the frequency spectre have not been corrected for transducer sensitivity.

4.3.1 1 MHz Transmitting Transducer With 5 MHz Receiving

Figure 4.15 shows the steady growth of the harmonics, from the single peak at 1 MHz at the initial MI. At this MI of 0.0250 the second harmonic can already be seen. The maximal amplitude of the harmonics seem to appear around a MI of 0.09. At a MI of 0.1760 a maximum number of peaks has been attained, with a newly formed subharmonic present below the fundamental. For the next pressure increments the harmonics seem to disappear, indicating destruction. The subharmonic, however, seems to grow for a period after ultraharmonic disappearance.

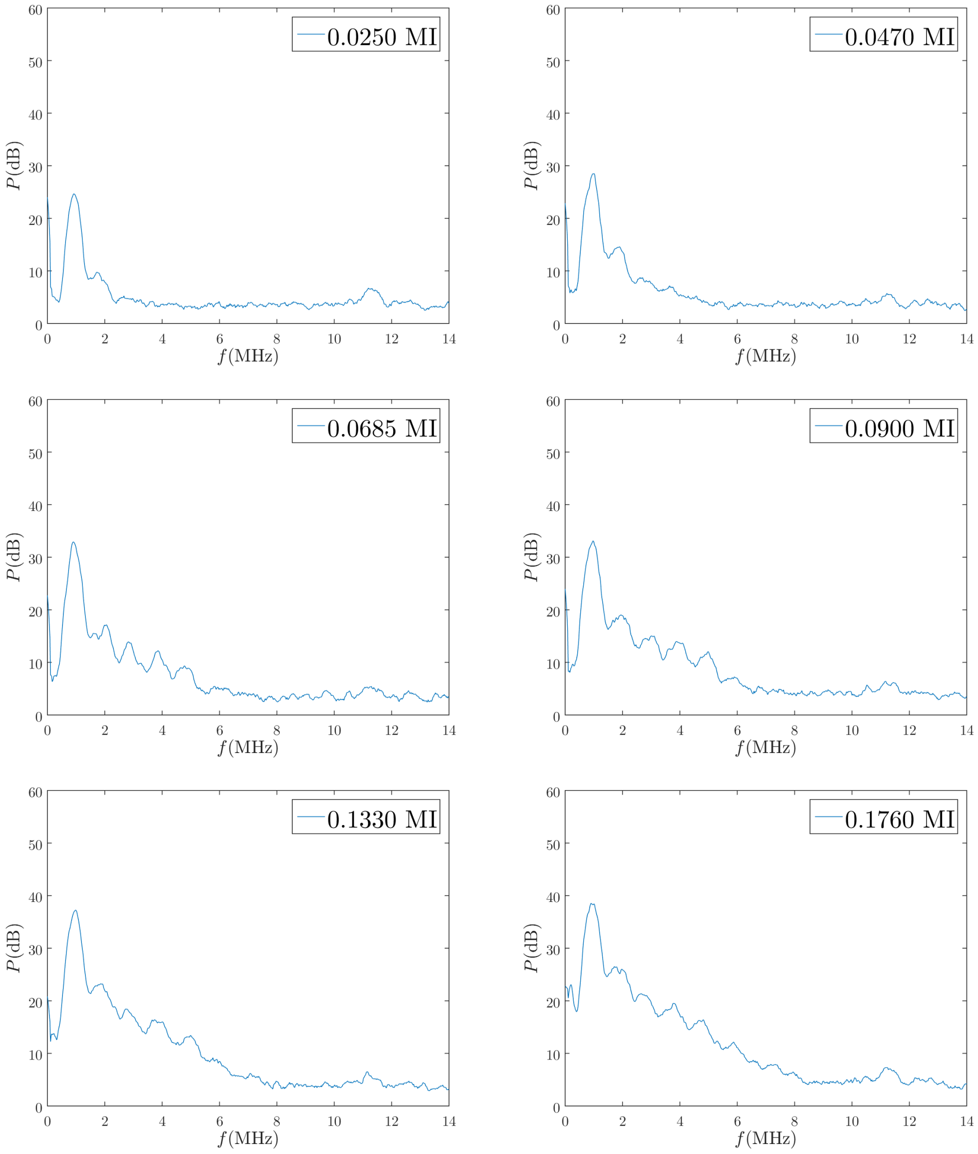
0.0250 MI
0.0470 MI
0.0685 MI
0.0900 MI
0.1330 MI
0.1760 MI
P(dB)
f(MHz)
0
10
20
30
40
50
60
0
2
4
6
8
10
12
14

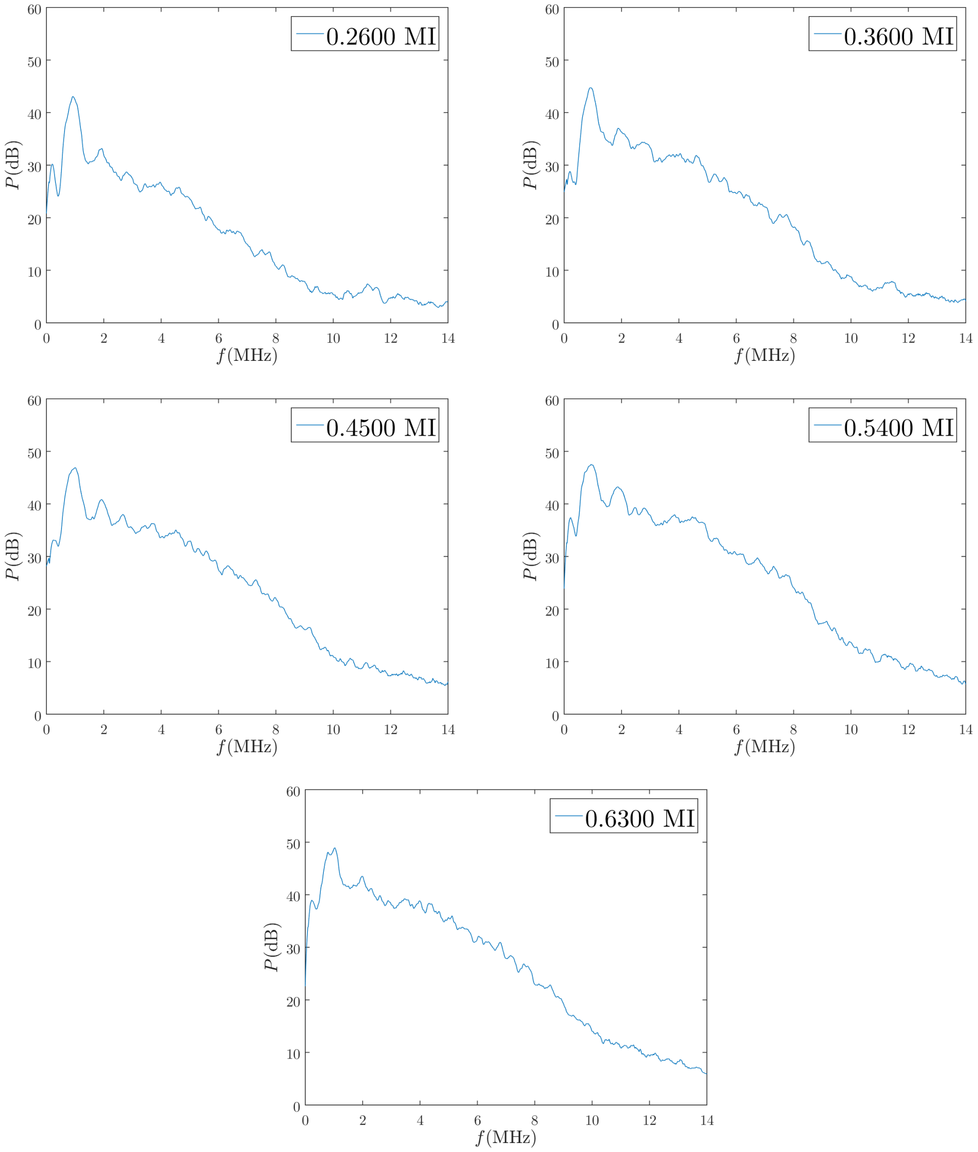

Figure 4.15: Backscatter measurements for increasing MI with the power in decibel as a function of frequency for a transmitting transducer with center frequency 1 MHz. The receiving transducers center frequency is 5 MHz and the number of cycles is two.

With the increasing number of cycles the peaks are more readily defined and clearly observable as shown in Figure 4.16. Five peaks, of which four are harmonics above the fundamental, can be observed for the first series at MI 0.025. Further increase of pressure also increases the number of harmonics up to a MI of 0.1760 where the ultraharmonics come online. The sprouting of ultraharmonics is best perceived around 7.5 MHz, although they are also present at lower and higher frequencies. The subharmonic at half the fundamental also arises at the pressure increment of 0.1760. The ultraharmonics continue to grow through the pressure increase at a MI of 0.26 and 0.36. In the following Figures the ultraharmonics dissipate with increasing pressure. At the maximal pressure, with an associated MI of 0.63 the harmonics above 7 MHz seem to have disappeared extensively .

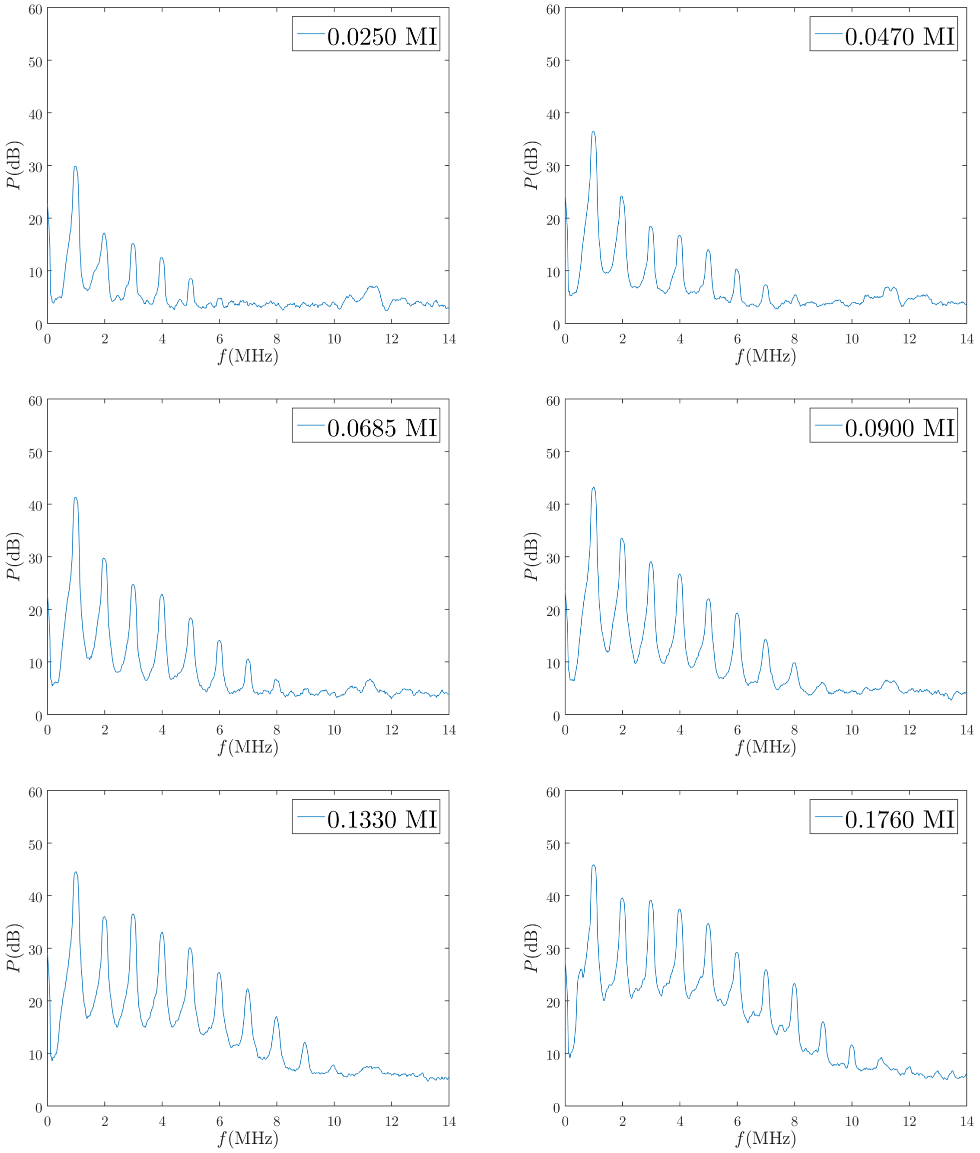

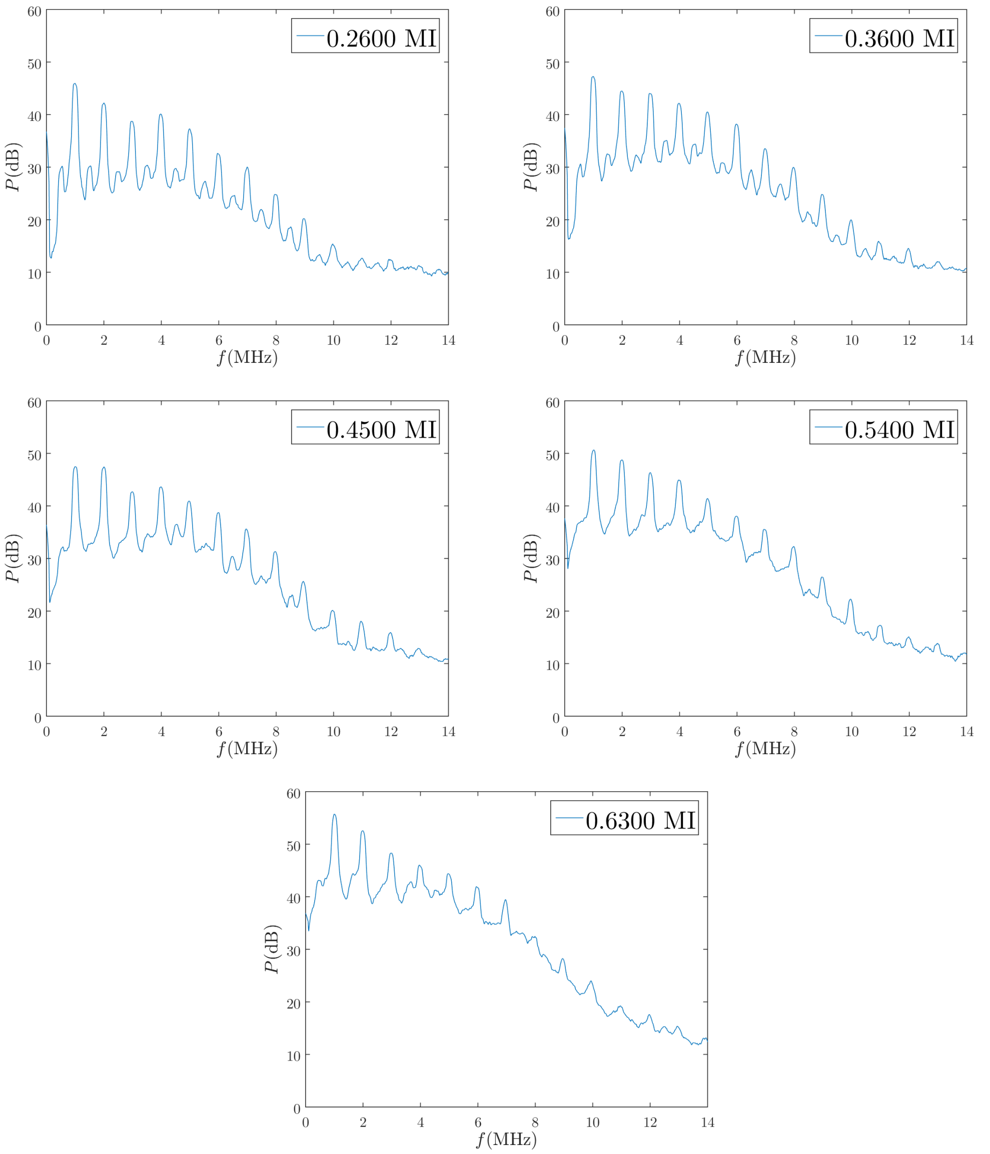

Figure 4.16: Backscatter measurements for increasing MI with the power in decibel as a function of frequency for a transmitting transducer with center frequency 1 Mhz. The receiving transducers center frequency is 5 MHz and the number of cycles is 20.

4.3.2 3.5 MHz Transmitting Transducer With 5 MHz Receiving

Apart from the growth of the fundamental, the first additional feature of Figure 4.17 appears at a mechanical index of 0.056 to 0.1050 with the subharmonic at 1.75 MHz. The additional peak seen rising from MI 0.39 to 0.53 may indicate the ultraharmonic at 5.25 MHz, the peak is, however, not very pronounced.

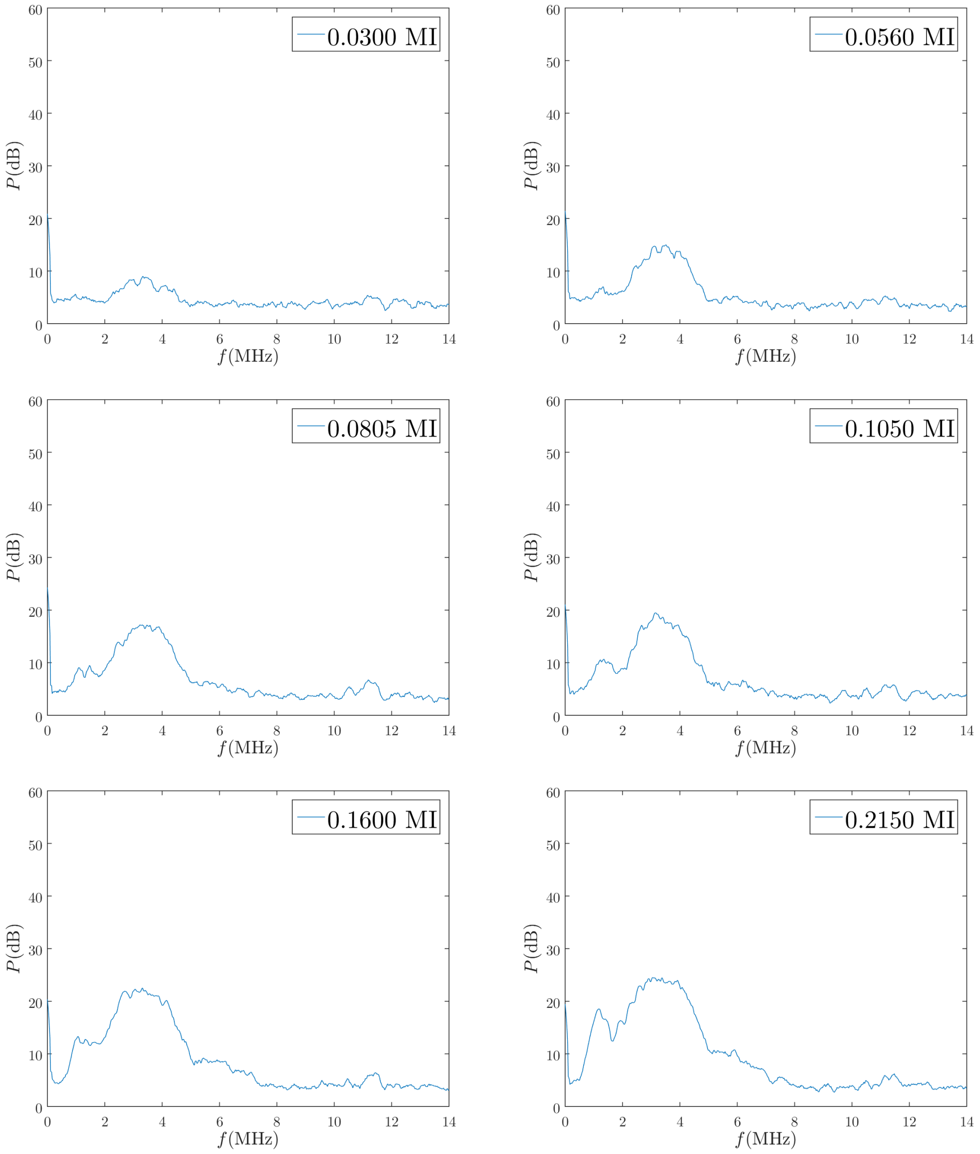

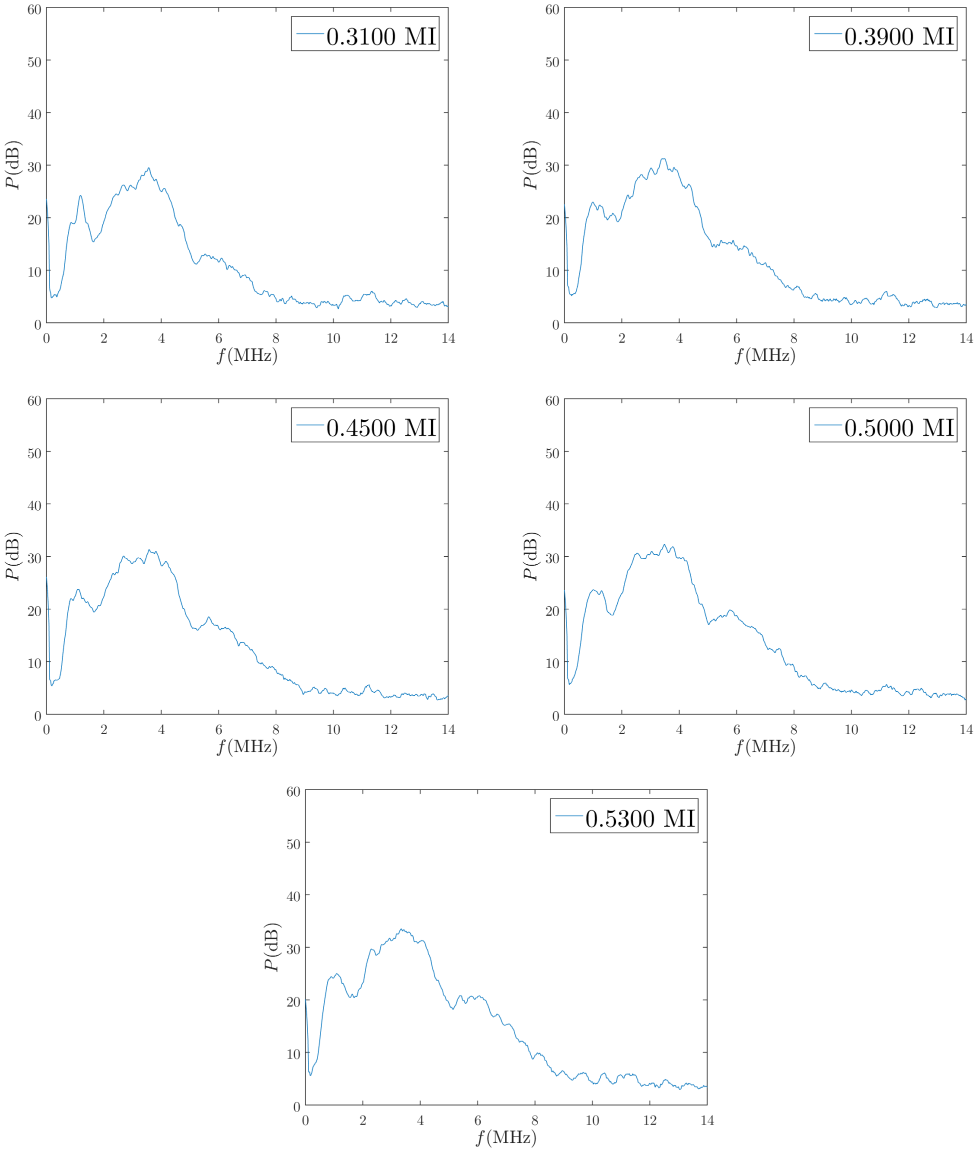

Figure 4.17: Backscatter measurements for increasing MI with the power in decibel as a function of frequency for a transmitting transducer with center frequency 3.5 MHz. The receiving transducers center frequency is 5 MHz and the number of cycles is two.

Increasing the cycles to twenty for the 3.5 MHz transmitting transducer leaves the initial MI plot in Figure 4.18 with three peaks. They correspond to the first harmonic at 7 MHz and the first subharmonic at 1.75 MHz. The next subfigure, at MI 0.056, the frist ultraharmonic begins to take shape, at 5.25 MHz. These four peaks persist as a quartet until MI 0.16 where the second subharmonic is generated at approximately 1.17 MHz. At MI's above 0.39 the signal can be seen to return the third harmonic as well as the second ultraharmonic at 10.5 MHz and 8.75 MHz, respectively.

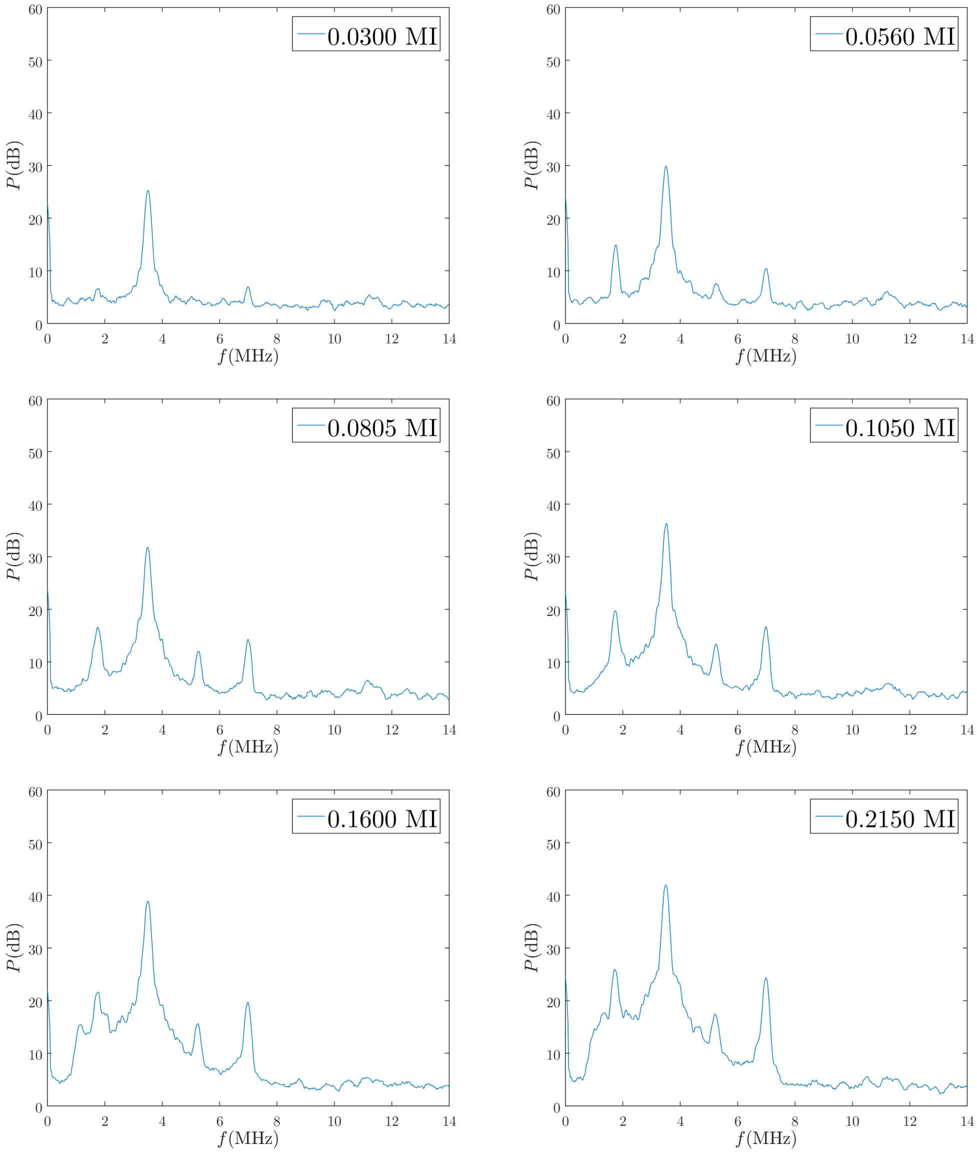

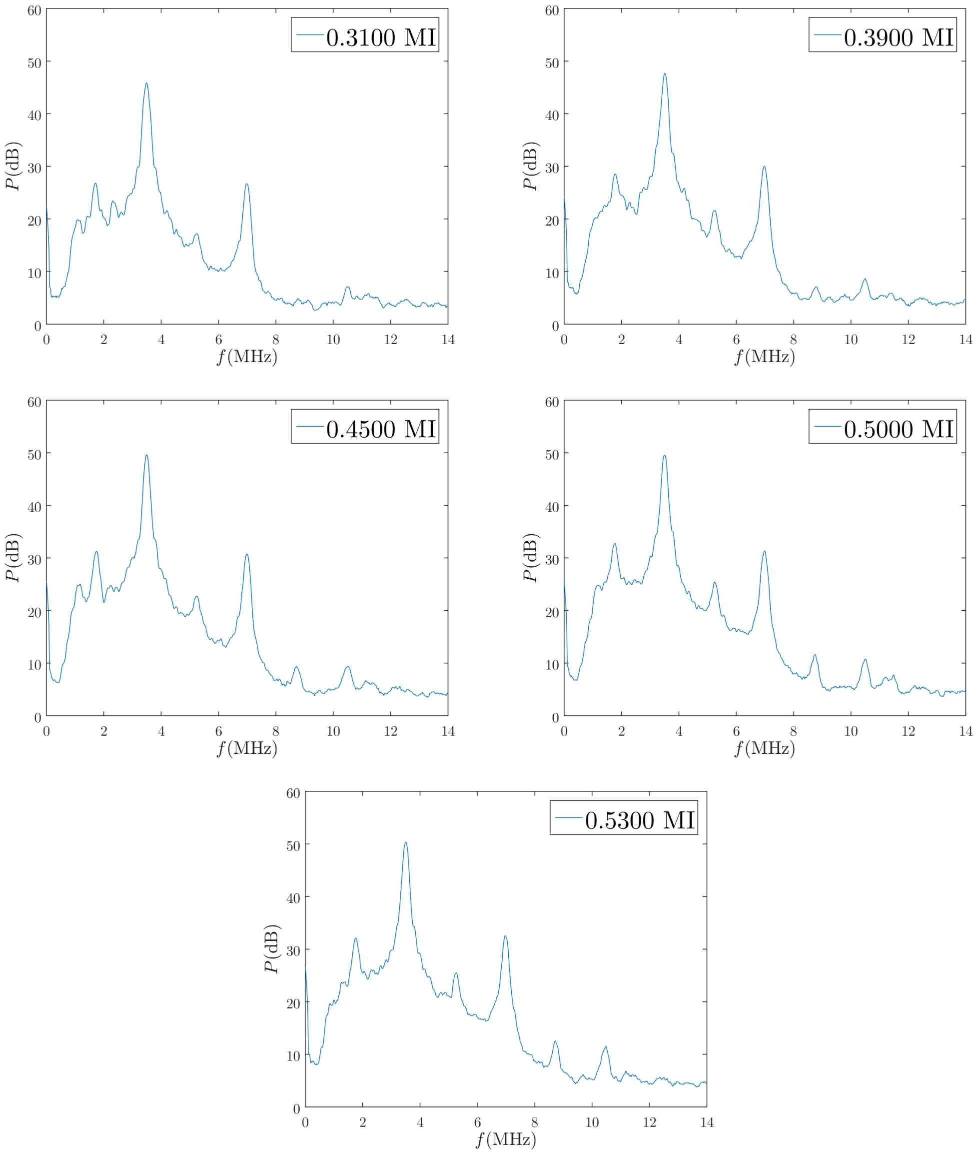

Figure 4.18: Backscatter measurements for increasing MI with the power in decibel as a function of frequency for a transmitting transducer with center frequency 3.5 Mhz. The receiving transducers center frequency is 5 MHz and the number of cycles is 20.

4.3.3 5 MHz Transmitting Transducer With 10 MHz Receiving

The final transducer pair that was used produced the results shown in Figure 4.19. For this transducer pair there is no apparent peak at the first measurement, the fundamental appears at MI 0.09, barely above the noise level. At 0.33 MI there seems to be the addition of a second peak at approximately 2 MHz, this does not however correspond to a subharmonic of the fundamental itself. The first harmonic at two times the fundamental can be seen from a MI of 0.47 and onwards at 10 MHz. The peak development in general for this number of cycles with this transducer pair appears to be low.

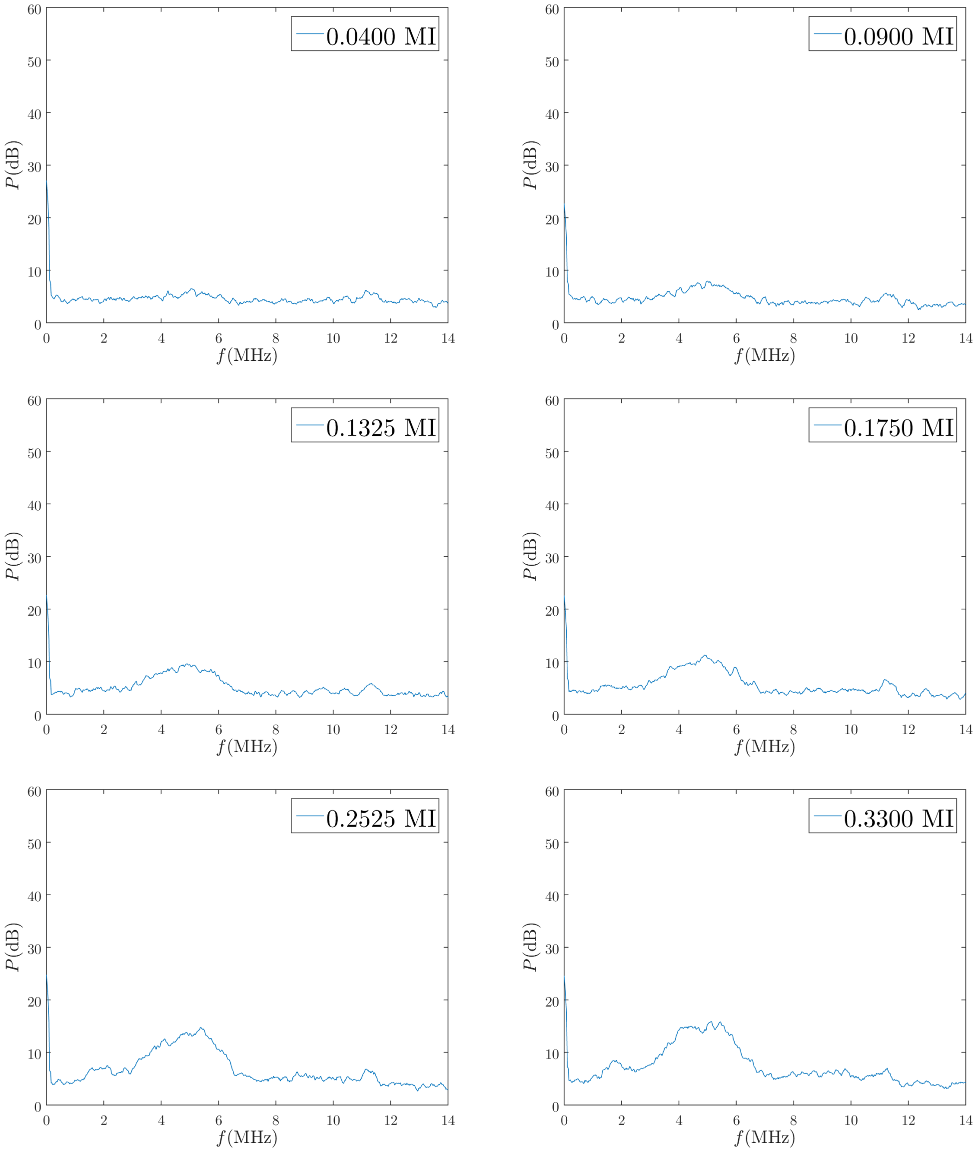
0.0400 MI
0.0900 MI
0.1325 MI
0.1750 MI
0.2525 MI
0.3300 MI
P(dB)
f(MHz)
0
10
20
30
40
50
60
0
2
4
6
8
10
12
14

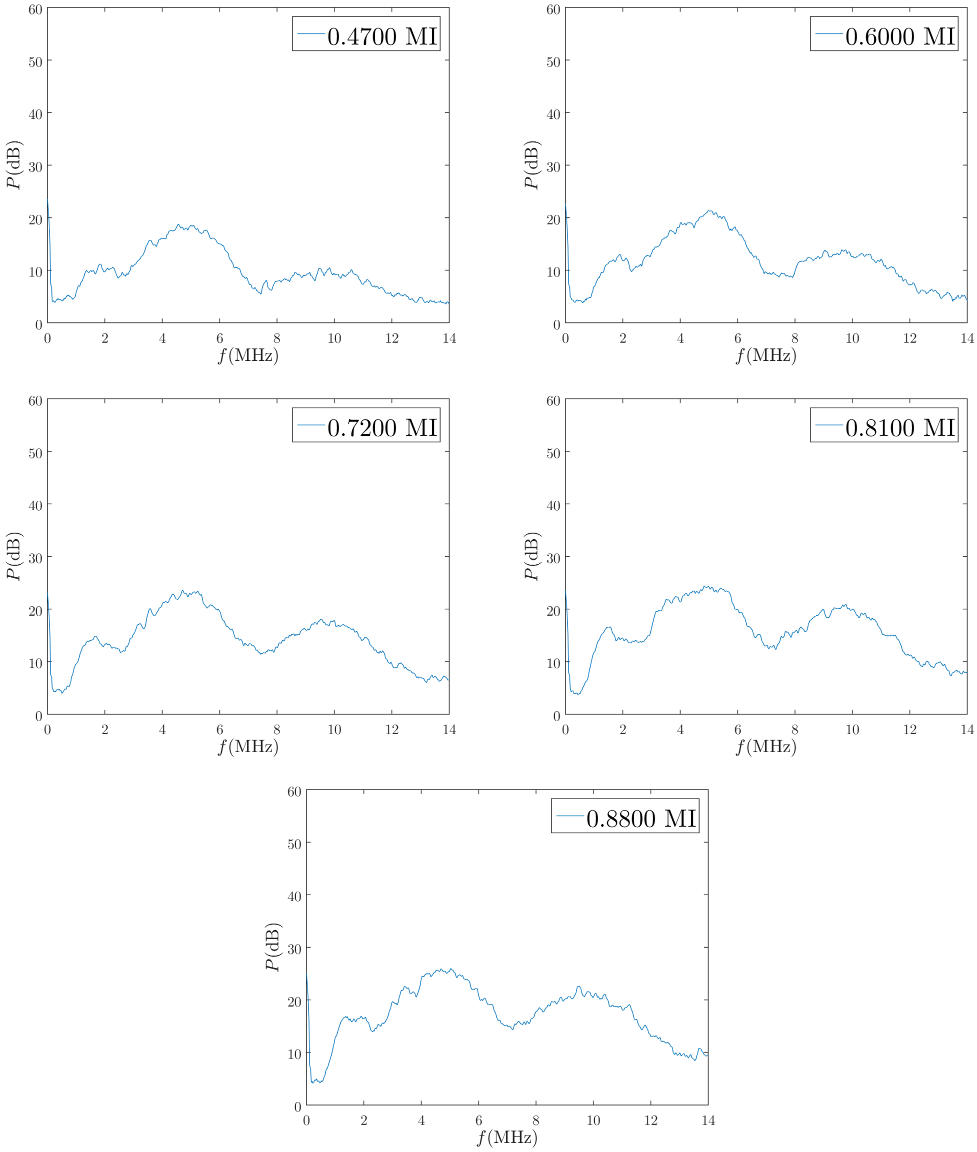

Figure 4.19: Backscatter measurements for increasing MI with the power in decibel as a function of frequency for a transmitting transducer with center frequency 5 Mhz. The receiving transducers center frequency is 10 MHz and the number of cycles is two.

After the increase to 20 cycles Figure 4.20 readily shows the first harmonic at 10 MHz, as well as the predicted subharmonic at 2.5 MHz. At MI 0.9 the first ultraharmonic at 7.5 MHz is barely visible. For the next pressure increments this ultraharmonic disappears, not re-emerging before a mechanical index of 0.33 is reached. Following a growth series the second ultraharmonic appears at MI 0.47.

Revisiting this ultraharmonic at a MI 0.72 reveals that it has all but vanished. At MI 0.81 it is no longer visible.

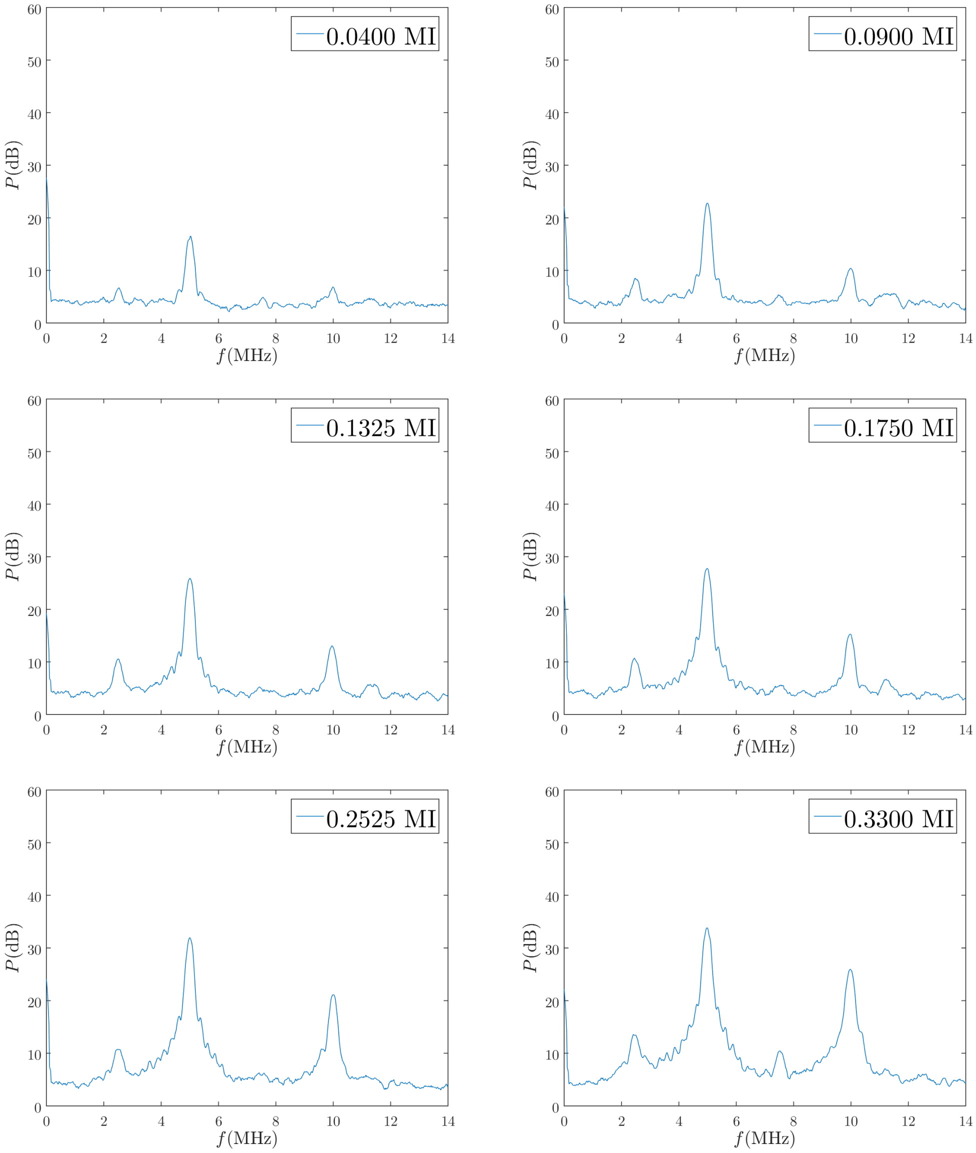

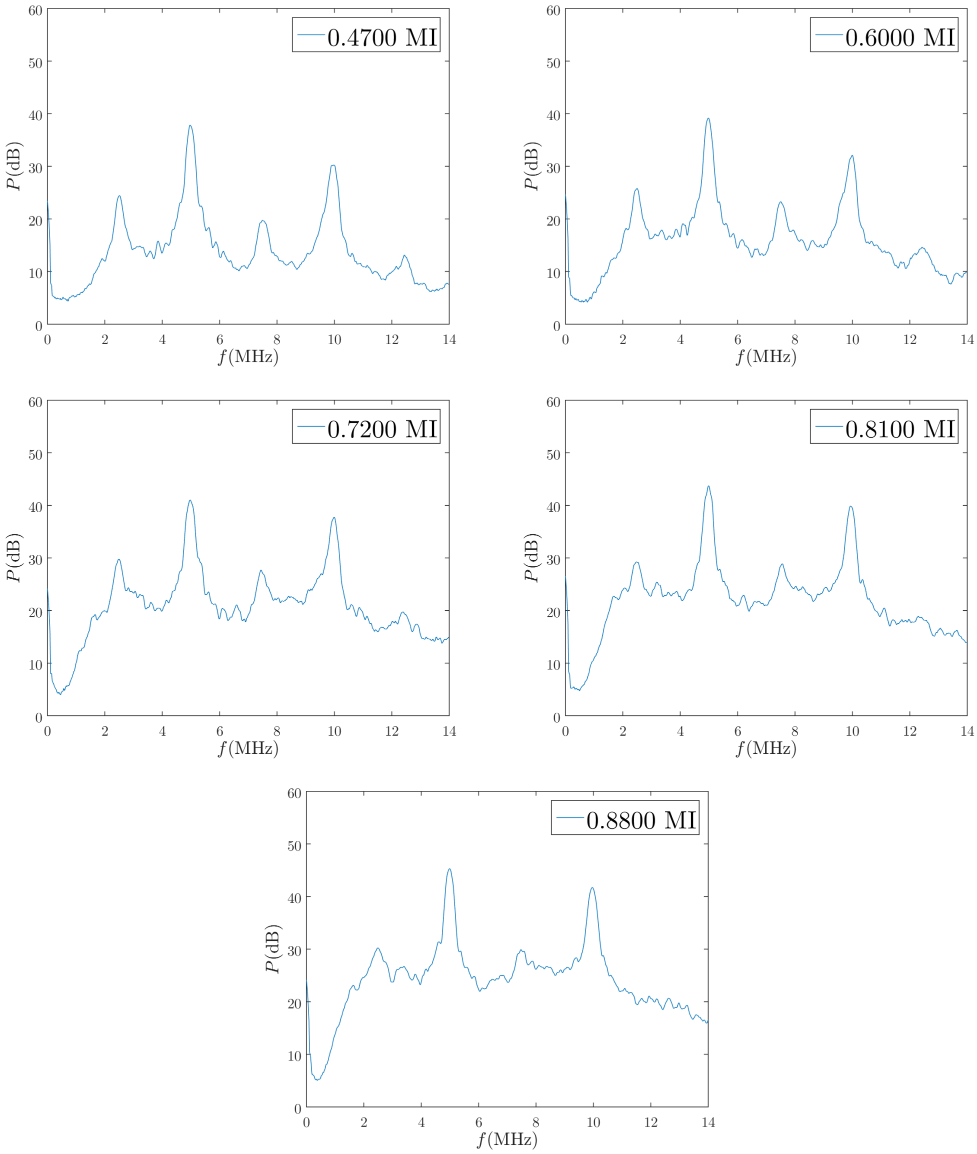

Figure 4.20: Backscatter measurements for increasing MI with the power in decibel as a function of frequency for a transmitting transducer with center frequency 5 Mhz. The receiving transducers center frequency is 10 MHz and the number of cycles is 20.

4.4 Attenuation Measurements

Following the successful automation of the acoustic setup it was possible to perform measurements series for the attenuation with better temporal resolution and so investigate the attenuation development over time. The experiments were conducted on a usual GB nanoparticle/PFC batch. In addition microbubbles with a different gas core, air, was produced, albeit the same in all other respects. Following the test of a microfluidic setup, microbubbles produced in this manner was also subjected to attenuation analysis.

4.4.1 PFC Microbubbles

Figure 4.21 shows three representative graphs showing the shape of the attenuation curve for a GB batch. The spectrum appears wide and so attenuates at approximately the same level over all frequencies, except in the lower end, where there is a drop-off. A peak is visible, however, at approximately 3-4 MHz.

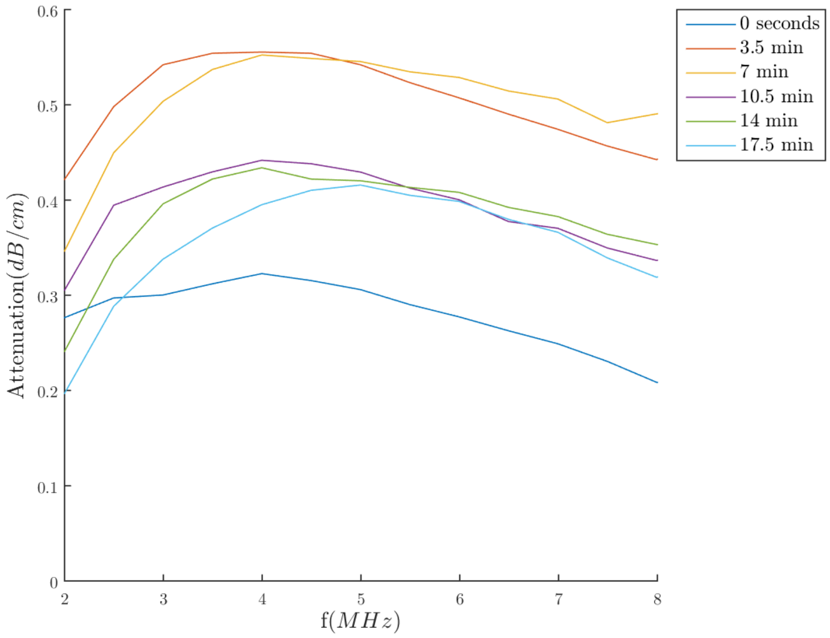

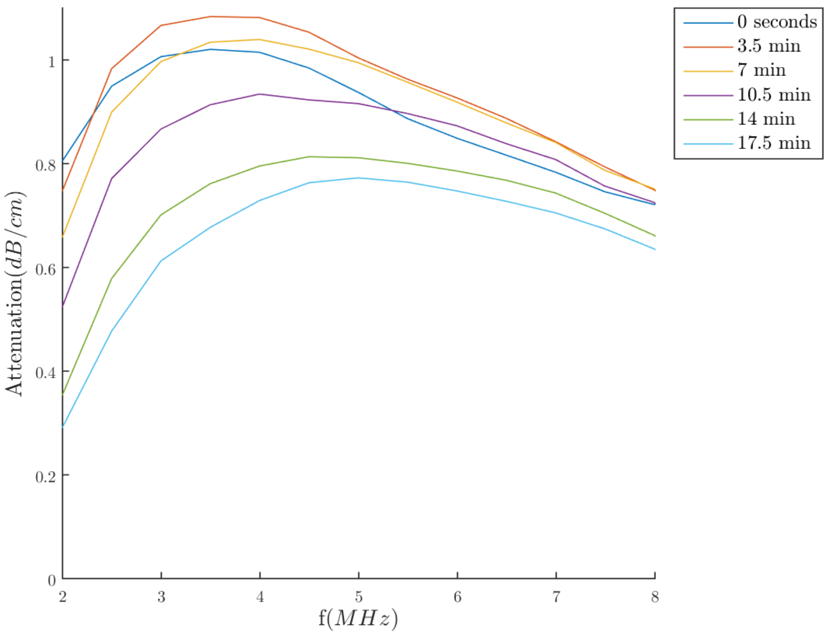

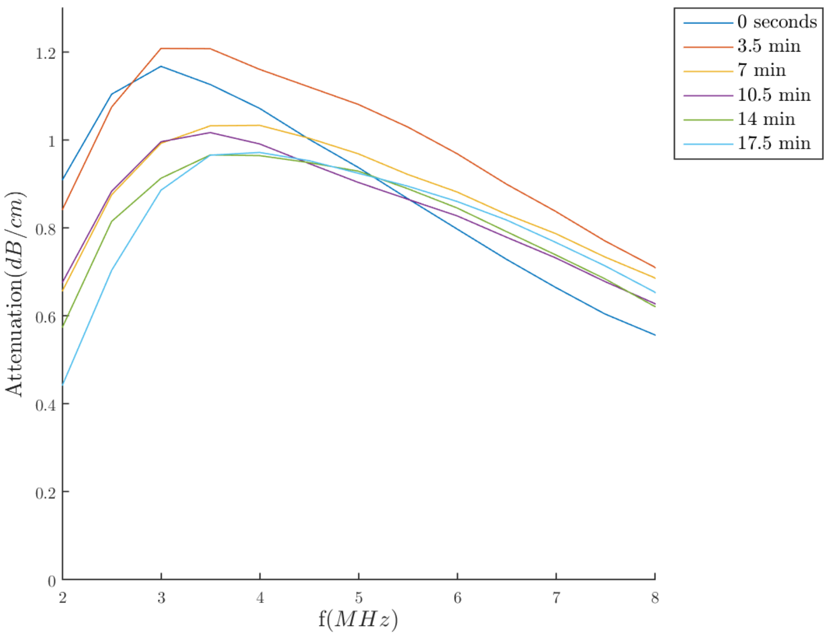

Figure 4.21: Attenuation over the full spectrum over time for the three first measurement series of the GB PFC batch. The number of microbubbles is 10 million/50 ml

The data presented in Figure 4.22 confirms the lower attenuation at 2 MHz compared to higher frequencies, which show a tighter distribution. The two top graphs display a growth period in the first two minutes followed by a gradual signal loss. In addition to being lower from the start the 2 MHz attenuation appears to be affected by a steeper decline.

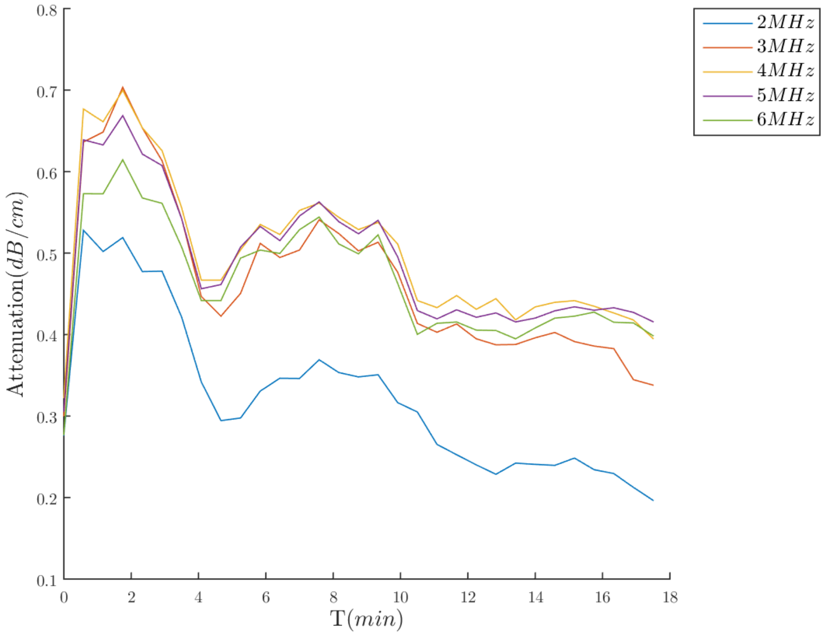

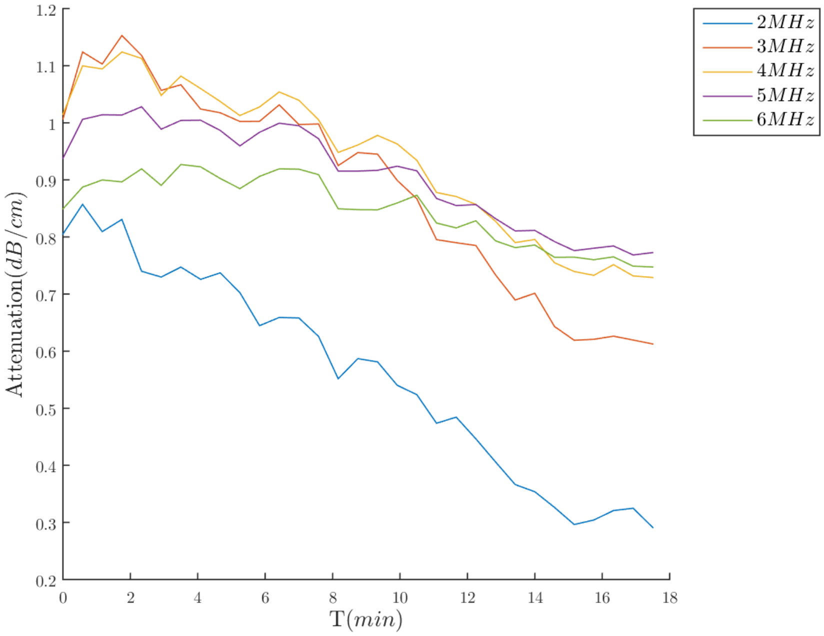

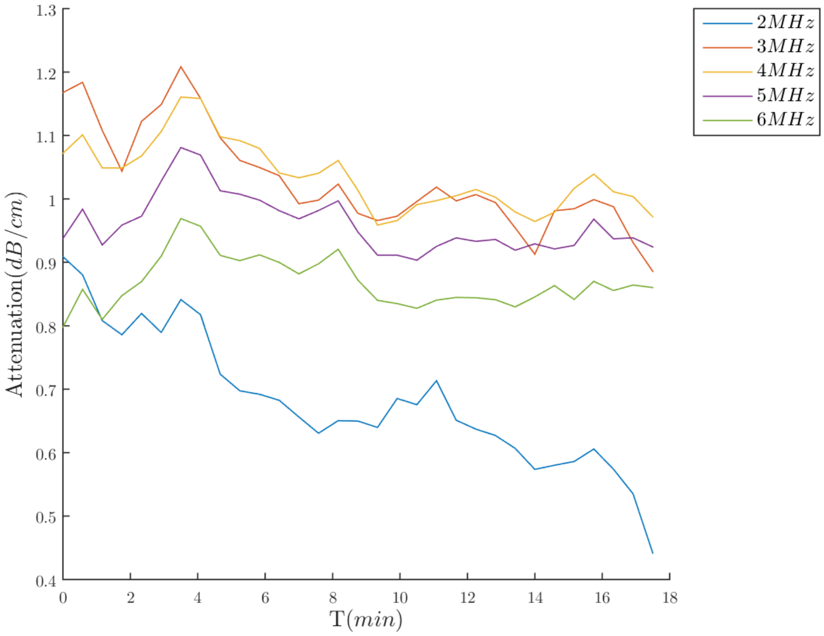

Figure 4.22: Time development of attenuation at specific frequencies for the three first measurement series of the GB PFC batch. The number of bubbles is 10 million/50ml.

Figure 4.23 illustrates that the growth and following signal loss is not only restricted to the individual measurement series. Following the development of the attenuation at 5 MHz at seven minutes the same development can be observed. Measurements that were performed with a fresh batch produced an attenuation of approximately 0.6 dB/cm for 5 MHz at minute seven. This does, however, not stay constant. One hour later the attenuation has increased to above 1 dB/cm before a rapid decline ensues. The second part of the graph are measurements performed the following day with off-hours being the blank gap between day one and two. Each data point corresponds to a 18 minute series, where the attenuation is probed at the seventh minute. While the result renders averaging across all the measurement series futile it cements how the sample will degrade in the canister, even if only opened for short amounts of time.

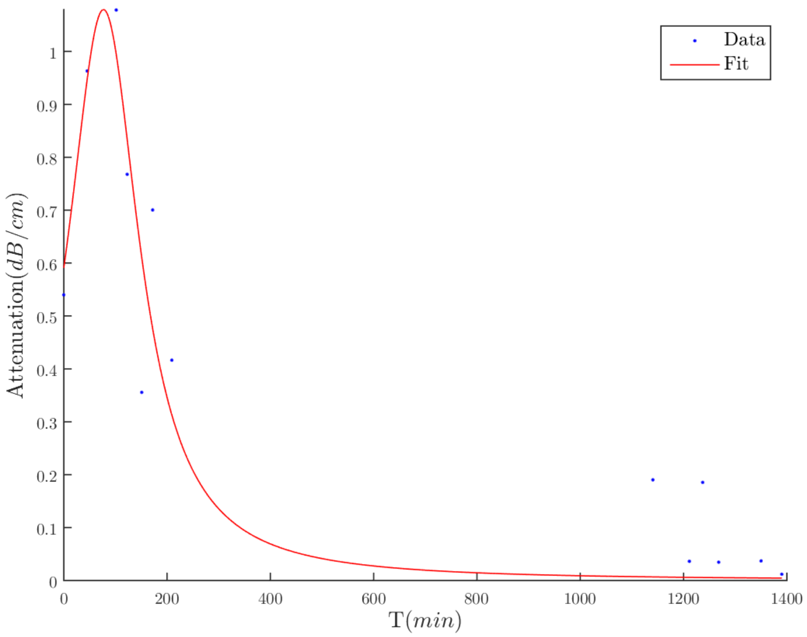

Figure 4.23: The attenuation at aproximate resonance frequency, 3.5 MHz, at minute seven for all measurement series of the GB PFC batch. The number of bubbles is 10 million/50ml.

Using the Epstein-Plesset model to predict the dissolution of a perfluoropropane bubble, Figure 4.24 was produced. The values for the other variables in the modified Epstein-Plesset equation were: $H = 5.2 \cdot 10^{-4}$, $P_a = 10^5$ Pa, the coefficient of diffusivity of perfluropropane in water $d_w = 7.45 \cdot 10^{-10}$ m^2/s and a surface tension $\sigma = 0.025$ N/m. Saturation was set to $f = 4/6$. These values were adapted from Sarkar [38]. The aim was to illustrate the setup ability to estimate the resistance of the shell to gas diffusion. Assuming that gas diffusion is the governing factor in attenuation loss a minimum shell resistance can be obtained by reasoning that the MBs are attenuating past their predicted dissolution. The shell resistance employed was taken to be 10^5 s/m and the dissolution was calculated from an approximate mean of the GB batches. Using more advanced models it is also possible to account for the growth period in the initial part of the graph. This also entails an increase in complexity however.

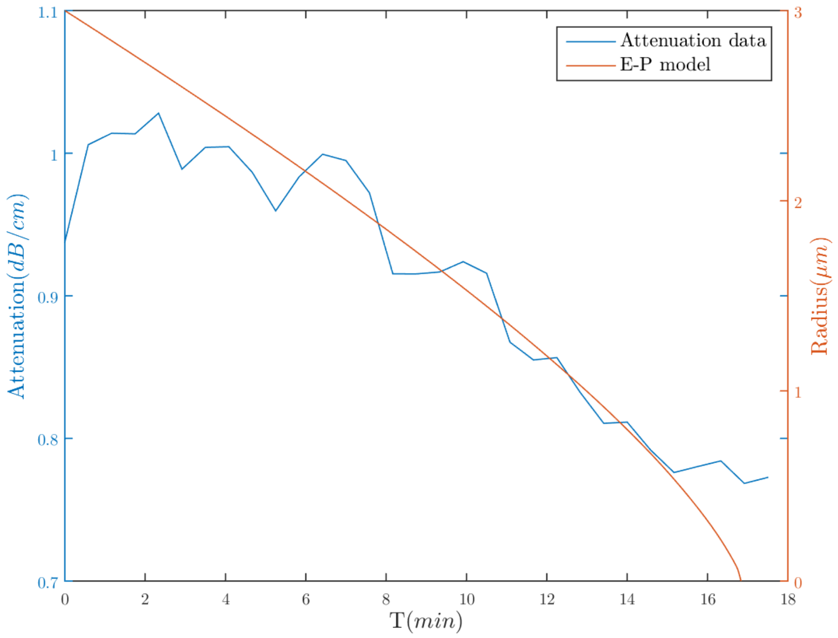

Figure 4.24: The attenuation development at 5 MHz of the PFC batch with the predicted dissolution of a batch mean radius microbubble according to 2.45. The data is taken from the first measurement series.

4.4.2 GB 168 Air

Due to an unfortunate leak in the PFC tank the microfluidic batches could not be produced with this gas core as was initially the plan. The content of the microfluidic batch was therefore air instead and in order to compare the production methods a set of air bubbles was produced according to the GB batches, although as stated with an air core.

The GB 168 batch with one million microbubbles produces significantly lower attenuation values. There also appears to be a varying shape to the spectra. In the first graph the resonance frequency appears to be at approximately 4 MHz, however, the two following plots present higher attenuation values for higher frequencies.

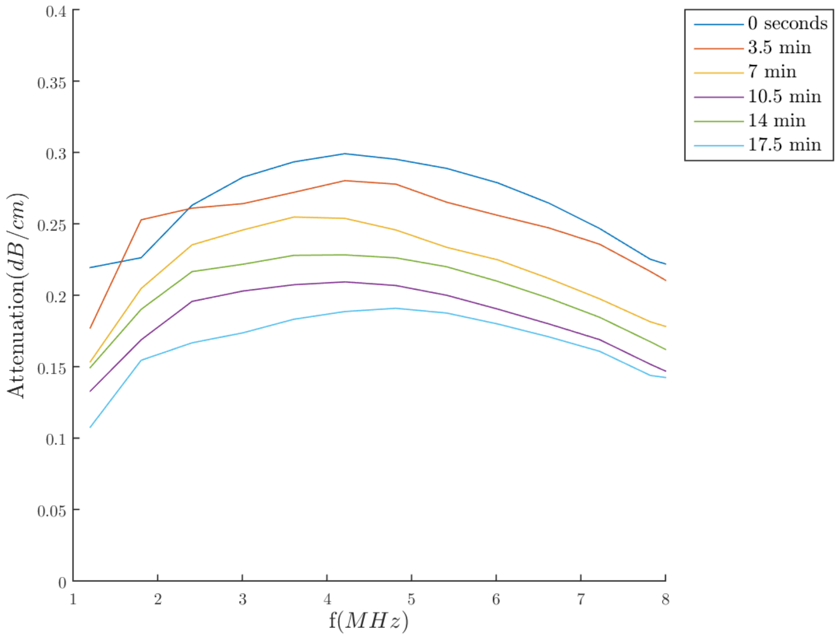

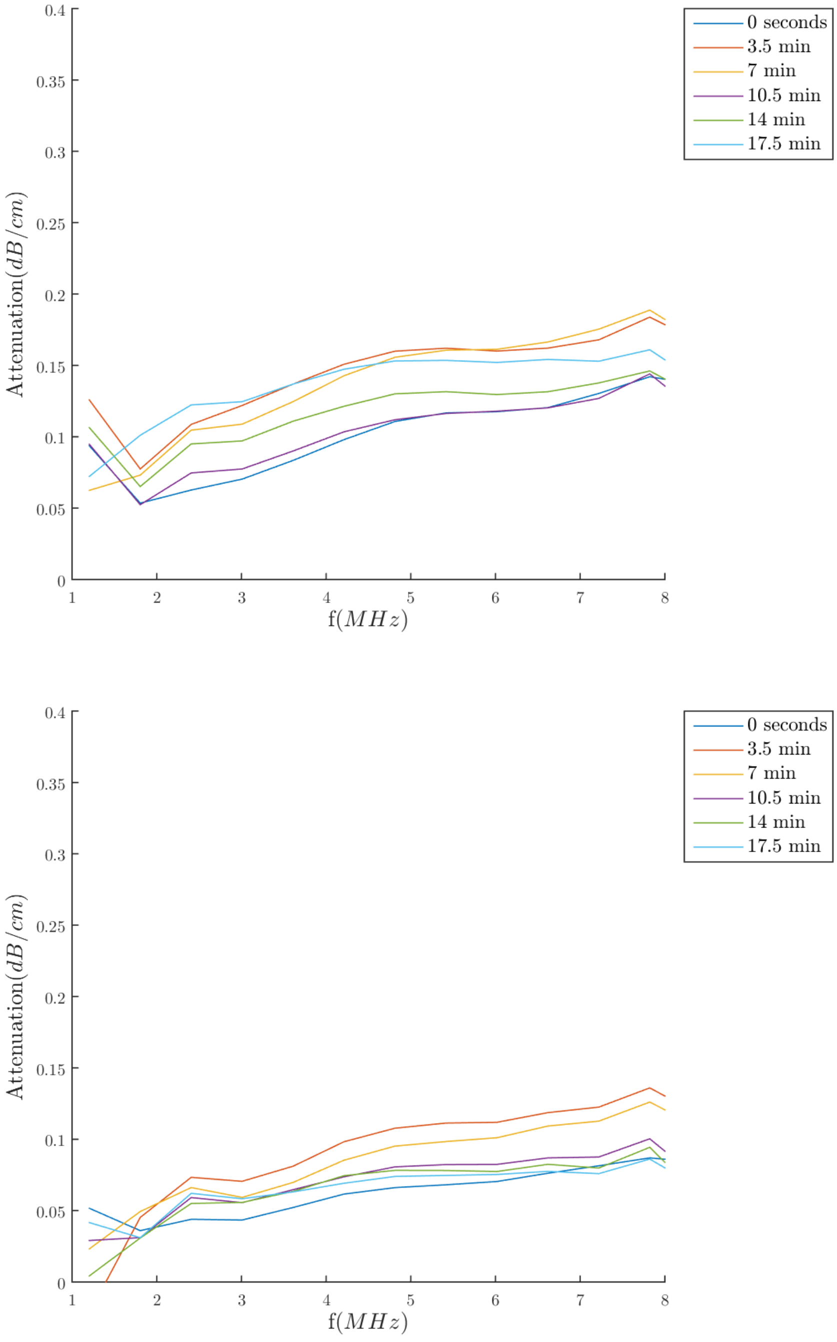

Figure 4.25: Attenuation over the full spectrum over time for the three first measurement series of the GB 168 air batch, the concentration is 1 million/50 ml.

The previously seen growth period and gradual loss is not reproduced in the GB 168 batch as seen in Figure 4.26. Frequency specific attenuation seems to vary greatly, with a tendency to oscillate. All the frequencies appear to behave in a similar fashion.

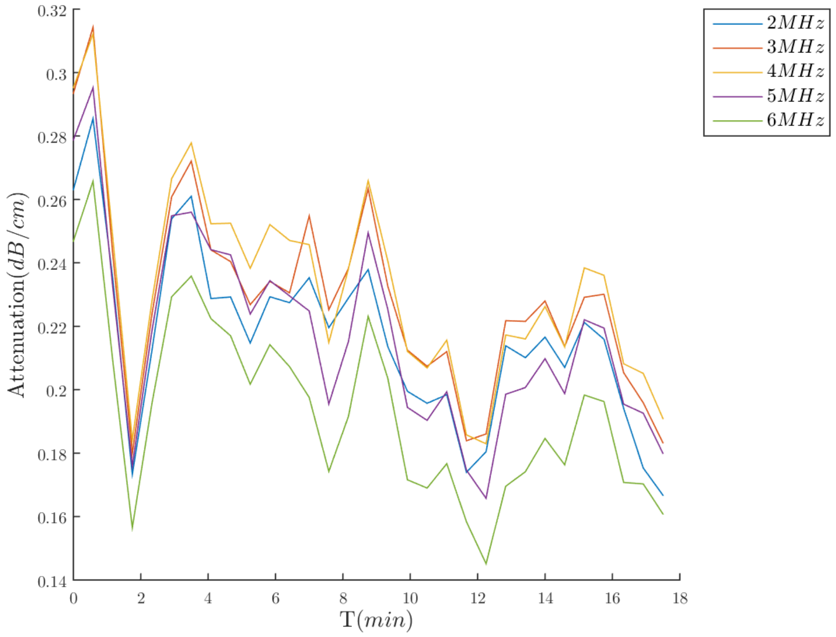

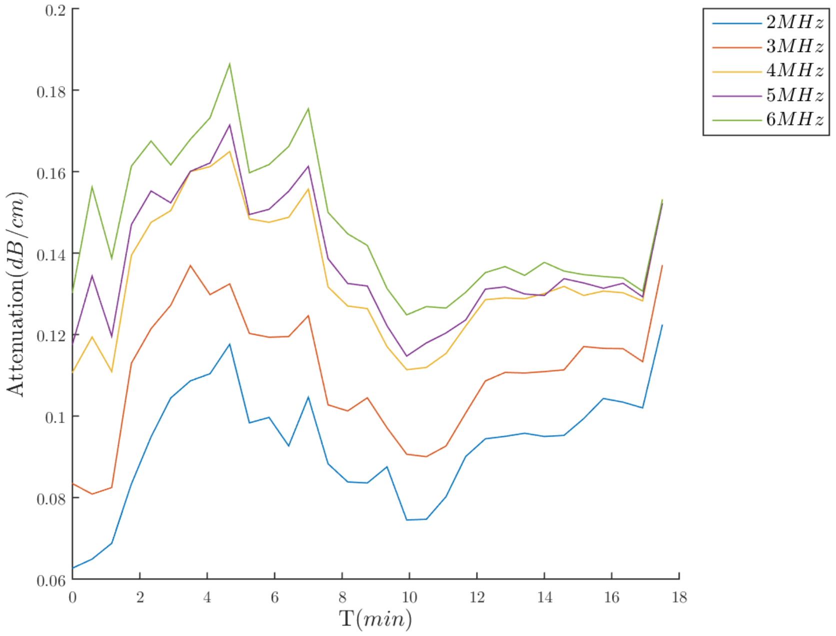

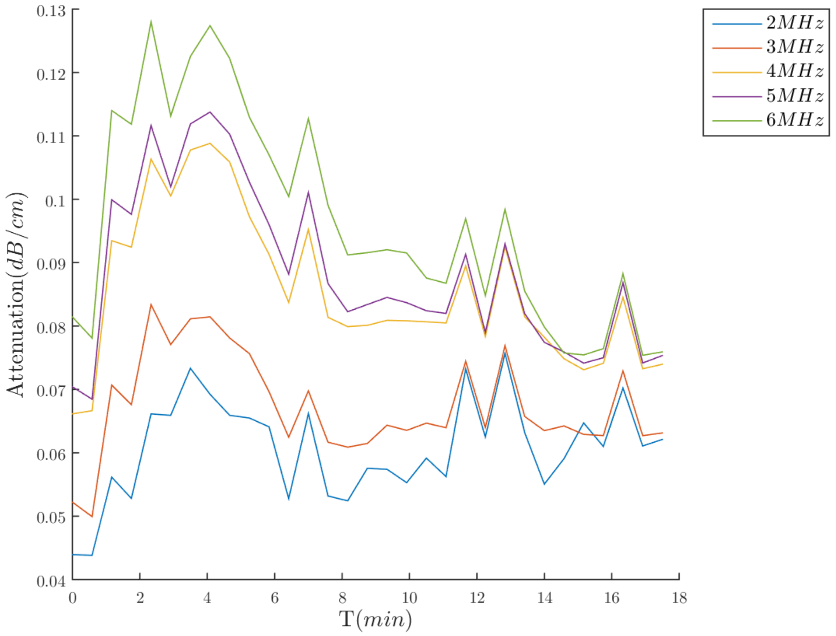

Figure 4.26: Time development of attenuation at specific frequencies for the three first measurement series of the GB 168 air batch. The number of bubbles is 1 million/50ml.

Figure 4.27 supports the great variations seen in 4.26, there is no clear development at the determined resonance frequency over all the measurement series, a total period of around 250 minutes.

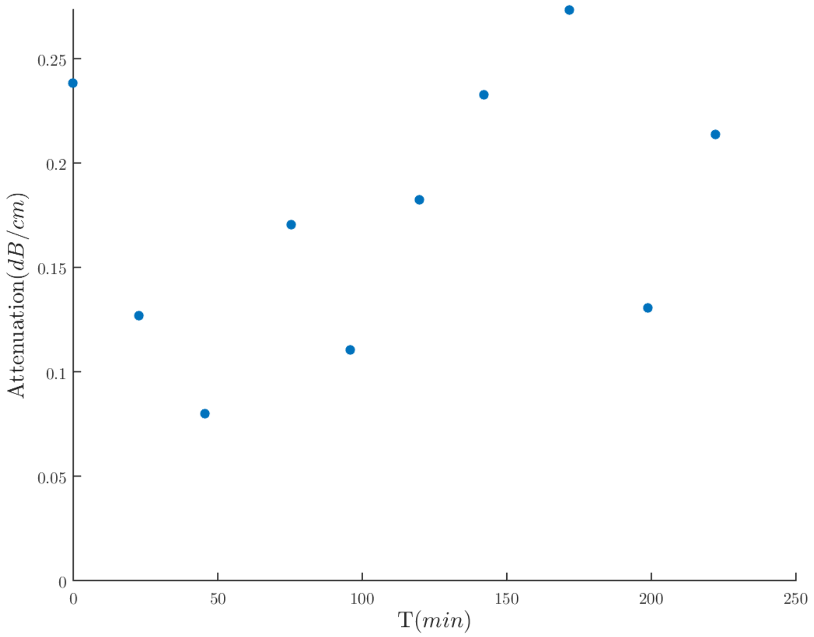

Figure 4.27: The attenuation at aproximate resonance frequency, 4 MHz, at minute seven for all measurement series of the Gb 168 air batch. The number of bubbles is 1 million/50ml.

The experiments with 10 million microbubbles in the chamber were performed after the previously described 1 million/50 ml measurements. Figure 4.28 shows an attenuation over the frequency spectrum similar to those obtained with 1 million microbubbles, but with elevated values.

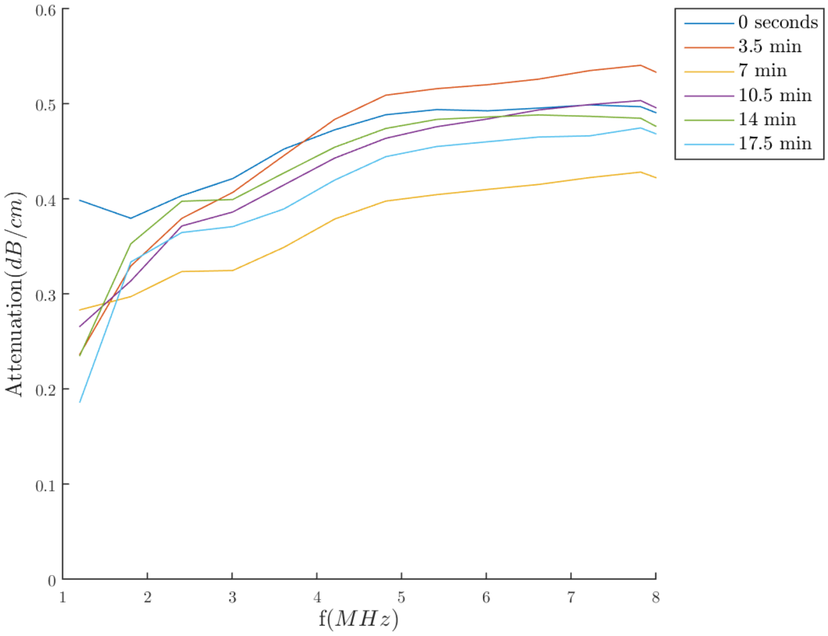

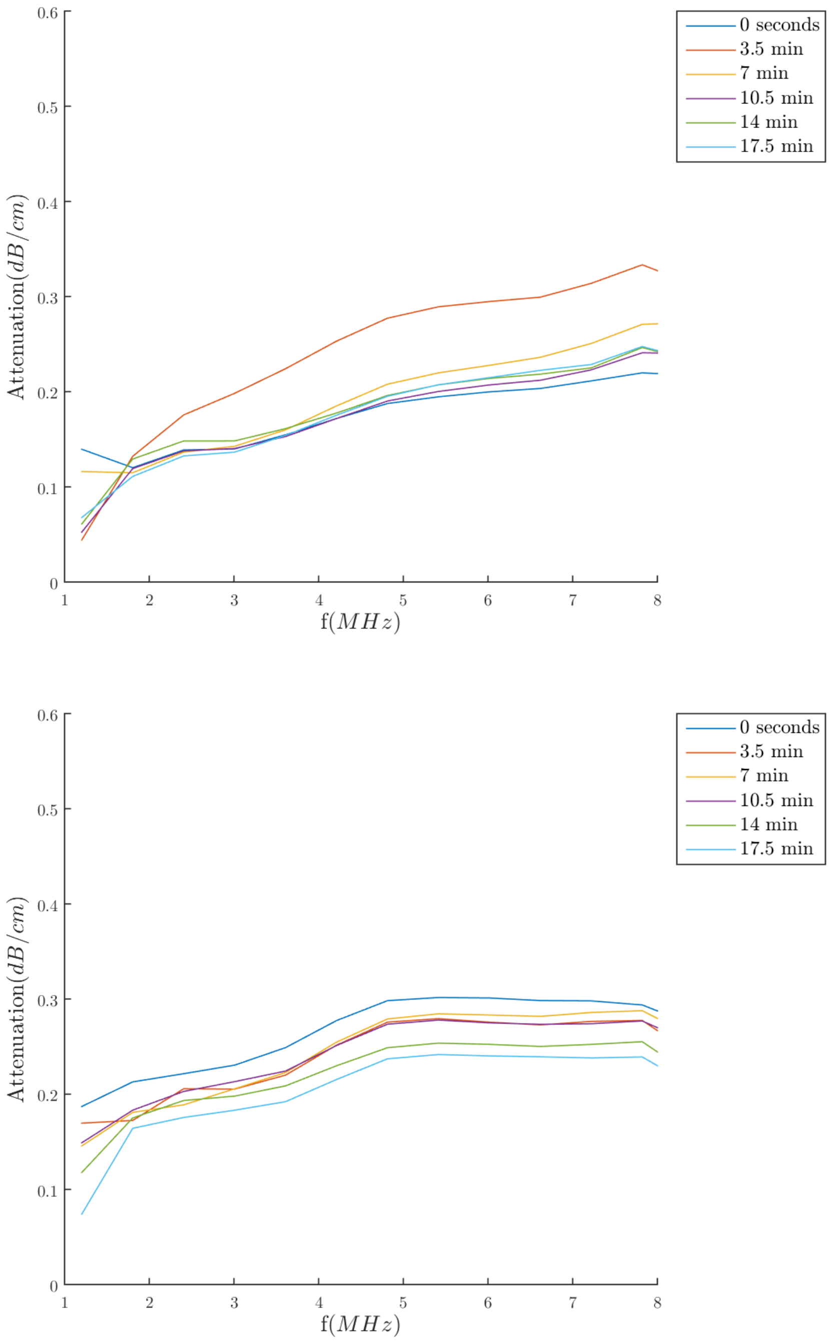

Figure 4.28: Attenuation over the full spectrum over time for the three first measurement series of the GB 168 air batch. The number of microbubbles is 10 million/50ml.

Inspecting select frequencies over representative series only the last graph shows a clear declining trend, as shown in Figure 4.29. The oscillating theme from the 1 million/50 ml series seem to be recurring and there appears to be no specific frequencies that behave in non conformal.

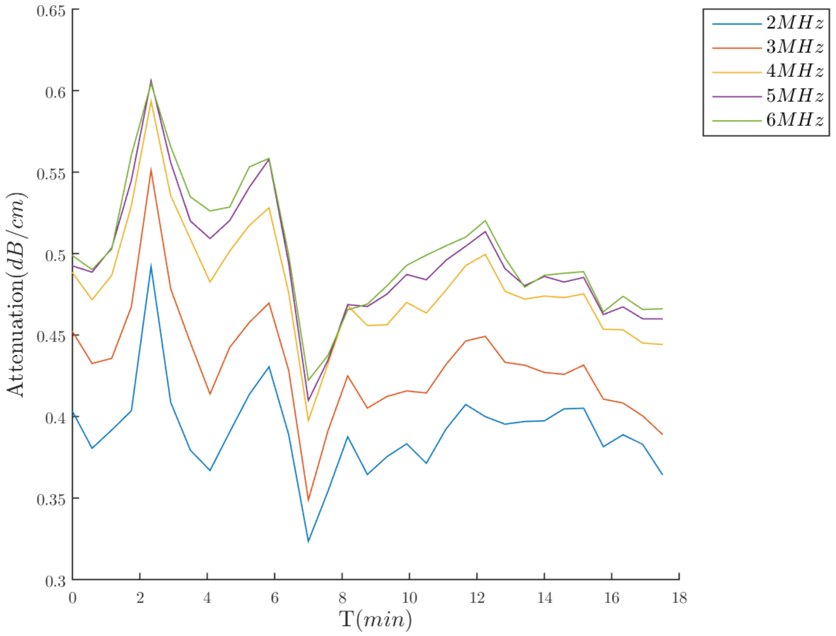

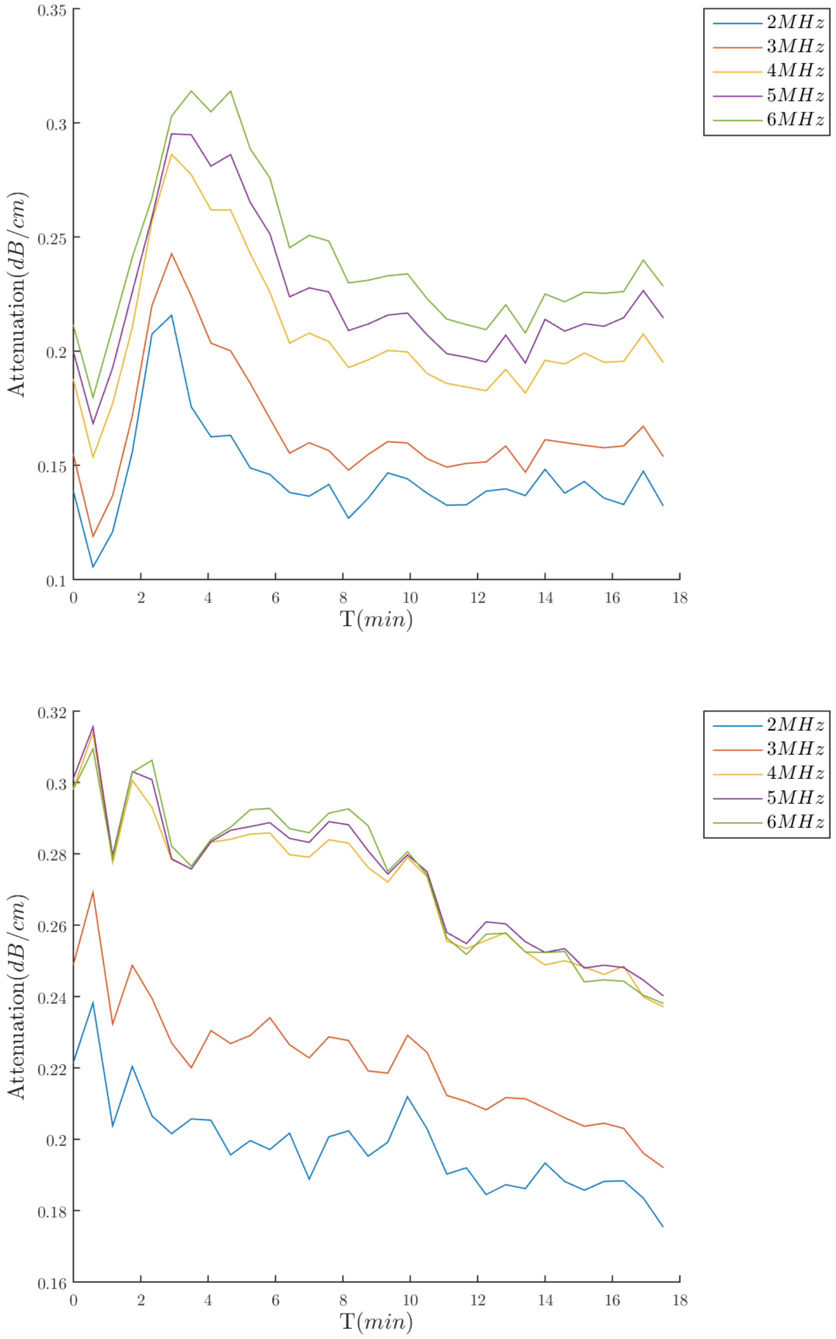

Figure 4.29: Time development of attenuation at specific frequencies for the three first measurement series of the GB 168 air batch. The number of bubbles is 10 million/50ml.

Over 140 minutes of measurements Figure 4.30 shows that there appears to be a decline early in the experiments. However, ending the series the trend is positive, making an extrapolation and prediction difficult.

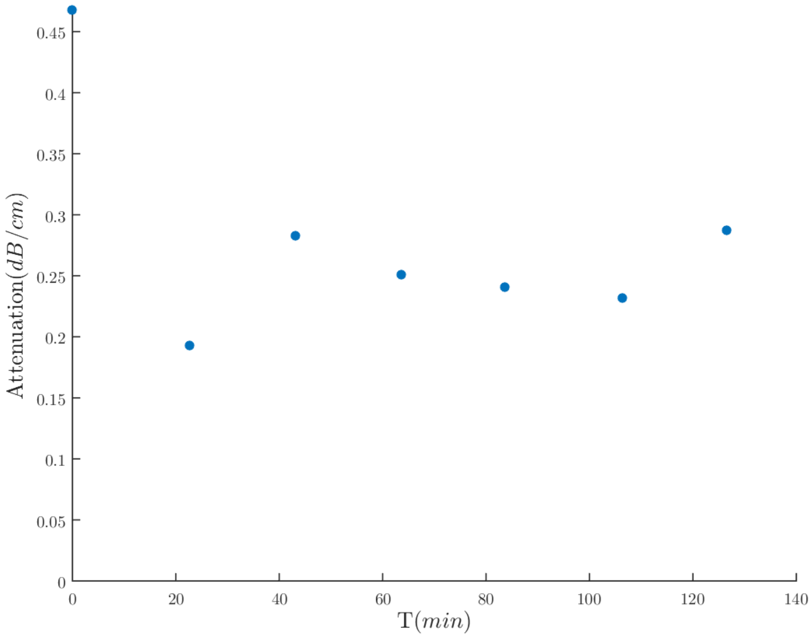

Figure 4.30: The attenuation at approximate resonance frequency, 4 MHz, at minute seven for all measurement series of the GB 168 air batch. The number of bubbles is 10 million/50 ml.

4.4.3 Microfluidic Batches

During the microfluidic production tests two different batches were produced, one with a mean diameter of 3.90 μm and the other with a mean size of 5.43 μm. For the bigger microbubbles a large part of the distribution is, however, between 6 and 7.6 μm as can be seen in Figure 4.14. The attenuation over the different frequencies as seen in Figure 4.31 depicts a broad distribution. The resonance frequency can, however, be readily obtained between 4 and 4.5 MHz.

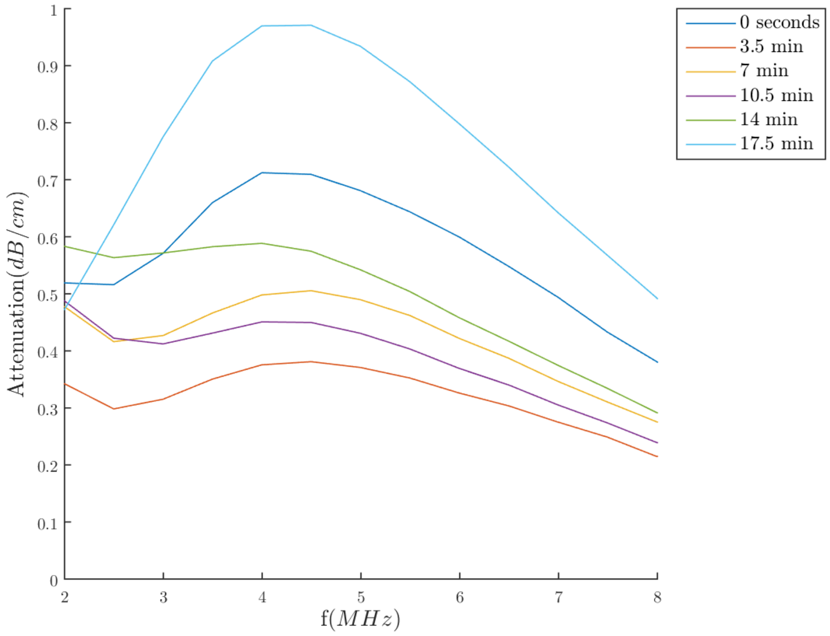

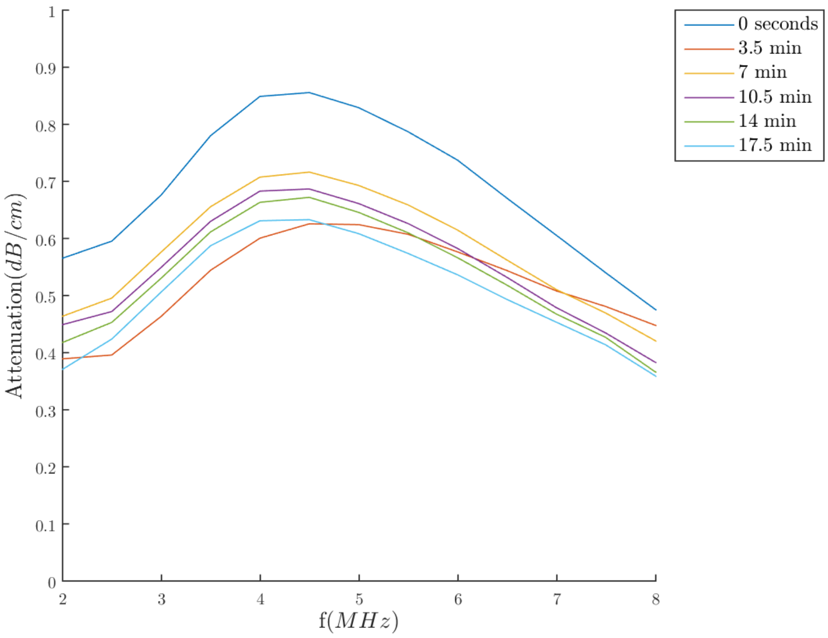

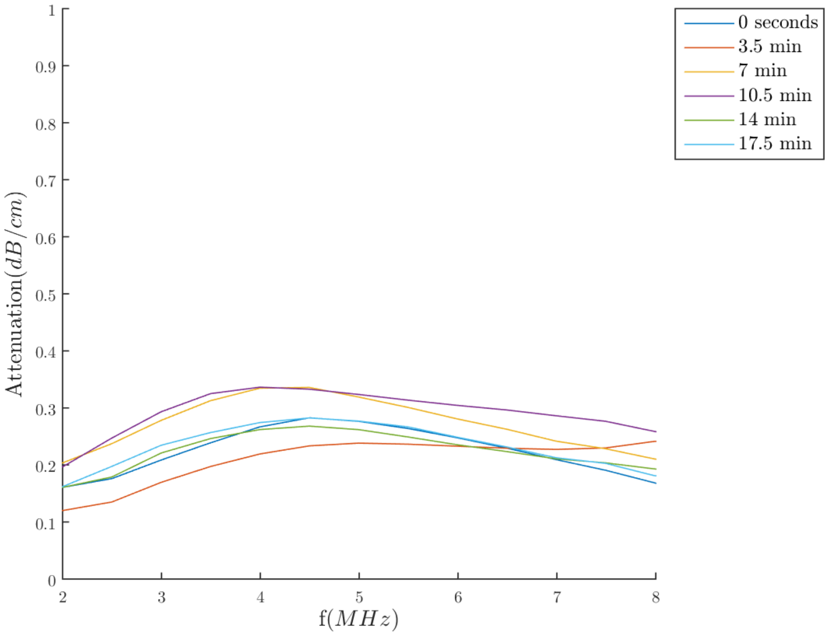

Figure 4.31: Attenuation over the full spectrum over time for measurement series one, two and four of the microfluidic standard batch. The number of bubbles is 1 million/50ml.

Looking at the time development of select frequencies in Figure 4.32 it resembles that of the air microbubbles, with large oscillations and no clear discernible trend. For the two last subfigures the lower end of the spectrum, 2 MHz, can be seen to be less attenuated over the measurements.

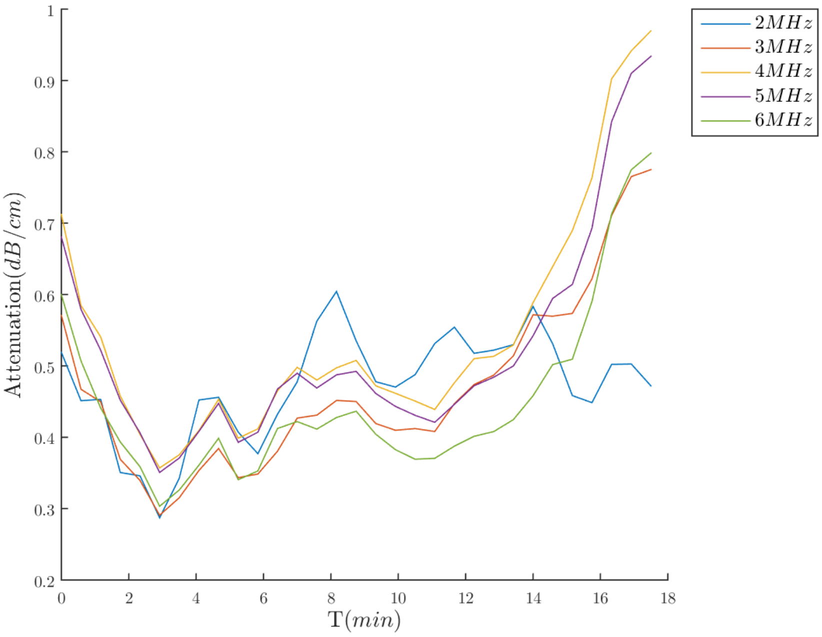

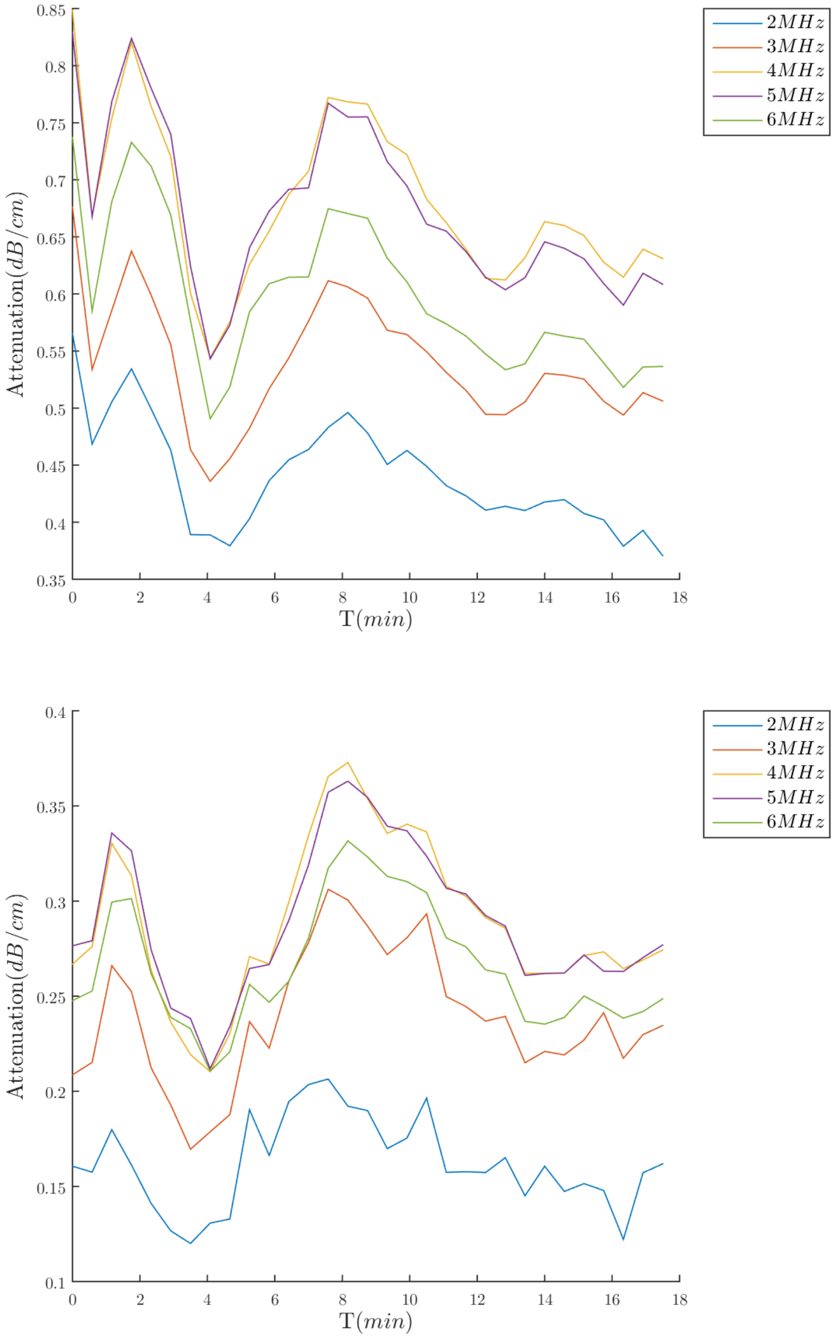

Figure 4.32: Time development of attenuation at specific frequencies for measurement one, two and four for the microfluidic standard batch. The number of bubbles is 1 million/50ml.

Across all the measurement series the batch reveals no clear trend for the time development at the approximate resonance frequency of 4 MHz, illustrated in Figure 4.33.

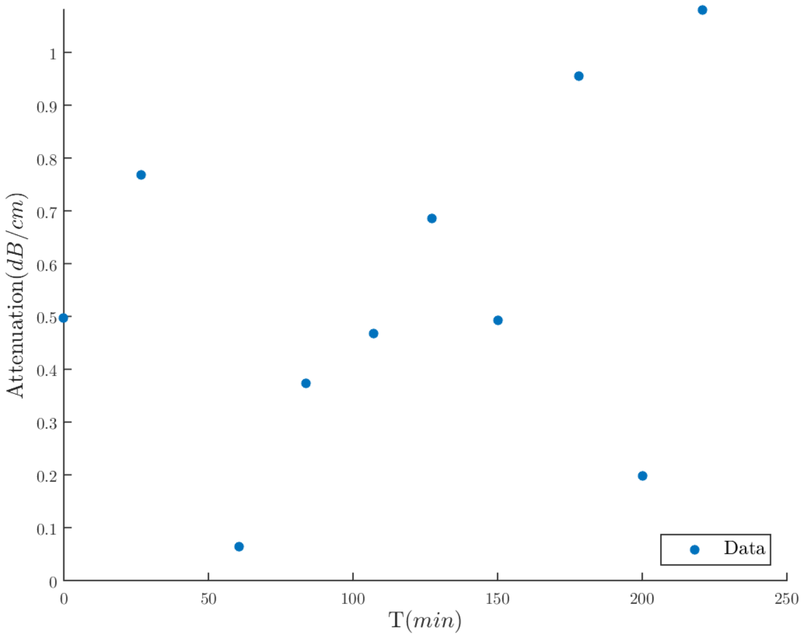

Figure 4.33: The attenuation at aproximate resonance frequency, 4 MHz, at minute seven for all measurement series of the microfluidic standard batch. The number of bubbles is 1 million/50ml.

The last batch to be analysed contained microbubbles with a larger mean diameter, this lead to the plots in Figure 4.34, where the resonance frequency is centred around the lower frequency of 2 MHz, with a sharp and slender peak.

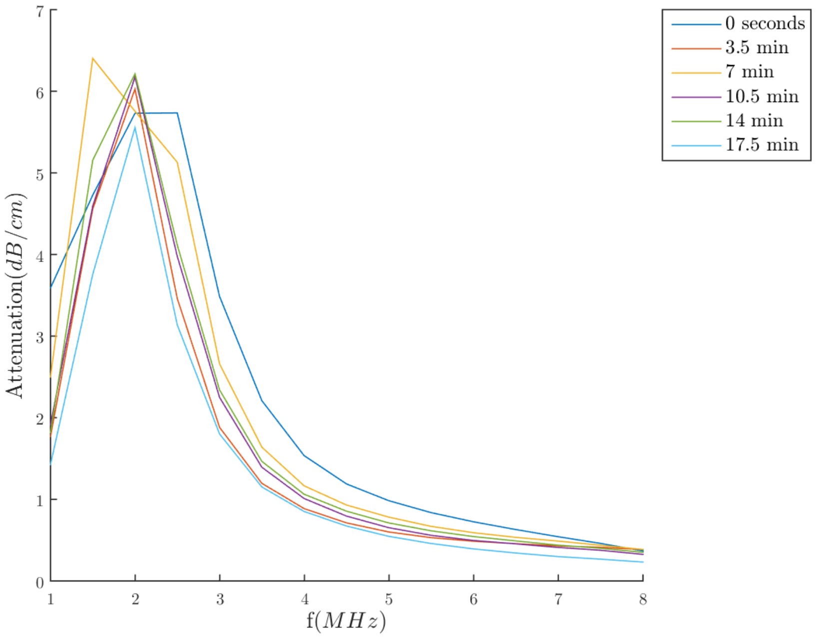

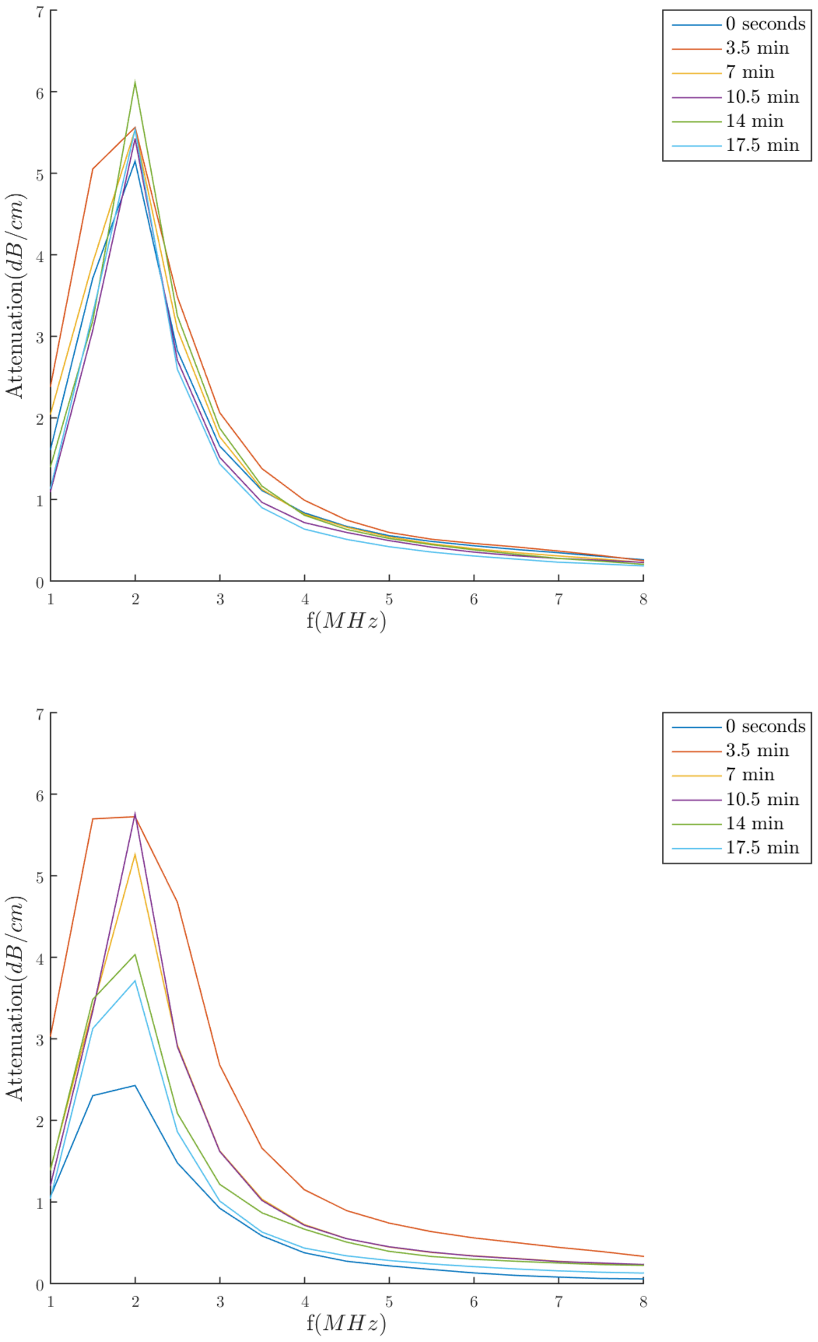

Figure 4.34: Attenuation over the full spectrum over time for the three first measurement series of the microfluidic slow batch with increased mean radius. The number of bubbles is 1 million/50ml.

The plots in Figure 4.35 further illustrates the large attenuation accounted for by the lower frequencies with 2 MHz dominating in addition to a contribution at 3 MHz. It's also interesting to note the overall large values for the attenuation, reaching values as high as 6 to 8 dB/cm.

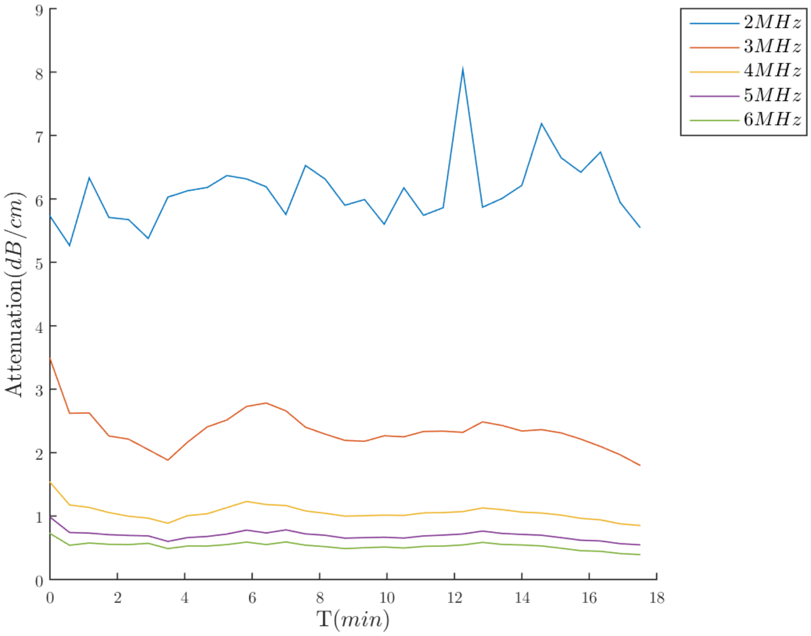

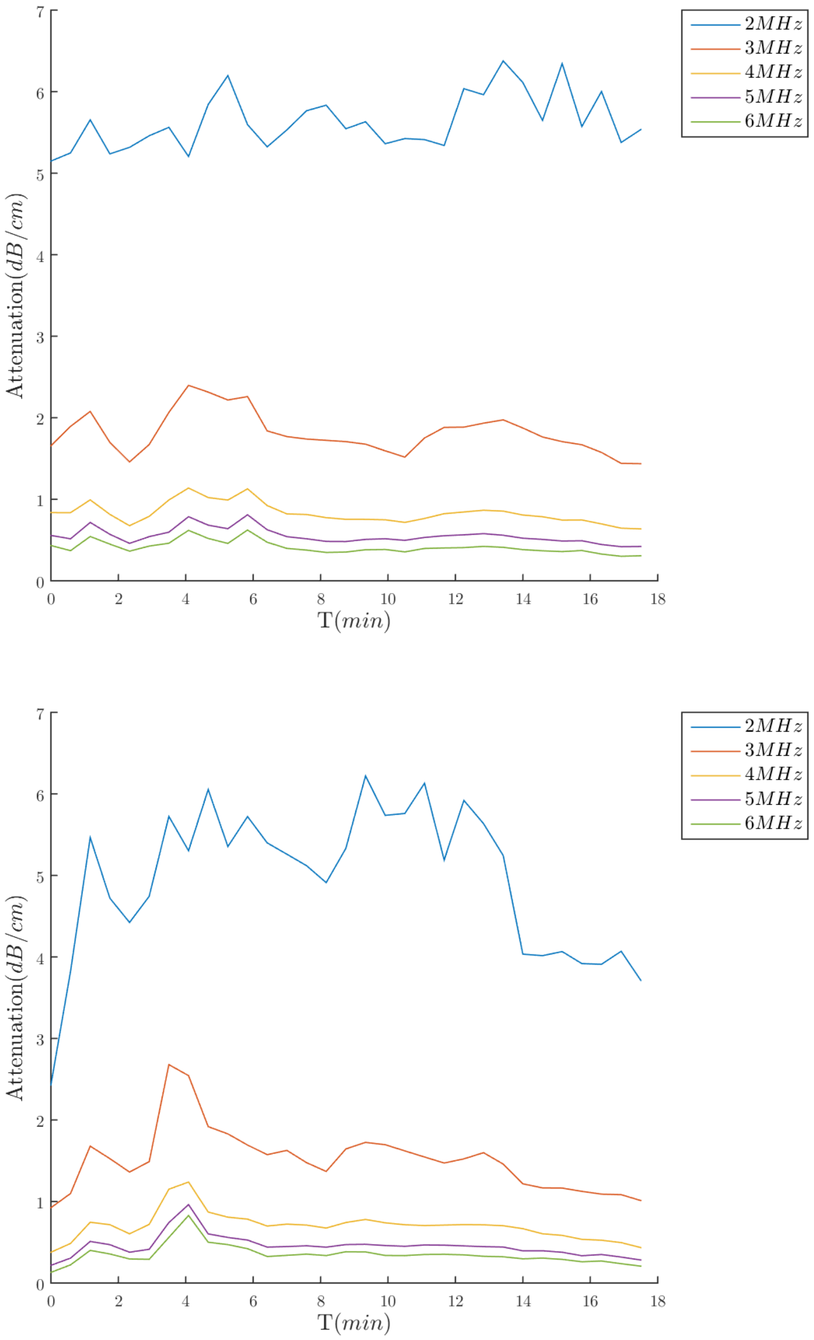

Figure 4.35: Time development of attenuation at specific frequencies for the three first measurements series of the microfluidic slow batch with increased mean radius. The number of bubbles is 1 million/50 ml.

Figure 4.36 shows that the large diameter microbubbles do not conform to the stable oscillations seen in other air microbubbles. The time development at resonance frequency is instead marked by a sharp decline after relatively short period of time. The larger average size is the only parameter separating this batch from the other air-microbubbles in principle.

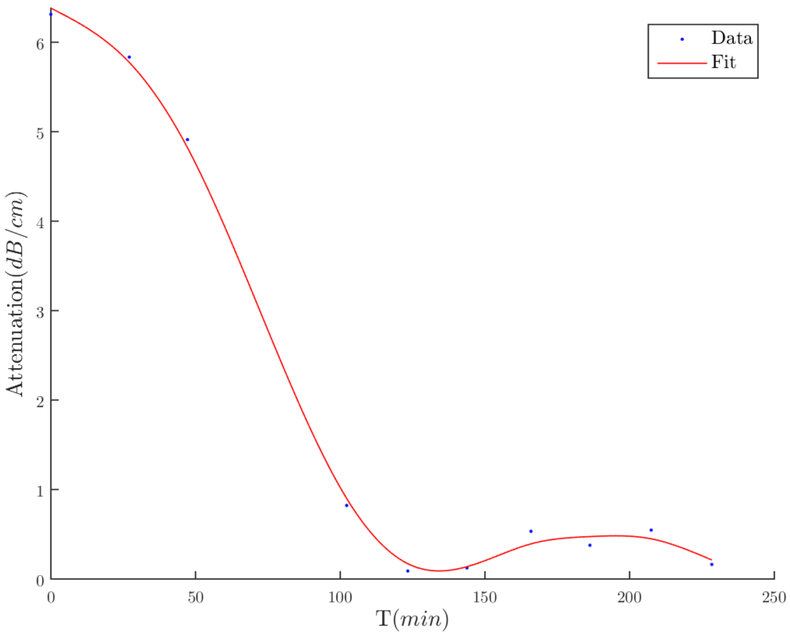

Figure 4.36: The attenuation at aproximate resonance frequency, 2 MHz, at minute seven for all measurement series of the microfluidic slow batch along with a spline fit.

Chapter 5

Discussion

5.1 Atomic Force Microscopy

5.1.1 The Setup

At the core and forming the basis for all the experimental data is the experimental setup. Observations and experiences garnered during the course of the thesis work warrants a discussion. Information gathered during the acoustic measurement may have implications for the AFM experiments and vice versa. The impression is that the technique of fastening the microbubbles with polyethylenimine inherited from Finnøy provides a reliable method and a solid platform for further analysis [36]. A significant amount of microbubbles of all the analysed batches were observed to be stationary placed against the glass surface, which is an integral prerequisite. The optical part of the AFM is, however, one important limiting factor when measuring the diameter of each microbubble. In the data the limited resolution is visible as what can be perceived as diameter ”bins”, limited regions in which the diameter value can be defined. The consequence of this binning is the less smooth transitions in the spectra as the diameter is varied and so possibly poorer fits with the theoretical models.

5.1.2 Microbubble Stability

Considering the dissolution observed during the acoustic attenuation experiments the validity of the AFM measurements have to be considered. For the PFC microbubbles the gas exchange process will begin as they are added to the water container and during the attachment procedure to the Wilco-well. The full gas exchange process has been reported to occur within seconds for SDS/SF_6, SDS being the encapsulator, microbubbles in an air saturated medium [39]. As seen in

Figure 4.23 this growth promotes dissolution and so is likely to not only affect the gas core of the microbubble, but also the shell parameters. One possible consequence is that the shrinkage following the growth period leads to the encapsulation packing more densely, making the shell increasingly rigid with decreasing diameter [39]. This would cause a potential overshoot when calculating the Young's Modulus in the theoretical models.

In this thesis only the 20th compression of each individual microbubble is used to calculate the Young's Modulus, in order to improve the reproducibility as suggested by Finnøy [36]. The image taken before and after each measurements series may not be adequate to determine permanent deformations affecting the microbubble stiffness. Comparing the 40 nN trials of GB 167 with the 400 nN measurements done on GB 162 would suggest that repeated compressions with significantly different peak loads does not seemingly have an effect.

5.1.3 Shell Thickness

The shell thickness was observed to be non-uniform in the STED images, and so this criteria is not fulfilled for the three models that analyse the shell, namely the Reissner theory, the elastic membrane model and de Jong theory. It stands to reason that these models thus carry a higher degree of uncertainty as a consequence and also that the calculated Young's Modulus can be expected to vary more as a function of diameter. This may be some of the reason why the nanoparticle-loaded microbubbles do not show a linear relationship between the stiffness and radius. Following this argument the Hertz model might provide more accurate values due to its independence of shell thickness.

5.1.4 The Reissner Theory

The Reissner theory is applied directly to the force curves obtained from the AFM. A major challenge pertaining to the GB nanoparticle microbubbles is defining a linear representative area of the force curve. In the project work this was attempted solved by a least squeares regression, however, this only found the first applicable section according to predefined criteria. In this thesis the regression was done over the points leading up to a maximal deformation of 0.1, meaning that all the points up to this limit contribute to the stiffness approximation. Comparing the project work values of 0.1 MPa to 3 MPa for the GB 160 batch shows that the regression method used in this thesis gives a wider range with 1 to 8 MPa [35]. The fit, however, gives a lower p-value, from 0.5 to 0.17 though still not significant. For microbubbles that have multiple linear regions that may be used for the Reissner theory, the simple regression up to a set deformation level, may represent a more robust evaluation method due to the removal of any heuristic criteria that may else have to be set. The criteria of the Reissner theory that the shell be significantly thinner than the radius, commonly set to 1/20, has not been met. Morris performed experiments on SonoVue® and Definity® using all the four models that are evaluated here [37]. Both represent lipid coated microbubbles, with SonoVue® having a hexafluorid core and Definity with a perfluoropropane core, as in the GB batches. The Reissner theory in this study yielded values of 302-854 MPa for Definity®. This is closer to the values found for the pure BSA microbubbles, the J6 batch, reanalysed in this work and which was found to be in the order of 10^2 higher than the GB batches. Shellwise the phospholipid monolayer of Definity® is closer to SonoVue® so the comparisons of these microbubbles to the GB batches is more valuable as an illustration of the Young's Moduli differences.

The measurements done on SonoVue® in this thesis gave values of approximately 3-7 GPa with a peak force of 40 nN and the larger range of 4 to 22 GPa for the 400 nN tests. The former value range is in close agreement with the values attained for BR14, by Morris, which was found to be 4-8 GPa. BR14 being another phospholipid system by Bracco. The Reissner theory in the same study gave values for SonoVue® in the range of 0.62 to 4.53 GPa, albeit with an assumed shell thickness of 5 nm, not 4 nm as in this study. These comparisons imply a significant overshoot for the values calculated for the SonoVue® with a peak force of 400 nN and the stiffer cantilever. This would imply a loading rate dependence for SonoVue® which is not found for the GB batches. A weak dependence has been mentioned in another study [40], the increased span is, however, in this case significant. A second study established a linearly increasing stiffness with applied force for lipid coated microbubbles, and so the result for this experiment may hold some merit [41]. With the Reissner theory these phospholipid MB's gave values of around 1 GPa. The higher values indicate that the set relative deformation region of 0.1 is not reached for the same applied force as for the cantilever with smaller spring constant, leading to an increase of points being included in the regression and finally to a steeper perceived stiffness. This may also be a consequence of cantilever contamination. Glynos et al. examined hollow thin sphered microspheres with a relevant size range of 2 to 6 μm, the shell was a double layer of polymers and albumin, encasing a core of nitrogen [27]. In this study the microspheres, which had a shell thickness that increased linearly with bubble radius, were found to have a Young's Modulus in the range of 2 to 18 GPa. The study also points to the increase in shell stiffness with decreasing shell thickness, which is also illustrated in this thesis, when comparing the thin-shelled SonoVue® with the thicker GB batches.

Picart et al. used the Reissner theory on ployelectrolyte multilayer microcapsules and this produced values of approximately 300 MPa, in the range of the pure BSA microbubbles investigated in this thesis [42]. In the master thesis of Finnøy, the precursor to this thesis, the Young's Modulus was used with nanoparticle bubbles with an air core [36]. These values were in the range of 10 to 70 MPa for three different batches, the shell thickness was, however, in these experiments set to 150 nm, representing a presumed monolayer of nanoparticles. Differences in shell thickness values accounts for the apparent increase in Young's Modulus compared to the GB batches. Three different models were also applied to lysosome encapsulated microbubbles [43]. Reissner was one of these models and gave a value of 1.3 MPa, close to the value of the GB batches.

5.1.5 The Hertz Model

The Hertz model calculates the Young's Modulus for a homogeneous sphere, rather than the contribution of the shell alone. Still, the Reissner theory and Hertz model computed strikingly similar values for the Young's Modulus for all the perfluoropropane batches containing nanoparticles, much owed to the thickness of the microbubble shell. The Hertz model does, however report higher maximum values up to 50 MPa for the GB 167 batch. This batch also shows a linear relationship between the Young's Modulus and the diameter for the model. For the J6 batch and SonoVue® the Hertz theory calculated Young's Modulus is orders of magnitude lower, compared to the nanoparticle microbubles. Turning to the phospholipid systems analysed by Morris the study found values of the Youngs Modulus in the range 0.07 to 2 MPa for all three systems [37]. This corresponds well with the findings done for the 40 nN experiments done on SonoVue®in this work, which produced values between 0.3 and 1.6 MPa. The 400 nN series again produced a wider range with higher values of 0.7 to 6 MPa. This indicates that the 40 nN measurements are the most accurate for SonoVue ®. As seen in the results for the day two SonoVue® experiments, Table 4.8, the Hertz theory yields a strong linear relationship, with a sinking Young's Modulus for increasing diameter. The Hertz model in general provides the lowest p-values for the nanoparticle microbubbles of the GB batches, indicating that while the shell Young's Modulus does not depend on the diameter, the total bubble modulus does.

The Hertz model was a second model applied by Cavalieri et al. and the Young's Modulus was found to be 0.6 MPa for lysosome microbubbles [43]. The lysosome microbubbles thus follows the trend of the total microbubble modulus to be close to the shell value. This study also used microbubbles with a thicker shell than the 1/20 limit often set for the thin-shell models, with the microbubble diameter being $2.5\,\mu\mathrm{m}$ and the thickness 150 nm.

5.1.6 Elastic Membrane Theory

The elastic membrane theory was found to produce wide ranges across all the batches. A notable exception being the 400 nN tests of a nanoparticle batch, the GB 162. As shown in Table 4.3 and 4.4 the higher maximal applied load appears to give a more precise range. Because only the stretching term of the elastic membrane theory is evaluated, the bending factor may be a larger contributor at low loading rates. All the calculations were also performed towards a relative deformation of 0.1 and this deformation may not be large enough for the stretching term to dominate. While the elastic membrane theory seems to overshoot considerably for the nanoparticle microbubbles at 40 nN peak load it produces more consistent values for the pure BSA J6 batch, where the value corresponds to the Reissner theory. The apparent loading rate dependence was not found in the different SonoVue® experiments, where the peak force was varied between 40 and 400 nN as done in the GB batches. Here the Young's modulus was consistently found to be 100 to 3000 MPa with the exception of a single data point at 8000 MPa. This shows that the stretching term may be a poor approximation for the nanoparticle microbubbles, and the force curves support this with numerous fluctuations up to the 0.1 maximal deformation. SonoVue tested in the low deformation regime, as done in this study, has given values of 0.61 to 4.7 GPa, with a similar phospholipid system giving 2 to 6 GPa [37]. These were, however, found using the bending term of the elastic membrane theory. Elastic membrane theory was also the last model to be used by Cavalieri et al. for the lysosome microbubbles and this gave 0.6 MPa. The esimated values for the GB batches suggests that the force curves have to be analysed at higher levels of deformation to avoid potential bending.

5.1.7 The de Jong model

A study done by Chen et al. used the de Jong model to estimate the Young's Modulus for perfluoropropane phospholipid microbbules [40]. The $1/8 \cdot \pi$ factor found in Morris' calculation does not appear to have been included here, however, possibly due to two different expressions being presented in the original article by de Jong. In this study the thickness was assumed to be 5 nm and this gave values of 0.2 to 2 MPa. Morris also utilized the de Jong approach for two phospholipid systems, BR14 and SonoVue, producing 0.1 to 0.8 MPa [37]. Again these values harmonize well with the 40 nN trials in this work, having given values of 0.4 to 1 MPa, the 400 nN experiment having the same lower value, but reaching 3 MPa at its highest. In general this approach returns lower estimated values for the Young's Modulus of the shell than the other models.

5.1.8 Data Analysis

The challenge of finding representative regions during the force curves persists. As argued in the Reissner section the regression up to a set deformation provides a way of including all possible linear regions into the fit. For the elastic membrane theory and Hertz theory however, this method does not provide the best fit, as is confirmed visually during analysis. When the force measurements are plotted against a power of the relative deformation, it produces a graph with a well defined non-linear section that should not be included. This region varies in length. In this thesis it was therefore opted to return to a forward wind determination method using the coefficient of determination R^2 for the Hertz and elastic membrane theories. With the fit requirement being set to a R^2<0.996 this cause some of the force curves not to be eligible. Possible solutions to this is to exclude data that are deemed not analysable or lower the threshold for the fit. Both of these options have limitations, the first may hide the true value of the Young's Modulus range and the second will include too large portions of the curve, causing an even larger spread when this was attempted with the data in this thesis. In this thesis the last 4 points were taken as representative for the slope generation with the argument that the curves show increasingly linear behavious towards the cut-off relative deformation at 0.1. Visually, this provided a good approximation found in the data obtained in this thesis. A more appropriate way of selecting these regions may be to apply a weighting scheme to the analysis to include more data points and simultaneously emphasize the later portions of the curve.

5.2 Backscatter Measurements

As seen in the backscatter results section the measured spectra are found to vary greatly across transducer pairs and mechanical index. The implementation of the Hanning-window along with the Savitzky–Golay filter produced smooth and well-defined peaks that makes comparison easier. It's important to note that the dissolution effects observed during the attenuation measurements also apply during the backscatter experiments. Parts of the perceived amplitude loss with increasing MI should therefore be expected to occur due to dissolution. The dissolution and possible fragmentation of the microbubbles may also have the effect that pure gas bubbles are present with increasing pressure and a study performed on Optison® showed that these gas microbubbles may influence the backscatter signal in the form of sharp peaks[44]. After extensive filtering these responses, that occurred in the form of sharp peaks may have been lost.

5.2.1 Higher Order Harmonics

The greatest number of partials, integer-multiples, of the fundamental frequency, as well as ultraharmonics; $3/2f_0$, $5/2f_0$ etc. is found for the 1 MHz transmitting and 5 MHz receiving transducer pair with 20 cycles. At a mechanical index of 0.26 and 0.36 this also produces a first subharmonic as seen in Figure 4.16. The first partial harmonic of double the fundamental appears to be the most persistent across the transducer pairs and also with increasing pressure. With increasing pressure, however, the second and third partial reaches the amplitude levels of the fundamental for the 1 MHz/5 MHz pair at 20 cycles and an MI of 0.45.

5.2.2 Subharmonics

The first subharmonic is present with lower mechanical indexes for the two highest transducers pairs with 3.5 MHz and 5 MHz transmitting with 5 MHz and 10 MHz receiving respectively. For the the first pair of 1 MHz transmitting and 5 MHz receving the first subharmonic is not seen before a mechanical index of 0.176. Increasing the fundamental frequency shows the subharmonic appearing for a mechanical index as low as 0.056 for the 2 cycle session with the 3.5 MHz transmitting and arguably 0.03 for the 20 cycle version. Increasing the mechanical index for this transducer pair induces the second subharmonic at MI 0.16 for the 20 cycle experiment. For the 3.5 MHz/5 MHz pair the subharmonic signal is of greater amplitude than the first ultraharmonic and indeed even the first partial when it is first generated. This is an important result, because it shows the potential of the subharmonic in imaging. The same result was obtained during backscatter measurements of Optison® with an MI of approximately 0.21 [45].
Prosperetti linked the subharmonic generation to cavitation events in the microbubble solution, stating that bubbles smaller than resonance frequency may be responsible [46]. Larger microbubbles, it is pointed out, may also have a reduced threshold for generating subharmonics.

5.2.3 Ultraharmonics

Reviewing the ultraharmonic tendencies the lowest mechanical index to induce this effect is found at an MI of 0.056 with the transmitting transducer of 3.5 MHz and 5 MHz receiving with 20 cycles. This ultraharmonic corresponds to the first at $3/2f_0$. Increasing the mechanical index to 0.0805 sees this ultraharmonic grow to a level close to the first partial. The greatest number of different ultraharmonics is found in data produced by the 1 MHz/5MHz pair, which reveals as much as 10 different ultraharmonic peaks with a MI of 0.26 to 0.36. A study done on SonoVue® found the first ultraharmonics to be generated at a mechanical index of 0.04 with a transmitting transducer of 3.5 MHz [47]. This is around half the value of that found for the nanoparticle loaded microbubbles in this study.

5.3 Attenuation Measurements

5.3.1 Microbubble Coalescence

One effect that would possibly impact that results from the attenuation measurements is that of bubble coalescence and the potential for ultrasound to drive this process [18]. As the microbubbles merge to form the more voluminous products one might expect the attenuation spectrum to shift providing amplification in the lower parts of the spectrum during the measurements. This general shift over the 18 minutes of each series was not observed, rather the lower frequencies attenuation seemed to have a tendency to fall off more steeply than the higher ones as observed for the PFC microbubbles in Figure 4.22. This indicates that effects such as buoyancy may have a greater impact on the development of the attenuation than coalescence. Both the air and PFC microbubbles, have spectra that show an unstable period in the first minutes after being added to the chamber with growth. During this period the microbubbles are not stationary and still affected by the stirring ,used to achieve uniform distribution. In this period coalescence can not be neglected as the turbulent movement is likely to increase bubble to bubble reactions, such as coalescence.

5.3.2 Dissolution and Buoyancy

Using the acquired data from the attenuation experiments it is possible to analyse the attenuation loss over time to investigate the processes involved in gain or loss in the attenuation. By modifying the Epstein-Plesset equation, models describing the predicted dissolution of shelled microbubbles have been produced [9]. Solving the Epstein-Plesset for a free air bubble predicts a dissolution time of one second in satured water [48]. Comparing this to the attenuation loss found in air and PFC microbubbles in this study the impression is that the encapsulating shell has a significantly stabilizing effect.

The microbubbles containing air and perfluoropropane were found to behave very differently when added to the PBS chamber where the size distribution was also found to have an impact on the rate of attenuation loss. Both versions of the microbubbles have unstable regions when looking at the time development at different frequencies for the first minutes at individual measurement series. Looking at the development at approximate resonance frequency at the same time over all series, however, reveal drastic differences. The growth seen in Figure 4.23 is associated with the gas exchange, where the perfluoropropane is diffusing out through the shell, while the gases in the PBS are diffusing inwards. Version have been made of the Epstein-Plesset to account for these dynamics, but the implementation was not in the scope of this thesis [49]. Efforts have also been made to incorporate nanoparticles into the equation [50]. This gaseous growth is followed by a sharp decline, indicating that the growth is detrimental to the stability of the bubble and facilitates disintegration.

The air microbubbles with a similar size distribution do not exhibit this behaviour, seen in Figure 4.30 and 4.30, which, considering that the microbubbles have the same shell features, points to the gaseous core as being the reason for the different developments. The stable gas exchange and external/internal pressures for the air microbubbles, making them have a stable radius and thus avoid the following sharp dissolution is likely responsible.

Comparing the two different microfluidic batches highlights the impact of size distribution on the attenuation development. While both batches show no clear trends over each 18 minute measurement, the development across all the series is more profound. While the smaller microbubble batch has an erratic distribution of values, the larger microbubbles show a marked decline at the resonance frequency. The lack of the same decline in the individual measurement series points to buoyancy as the driving factor, affecting the larger bubbles while placed in the container before being extracted for the individual series. While in the chamber, the assumption is that the microbubbles are uniformly distributed and so the number of microbubbles in the transducer field stays somewhat constant. This would imply that there is a cut of size where the microbubble diameter creates buoyancy to outweigh the density of the shell, preserving the smaller radius microbubbles.

5.3.3 Experimental Procedure

When the attenuation measurements were first initiated the microbubbles were extracted by the use of a syringe and transferred to an intermediate container before pipetting. This procedure produced very low attenuation and it was speculated that the multiple steps and the syringe were causing major bubble destruction. The following experiments were therefore conducted with open containers, allowing for direct pipetting in order to minimize microbubble damage. The influx of air during the opening of the canister, however, fundamentally changes the gas interior of the microbubble as was shown in Figure 4.23. Therefore only the first measurement series can be assumed to contain the original gas contents. The optimal solution may therefore be to use a larger needle size and transfer the microbubbles directly from the syringe to the PBS-chamber. Due to this realization the Epstein-Plesset model was only fitted for the first measurement series, were the gas contents were assumed to be known.

5.3.4 Attenuation Spectra

A study done on the Optison® microbubbles, which features the same perfluoropropane core as the GB batches analysed in this thesis show attenuation spectra that share several characteristics with the latter [45]. The surfactant is not the same however, as Optison® utilizes human serum albumin instead of casein, and does not contain nanoparticles. According to the findings made in the study the Optison®microbubbles also undergo a growth period for the first 5-7 minutes, typical of gas exchange were the attenuation increases. The attenuation values for Optison®were found to be in the range of 2-3 dB/cm before the growth and following decline, with a concentration of 55000 bubbles/ml. Taking the concentration into account this attenuation is substantially higher than the 0.5 to 1.2 dB/cm found for the bubbles in this study, which were computed from a concentration of 200 000 bubbles/ml. The size distribution of Optison is, however, larger, featuring a maximal microbubble size of $32\,\mu\mathrm{m}$, while the GB batches do not appear to feature microbubbles over $20\,\mu\mathrm{m}$. The contribution of the larger bubbles is supported by the attenuation peak in the Optison® study which is situated between 1-2 MHz.

Comparing the PFC microbubbles with 10 million bubbles/50 ml with the same concentration of air microbubbles show that the PFC microbubbles provide a higher dampening with the maximum values of 0.6 to 1.2 for the three first measurements of PFC and 0.3 to 0.6 dB/cm for air. With the gas exchange process starting instantly as the PFC microbubbles reach the undersaturated PBS the higher values may be partially due to bubble growth before the measurement starts. The non-linear increase between experiments with ten and ten million microbubbles is the sample chamber is of some concern and may be related to either measurement uncertainties or extensive microbubble destruction as they are introduced into the chamber. As the microbubbles are pipetted from the container they are in contact with an environment that is more undersatured in perfluorpropane than the container and this may cause bubble collapse. The same may be the case after the introduction to the chamber. It may be possible to investigate this further by running an experiment where the measurements are rapidly recorded and initiated before microbubble addition to the chamber. The higher temporal resolution may provide insight into whether there is a marked growth phase followed by loss in the attenuation, seeing as the measurements done in this thesis have a start point that is seconds after bubble addition.

5.3.5 Shell Resistance

Solving the Epstein-Plesset equation with an incorporated shell showed that the shell provides a considerable resistance to gas diffusion. The values plugged in for surface tension and saturation are not measured values and were taken from a study done onthe dissipation of Definity® and a lipid-shell perfluoropropane system [38]. The shell resistance calculated here of 10^5 s/m only gives an impression of the resistance for a uniformly sized microbubble batch and is a minimum value as considerable attenuation persists after the end of the measurement series. By doing a single long measurement series of around one hour with a fresh batch where the gas contents are knows this charachteristic can be determined with a higher precision. Nevertheless, free microbubbles without a shell resistance gives dissolution values in the order of seconds [51].

5.4 Implications

The results from the AFM measurements would indicate that the addition of nanoparticles to the shell lowers the stiffness of the microbubble, possibly due to less dense packing. This in turn would entail that the pressure required to rupture the microbubble with ultrasound would be diminished and also affect the resonance frequency, a non-uniform shell has also been found to lessen the critical pressure[52]. As the microbubbles are sought to be used as drug delivery vehicles, this is an important consideration. The addition of nanoparticles has also been found to decrease the stiffness in microbubbles, where magnetic nanoparticles were attached to the bubble surface [53].

The gas diffusion process tracked in the attenuation measurements may lead to increased buckling of the shell as the gas leaks out of the microbubble and increase non-linear behaviour in the backscatter measurements [54]. This could potentially lead to an increase in contrast by increasing “compression-only” behaviour, meaning that the microbubble does not expand to a large degree, but rather contracts.

Higher integer-multiples of the fundamental has been shown to provide an increasing contrast ratio with frequency [55]. As seen in the 1 MHz/5 MHz pair the number of higher harmonics is significant and the amplitudes are also high compared to the fundamental and first harmonic, which is currently used a extensively in imaging. The exceedingly non-linear behaviour of the nanoparticle microbubbles may therefore provide an improved contrast ratio due to this feature.

5.5 Future Work

In order to improve upon the predicted values found by the different models in the AFM experiments the shell thickness needs to be accurately determined. Even if an average value has to be established due to the tendency of the nanoparticles to be layered, an important aspect is whether the thickness of the shell is dependant of the microbubble diameter. If this is found to be the case then this could be included in the models determining the Young's Modulus of the shell. Another unanswered question is that of the gas exchange effect on the shell integrity and stiffness. As the sample preparation process for the AFM is tedious, largely due to the process of attaching the microbubbles to the Wilco-Well®, the acoustic setup might offer a better route to investigate these dynamics. In this setup the measurements can be started within seconds after adding the microbubbles to a PBS solution and so it might be possible to see if the acoustic pressure threshold causing significant bubble destruction is lowered with time spent in the PBS-chamber.

Chapter 6

Conclusion

By analysing perfluoropropane microbubbles through atomic force microscopy the results from this study indicate that adding nanoparticles to the shell lowers the Young's Modulus of the shell. No significant relationship was found between the diameter of the microbubble and the Young's Modulus and the impression is that this is due to the inconsistent shell thickness. This is indicated by the high-resolution images of the shell as well as the buckled appearance of the microbubbles when viewed under brightfield and fluorescence microscopy. While the Reissner theory, Hertz theory and De Jong model all show consistent values, the poor fit of the elastic membrane models may indicate that there is a substantial bending of the shell in the lower deformation region. The microbubbles, however, seem highly resistant to high peak loads up to 400 nN. Through attenuation measurements it was shown that the perfluoropropane microbubbles behave very differently than air microbubbles otherwise produced with the same specifics. The gas exchange process occuring when the microbubbles are added to the sample chamber was found to promote bubble dissolution, with this process being determined as the lead cause of attenuation loss. By solving the Epstein-Plesset equation for a perfluropropane microbubble it was shown that the microbubble shell provides a resistance to gas exchange, an important in vivo characteristic. Backscatter experiments revealed that the nanoparticle coated microbubbles produce sub-harmonics , harmonics and ultraharmonics at low pressure levels for given frequencies. These are important features that may be exploited to produce higher contrast during imaging.

Bibliography

[1] F. Calliada, R. Campani, O. Bottinelli, A. Bozzini, and M. G. Sommaruga. Ultrasound contrast agents; basic principles. *European Journal of Radiology*, 27:157–160, 1998.

[2] S. Mayer and P. A. Grayburn. Myocardial contrast agents: Recent advances and future directions. *Progress in Cardiovascular Diseases*, 44:33–44, 2001.

[3] D. Cosgrove. Ultrasound contrast agents: An overview. *European Journal of Radiology*, 60(3):324–330, 2006.

[4] S. R. Grobmyer, N. Iwakuma, P. Sharma, and B. M. Moudgil. *Cancer Nanotechnology: Methods and Protocols*, chapter 1, pages 1–11. Humana Press, Springer, 2010.

[5] W. M. Pardridge. Drug transport across the blood–brain barrier. *Journal of Cerebral Blood Flow and Metabolism*, 32:1959–1972, 2012.

[6] J. I. Park, D. Jagadeesan, R. Williams, W. Oakden, S. Chung, G. J. Stanisz, and E. Kumacheva. Microbubbles loaded with nanoparticles: A route to multiple imaging modalities. *ACS Nano*, 4(11):6579–6586, 2010.

[7] S. I. Fox. *Human Physiology*. McGraw-Hill, New York, 2013.

[8] A. Klibanov. Ligand-carrying gas-filled microbubbles: Ultrasound contrast agents for targeted molecular imaging. *Bioconjugate Chem.*, 16:9–17, 2005.

[9] Borden M. A and M. L. Longo. Dissolution behaviour of lipid monolayer-coated, air-filled microbubbles: Effect of lipid hydrophobic chain length. *Langmuir*, 18:9225–9233, 2002.

[10] L. Zhang, F. X. Gu, J. M. Chan, A. Z. Wang, R. S. Langer, and O. C. Farokhzad. Nanoparticles in medicine: Therapeutic applications and developments. *Clinical Pharmacology and Therapeutics*, 83(5), 2008.

[11] D. Sutton, N. Nasongkla, E. Blanco, and J. Gao. Functionalized micellar systems for cancer targeted drug delivery. *Pharmaceutical Research*, 24(6), 2007.

[12] E. Stride, K. Pancholi, M. J. Edirisinghe, and S. Samarasinghe. Increasing the nonlinear character of microbubble oscillations at low acoustic pressures. *J. R. Soc. Interface*, 5:807–811, 2008.

[13] K. Greish. *Cancer Nanotechnology: Methods and Protocols*, chapter 3, pages 25–39. Humana Press, Springer, 2010.

[14] K. Greish, T. Sawa, J. Fang, T. Akaike, and H. Maeda. Sma-doxorubicin, a new polymeric micellar drug for effective targeting to solid tumours. *Journal of Controlled Release*, 97:219–230, 2004.

[15] J. R. Lindner, J. Song, J Christiansen, A. Klibanov, F. Xu, and K. Ley. Ultrasound assessment of inflammation and renal tissue injury with microbubbles targeted to p-selectin. *Circulation*, 2001.

[16] M. Overvelde, H. J. Vos, N. de Jong, and M. Versluis. *Ultrasound contrast agents*, chapter 7, pages 79–97. Springer, 2010.

[17] L. Hoff. *Acoustic Characterization of Contrast Agents for Medical Ultrasound Imaging*. Springer, 2001.

[18] M. Postema, P. Marmottant, C. T. Lancée, S. Hilgenfeldt, and N. de Jong. Ultrasound-induced microbubble coalescence. *Ultrasound in Med. & Biol.*, 30(10):1337–1344, 2004.

[19] J. Wu and W. L. Nyborg. Ultrasound, cavitation bubbles and their interaction with cells. *Advanced Drug Delivery Reviews*, 60:1103–1116, 2008.

[20] J. Collis, R. Manasseh, P. Liovic, P. Tho, A. Ooi, K. P. Duran, and Y. Zhu. Cavitation microstreaming and stress field created by microbubbles. *Ultrasonics*, 50:1103–1116, 2010.

[21] R. V. Shohet, S. Chen, Y. Zhou, Z. Wang, R. S. Meidell, R. H. Unger, and P. A. Grayburn. Cardiographic destruction of albumin microbubbles directs gene delivery to the myocardium. *Circulation*, 101:2554–2556, 2000.

[22] J. P. Dear, J. E. Field, and A. J. Walton. Gas compression and jet formation in cavities collapsed by a shock wave. *Nature*, 332:2554–2556, 1988.

[23] C. E. Brennen. *Cavitation and Bubble Dynamics*. Oxford University Press, Oxford, 1995.

[24] W. Chen, T. J. Matula, and L. A. Crum. The dissapearance of ultrasound contrast bubbles: Observations of bubble dissolution and cavitation nucleation. *Ultrasound in Med. and Biol.*, 28(6):793–803, 2002.

[25] P. S. Epstein and M. S. Plesset. On the stability of gas bubbles in liquid-gas solutions. *The Journal of Chemical Physics*, 18(11):1505–1509, 1950.

[26] N. de Jong, F. J . Cate, C. T. Lancée, J. R. T. C. Roelandt, and N. Bom. Principles and recent developments in ultrasound contrast agents. *Ultrasonics*, 29:324–330, 1991.

[27] E. Glynos, V. Koutsos, W. McDicken, C. Moran, S. Pye, J. Ross, and V. Sboros. Nanomechanics of biocompatible hollow thin-shell polymer microspheres. *Langmuir*, 25:7514–7522, 2009.

[28] N. Elsner, F. Dubreuil, R. Weinkamer, M. Wasicek, F. D. Fischer, and A. Fery. Mechanical properties of freestanding polyelectrolyte capsules: a quantitative approach based on shell theory. *Progr Colloid Polym Sci*, 132:117–123, 2006.

[29] E.B. Santos, J.K. Morris, E. Glynos, V. Sboros, and V. Koutsos. Nanomechanical properties of phospholipid microbubbles. *Langmuir*, 28:5753–5760, 2012.

[30] R. W. Carpick, N. Agrait, D. F. Ogletree, and M. Salmeron. Measurment of interfacial shear(friction) with an ultrahigh vacuum atomic force microscope. *Departemental Papers (MEAM)*, 97, 1996.

[31] V. Lulevich, T. Zink, H. Chen, F. Liu, and G. Liu. Cell mechanics using atomic force microscopy-based single-cell compression. *Langmuir*, 22:8151–8155, 2006.

[32] V. Lulevich, D. Andrienko, and O. I. Vinogradova. Elasticity of polyelectrolyte multilayer microcapsules. *Journal of Chemical Physics*, 120(8):3822–3826, 2004.

[33] J. Tu, J. Guan, Y. Qiu, and T. J. Matula. Estimating the shell parameters of sonovue® microbubbles using light scattering. *J. Acoust. Soc. Am.*, 126(6), 2009.

[34] N. Sponheim, L. Hoff, A. Waaler, B. Muan, H. Moms, S. Holm, M. My, N. de Jong, and T. Skotland. Albunex - a new ultrasound contrast agent. pages 103–108, 1993.

[35] G. F. Moe. Mechanical charcaterization of perfluorocarbon microbubbles containing nanoparticles. Project thesis, 2014.

[36] Andreas Finnøy. Acoustic and mechanical properties of microbubbles stabilized by polymeric nanoparticles. Master's thesis, NTNU - Norwegian University of Science and Technology, 2013.

[37] J. K. Morris. *The Mechanical Properties of Phospholipid Coated Microbubbles*. PhD thesis, The University of Edinburgh, 2014.

[38] K. Sarkar, A. Katiyar, and P. Jain. Growth and dissolution of an encapsulated contrast microbubble: effects of encapsulation permeability. *Ultrasound Med Biol.*, 35(8):1385–1396, 2009.

[39] J. J. Kwan and M. A. Borden. Microbubble dissolution in a multigas environment. *Langmuir*, 26(9):6542–6548, 2010.

[40] C. C. Chen, S. Wu, J. D. Finan, B. Morrison III, and E. E. Konofagou. An experimental study on the stiffness off size-isolated microbubbles using atomic force microscopy. *Trans Ulttrason Ferroelectr Freq Control*, 60(3):524–534, 2013.

[41] R. H. Abou-Saleh, S. A. Peyman, K. Critchley, S. D. Evans, and N. H. Thomson. Nanomechanics of lipid encapsulated microbubbles with functional coatings. *Langmuir*, 29:4096–4103, 2013.

[42] C. Picart, B. Senger, K. Sengupta, F. Dubreuil, and A. Fery. Measuring mechanical properties of polyelectrolyte multilayer thin films: Novel methods based on afm and optical techniques. *Colloids and Surfaces A: Physicochem. Eng. Aspects*, 303:30–36, 2007.

[43] F. Cavalieri, J. P. Best, C. Perez, J. Tu, F. Caruso, T. J. Matula, and M. Ashokkumar. Mechanical characterization of ultrasonically synthesized microbubble shells by flow cytometry and afm. *Appl. Mater. Interfaces*, 5:10920–10925, 2013.

[44] A. Y. Ammi, R. O. Cleveland, J. Mamou, G. I. Wang, S. L. Bridal, and Jr. W. D. O'Brien. Ultrasonic contrast agent shell rupture detected by inertial cavitation and rebound signals. *IEEE Transactions on Ultrasonics, Ferroelectrics, and Frequency Control*, 53(1), 2006.

[45] W. T. Shi and F. Forsberg. Ultrasonic characterization of the nonlinear properties of contrast microbubbles. *Ultrasound in Medicine & Biology*, 26(1):93–104, 2000.

[46] A. Prosperetti. Nonlinear oscillations of gas bubbles in liquids: transient solutions and the connection between subharmonic signal and cavitation. *J. Acoust. Soc. Am.*, 57(4), 1975.

[47] N. de Jong, M. Emmer, A. van Wamel, and M. Versluis. Ultrasonic characterization of ultrasound contrast agents. *Med Biol Eng Comput*, 47:861–873, 2009.

[48] M. A. Borden, S. Qin, and K. W. Ferrara. *Molecular Imaging: Principles and Practice: Ultrasound Contrast Agents*, chapter 28, pages 425–444. People's Medical Publishing House - USA, 2010.

[49] A. Kabalnov, D. Klein, T. Pelura, E. Schutt, and J. Weers. Dissolution of multicomponent microbubbles in the bloodstream: 1. theory. *Ultrasound in Medicine & Biology*, 24(5):739–749, 1998.

[50] M. Azmin, G. Mohamedi, M. Edirisinghe, and E. P. Stride. Dissolution of coated microbubbles: The effect of nanoparticles and surfactant concentration. *Materials Science and Engineering C*, 32:2654–2658, 2012.

[51] S. V. Dalvi and J. R. Joshi. Modelling of microbubble dissolution in aqueous medium. *Journal of Colloid and Interface Science*, 437, 2014.

[52] P. V. Chitnis, S. Koppolu, J. Mamou, C. Chlon, and J. A. Ketterling. Influence of shell properties on high-frequency ultrasound imaging and drug delivery using polymer-shelled microbubbles. *IEEE Transactions on Ultrasonic, Ferroelectrics, and Frequency Control*, 60(1), 2013.

[53] G. Guo, L. Lu, L. Yin, J. Tu, X. Guo, J. Wu, D. Xu, and D. Zhang. Mechanical and dynamic chatacteristics of encapsulated microbubbles coupled bu magnetic nanoparticles as multifunctional imaging and drug delivery agents. *Phys. Med. Biol.*, 59:6729–6747, 2014.

[54] N. de Jong, M. Emmer, C. T. Chin, A. Bouakaz, F. Mastik, D. Lohse, and M. Versluis. "compression-only" behaviour of phospholipid-coated contrast bubbles. *Ultrasound in Medicine & Biology*, 33(4):653–656, 2007.

[55] A. Bouakaz, S. Frigstad, F. J. T. Cate, and N. de Jong. Super harmonic imaging: A new imaging technique for improved contrast detection. *Ultrasound in Medicine & Biology*, 28(1):59–68, 2002.